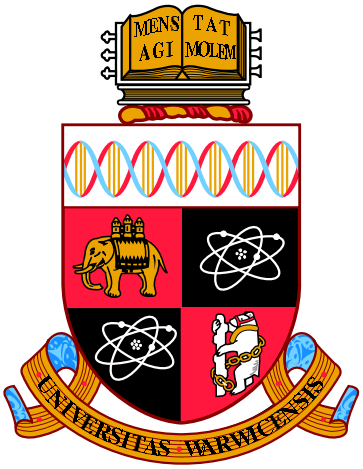

Overhauser Dynamic Nuclear Polarisation Studies in Solution-State at 3.4T

by

Thomas Kai Yip Tam

Thesis

Submitted to the University of Warwick

for the degree of

Doctor of Philosophy

Department of Physics

March 2013

THE UNIVERSITY OF WARWICK

Contents

List of Tables **iv**

List of Figures **v**

Acknowledgments **xi**

Declarations **xii**

Abstract **xiii**

Abbreviations **xiv**

Chapter 1 Introduction **1**

1.1 Development of microwave-driven DNP 2

1.1.1 Early experiments 2

1.1.2 Modern revival 2

1.2 Thesis overview and motivation 3

Chapter 2 Theoretical background **5**

2.1 Nuclear magnetic resonance 5

2.1.1 Spin angular momentum and nuclear magnetism 5

2.1.2 Zeeman splitting 6

2.1.3 Longitudinal magnetisation 7

2.1.4 Transverse magnetisation 8

2.1.5 Spin relaxation 8

2.1.6 Internal spin interactions 12

2.1.7 Detection and Fourier transformation 14

2.2 Electron paramagnetic resonance 15

2.2.1 Electron spin and the Zeeman effect 15

2.2.2 The g-factor 15

2.2.3 Hyperfine interaction 16
2.2.4 Electron-spin exchange 18
2.2.5 Detection 18
2.3 Dynamic nuclear polarisation 18
2.3.1 Electron-nuclear spin system 19
2.3.2 The Overhauser effect 20

Chapter 3 Review of dynamic nuclear polarisation experiments 28
3.1 Discovery and early investigations of the Overhauser effect 28
3.2 Solid-state mechanisms and DNP at high magnetic field strengths . . 31
3.3 Feasibility of high-field liquid DNP 31
3.3.1 Direct polarisation in-situ 31
3.3.2 Sample transfer 34
3.4 Polarising agents 35
3.5 Overhauser equation parameters 37
3.5.1 Coupling factors at high frequency 38
3.5.2 Saturation factor 40

Chapter 4 Experimental details 44
4.1 A 94 GHz spectrometer for in-situ DNP-NMR at 3.4 T 44
4.1.1 Microwave source 45
4.1.2 Modified ENDOR probe and cavity 48
4.1.3 NMR spectrometer 49
4.2 Sample preparation and positioning 50
4.3 One-pulse NMR experiment 52
4.4 Nuclear T_1 measurements — inversion-recovery and saturation-recovery experiments 52
4.5 Acquisition of CW-EPR spectra 54
4.6 Overhauser DNP experiments 54
4.7 Simultaneous use of two independent microwave sources 56

Chapter 5 DNP enhancement of water protons with TEMPOL radical 61
5.1 Introduction 61
5.1.1 Polarisation of water protons 62
5.1.2 Factors reducing maximum enhancement 62
5.2 Experimental details 63
5.2.1 Sample preparation 63

5.2.2 Experiment 63
5.3 Results and discussion 64
5.3.1 Temperature dependence of enhancement, nuclear relaxation and EPR spectrum 64
5.3.2 Modelling of data with time-step calculations using instantaneous I_{enh} and T_{1I} values 70
5.4 Conclusions 78

Chapter 6 Overhauser DNP of small organic compounds in aqueous solutions 80
6.1 Glycine 81
6.1.1 Experimental details 82
6.1.2 Results and discussion 83
6.2 L-proline 92
6.2.1 Experimental details 93
6.2.2 Results and discussion 93
6.3 Acrylic acid 98
6.3.1 Experimental details 99
6.3.2 Results and discussion 99
6.4 Conclusions 109

Chapter 7 Investigation of saturation by simultaneous irradiation of two EPR lines 113
7.1 Introduction 113
7.2 Experimental details 115
7.2.1 Samples 115
7.2.2 Dual irradiation experiments 116
7.3 4-oxo-TEMPO-d_{16}-^{15}N — two hyperfine lines 116
7.4 TEMPOL — three hyperfine lines 119
7.5 Discussion 123
7.6 Conclusions 127

Chapter 8 Summary and conclusions 129

List of Tables

5.1 Summary of DNP enhancements and coupling factor data for several studies conducted at 3.4 T 76

6.1 Summary of relaxation time and enhancement measurements used to estimate leakage factors and coupling factors in three different samples of organic compounds in aqueous solutions. 110

7.1 Summary of dual irradiation DNP experiment results for 5 mM 4-oxo-TEMPO-d_{16}-^{15}N in toluene, showing the effect of increasing saturation of second EPR transition on ε. Experiments where all microwave power is applied on-resonance have been emphasised in the table with bold font and double arrows; 'L' and 'S' indicate 'large' and 'small' changes in enhancement, respectively (arbitrarily defined as >15% and <15%). 120

7.2 Summary of dual irradiation DNP experiment results for 2.5 mM TEMPOL in toluene, showing the effect of increasing saturation of a second EPR transition on ε. Experiments with Source B and A irradiating allowed EPR transitions are highlighted with enhancements in bold and enhancement change represented by double arrows; 'L' and 'S' indicate 'large' and 'small' changes in enhancement, respectively (arbitrarily defined as >15% and <15%). 124

List of Figures

2.1 Lorentzian spectral density functions showing molecular motion in the slow, intermediate and fast regimes. 10

2.2 Plot illustrating the variation of the spin-lattice ($1/T_1 \propto \tau_c/(1 + (\omega_0\tau_c)^2)$) and spin-spin ($1/T_2 \propto 3J(0)+5J(\omega_0)+2J(2\omega_0)$) relaxation time constants with the correlation time of molecular motion [16]. Regions for slow, intermediate and fast motion are indicated, as well as the effect of increasing molecule size, liquid viscosity and temperature on relaxation. 10

2.3 Energy levels resulting from the Zeeman effect and hyperfine splitting for an $S = 1/2$ electron and $I = 1$ nucleus. The 3 allowed EPR transitions are indicated by the blue arrows, corresponding to an energy gap $h\nu$. 17

2.4 Energy level diagram for an electron spin $S = 1/2$ coupled to a nuclear spin $I = 1/2$. All possible transition probabilities are shown, where w_I is the nuclear spin relaxation rate, w_S is the electron spin relaxation rate, w_2 is the double-quantum relaxation rate, w_0 is the zero-quantum relaxation rate. The microwave excitation of an electron transition is also indicated. 20

2.5 Calculated field dependence of coupling factor for pure dipolar relaxation, modeled with rotational (solid black line) and translational (dashed blue line) diffusion, using a correlation time $\tau = 20$ ps. . . . 25

3.1 Theoretical field dependence of coupling factors, calculated using a 20 ps correlation time (from Reference [33]). Top 2 lines — pure dipolar relaxation mechanism, modelled with rotational and translational diffusion; bottom 4 lines — pure scalar relaxation mechanism, shown for various values of the fast electron spin relaxation correction term β. 30

4.1 94 GHz spectrometer for in-situ DNP-NMR at 3.35 T 45

4.2 Photograph of the Warwick 94 GHz DNP-NMR spectrometer. 46
4.3 Schematic of W-band microwave bridge for Bruker ELEXSYS E680 EPR system. 47
4.4 EIK amplifier characteristics. 49
4.5 Diagram of modified ENDOR probe: (1) W-band cavity, (2) RF coil, (3a,b) RF leads, (4) sample access, (5) variable tuner, (6) coupling iris, (7) waveguide to microwave assembly, (8) thermocouple [43]. . . 50
4.6 Structures of derivatives of the nitroxide free radical TEMPO. 51
4.7 Typical sample. Surface of outer capillary tube marked with red dots with a separation of 1 mm in order to ensure proper sample positioning in the sample holder and cavity. 52
4.8 One-pulse sequence. 53
4.9 Pulse sequences used to measure spin-lattice relaxation time T_1. . . 53
4.10 Example of 94 GHz CW-EPR spectrum for 100 mM TEMPOL radical in water at room temperature. 55
4.11 Typical pulse sequence for Overhauser DNP experiments. 56
4.12 Schematic of the microwave assembly utilising two microwave sources. The orange coloured components were added as the second microwave source, whilst the blue coloured components constitute the original setup for the experiments in Chapters 5 and 6. 57
4.13 Output of low-power side of Bruker W-band bridge in CW-mode, measured using Hewlett Packard power meter. 59
4.14 Output of high-power side of Bruker W-band bridge in pulse-mode, measured using Hewlett Packard power meter at the bridge and at the magic-T output. The loss in microwave power in travelling from the bridge through to the magic-T output is plotted in red (diamonds) and corresponds to the right-hand axis. 59
4.15 Output of magic-T when used with two sources simultaneously. The contributions to the total input power from each source is approximately equal. 60
4.16 Agilent frequency 'sweep' in which DNP enhancement is plotted as a function of frequency; used to determine the required input frequency for two-source DNP experiments. DNP experiments were conducted on 5 mM 4-oxo-TEMPO-d_{16}-^{15}N in toluene at room temperature. . . 60

5.1 ^{1}H NMR spectra of water with 120 mM TEMPOL; top — no microwave irradiation, 100 acquisitions; bottom — 1.3 W microwave irradiation for one second, single acquisition. 64
5.2 Water proton spin-lattice relaxation rates. 67
5.3 Proton chemical shift and inferred temperature in water as a function of duration of 1.3 W microwave irradiation, for different concentrations. Dotted line — fit of the form $(1-\exp(-t/\tau_T))$ with $\tau_T = 0.25$ s. The inset shows the same data for 80 mM and 120 mM over an extended irradiation period. 68
5.4 Enhancement as a function of 1.3 W microwave irradiation time for different radical concentrations. Dotted lines are single exponent fits of the data with time constants τ displayed. The inset shows the first second of irradiation for concentrations of 120 mM, 80 mM and 40 mM. The dotted line is once again a single exponent fit. 69
5.5 Evolution of nuclear spin polarisation with 1.3 W microwave irradiation. Enhancement values are corrected for the change in Boltzmann factor with temperature increase. 71
5.6 CW-EPR spectra of TEMPOL in water recorded at different temperatures, at two radical concentrations. 72
5.7 DNP enhancement as a function of magnetic field for a sample of water with 120 mM TEMPOL, 10 mm length. 1 s microwave irradiation. Circles — 1.3 W, 130°C; squares — 0.25 W, 40°C. Lines are integrated CW-EPR spectra: solid line — 98°C; dashed line — 22°C. 72
5.8 Simulations fitted to experimental data of DNP enhancement in water with 100 mM TEMPOL resulting from 1.3 W microwave irradiation. 75

6.1 Skeletal formula of glycine (NH_2CH_2COOH). 82
6.2 ^{1}H NMR spectrum of 3 M glycine-100 mM TEMPOL-D_2O sample: no microwave irradiation, 40,000 acquisitions, 7.0 ± 0.5°C. 83
6.3 DNP-enhanced ^{1}H NMR spectrum of 3 M glycine-100 mM TEMPOL-D_2O. $\sim$1.1 W applied microwave power, 400 acquisitions, 101 ± 3°C. 84
6.4 Overlay of DNP-enhanced spectra, illustrating the increasing enhancement and temperature of both HDO and CH_2 protons. The DNP spectra have been normalised to the same number of acquisitions (multiplication factor shown in figure) and the thermal equilibrium signal increased by a factor of 5 for comparison. 85

6.5 DNP enhancement as a function of temperature, as calculated from the chemical shift. Dashed lines — linear fits with slopes of -1.01 and -0.30 for HDO and CH_2 protons, respectively. Ratio of slopes $m_{HDO}/m_{CH_2} = 3.4 \pm 0.5$. 86
6.6 Saturation-recovery experiment at 143 MHz. Sample temperature is 100 ± 3°C. Dashed lines — fit of the form $(1 - \exp(-t/T_{1I}))$ with resulting nuclear relaxation times displayed in the figure. 88
6.7 Temperature dependence of proton T_1 of HDO and CH_2 in water with 3 M glycine and 100 mM TEMPOL at 143 MHz. Data are shown with temperature indicated by chemical shift. The T_1 of pure water is shown as a dotted line and has been scaled to agree with the glycine-TEMPOL-D_2O sample value at 63°C. 88
6.8 Room temperature T_{1I} values of 3 M glycine-D_2O at 143 MHz, interpolated from measurements made at 100 MHz and 300 MHz. 90
6.9 Skeletal formula of L-proline ($C_5H_9NO_2$). 92
6.10 ^{1}H NMR spectrum of 1 M L-proline-100 mM TEMPOL-D_2O sample: no microwave irradiation, 48,000 acquisitions, 6.0 ± 0.5°C. 93
6.11 DNP-enhanced ^{1}H NMR spectrum of 1 M L-proline-100 mM TEMPOL-D_2O. $\sim$0.4 W applied microwave power, 200 acquisitions, 70 ± 3°C. 94
6.12 Overlay of DNP-enhanced spectra, demonstrating the increase of enhancement and temperature of HDO, C-CH_2-N and C-CH_2-C protons. The DNP spectra have been normalised to the same number of acquisitions and the thermal equilibrium spectrum (multiplied by a factor of 5) is displayed on top for comparison. 95
6.13 DNP enhancement as a function of temperature, as calculated by chemical shift change. Dashed lines — linear fits with slopes of -1.31, -0.48, -0.08 and -0.26 for HDO, C-CH_2-N, C-CH_2-C and Peak Y protons, respectively. Ratio of slopes $m_{HDO}/m_{\text{C-CH}_2\text{-N}} = 2.8 \pm 0.4$, $m_{HDO}/m_{\text{C-CH}_2\text{-C}} = 15.8 \pm 0.7$, $m_{HDO}/m_Y = 5.1 \pm 0.6$. 96
6.14 Effect of temperature on proton T_{1I} of HDO and C-CH_2-C in water doped with 100 Mm TEMPOL and 1 M L-proline. Data are shown with the temperature calculated from chemical shift, and have an uncertainty of approximately ± 3°C. The T_{1I} of pure water has been included, and scaled to agree with the sample value at 11°C, for comparison. 97
6.15 Skeletal formula of acrylic acid ($CH_2CHCOOH$). 99

6.16 ^{1}H NMR spectrum of acrylic acid-D_2O(10:90 % v/v)-100 mM TEMPOL sample: no microwave irradiation, 100,000 acquisitions, 6.0 ± 0.5°C. 100
6.17 The reduction of TEMPOL by acrylic acid, resulting in the formation of the diamagnetic TEMPOL-H molecule. 101
6.18 DNP-enhanced ^{1}H NMR spectrum of acrylic acid-D_2O-100 mM TEMPOL. ∼1.7 W applied microwave power, 400 acquisitions, 83 ± 3°C. 101
6.19 Overlay of DNP-enhanced spectra, showing the increasing enhancement of HDO and AA protons, whilst showing the changing shift of HDO and constant position of AA. The DNP spectra have been normalised to the same number of acquisitions and the thermal equilibrium signal (top) increased by a factor of 5 for comparison. 102
6.20 Change in nuclear spin-lattice relaxation time as a function of time, due to reduction of TEMPOL. Measured at room temperature at 284 MHz. 103
6.21 Evolution of integrated X-band EPR signal intensity with time, showing a continuous degradation of TEMPOL radical at room temperature. Inset — expansion of the first 275 minutes after the sample was prepared. 104
6.22 Temperature dependence of DNP enhancement, with temperatures calculated from change in chemical shift of water protons. Dashed lines — linear fits with slopes of -0.72, -0.34 and -0.14 for HDO, AA and CH_3 protons, respectively. Ratio of slopes $m_{\mathrm{HDO}}/m_{\mathrm{AA}} = 2.1 \pm 0.2$, $m_{\mathrm{HDO}}/m_{\mathrm{CH_3}} = 5.3 \pm 5.3$. 105
6.23 Temperature dependence of proton $T_{1\mathrm{I}}$ of HDO and AA protons in D_2O with acrylic acid and an initial radical concentration of 100 mM TEMPOL which is thought to have reduced by at least ∼40%. Data are shown with temperatures indicated by HDO chemical shift. The $T_{1\mathrm{I}}$ of pure water is shown as a dotted line and has been scaled to agree with the sample value at 4°C. 107
6.24 $T_{1\mathrm{I}}$ values of acrylic acid-D_2O (10:90 % v/v) at 143 MHz at room temperature, interpolated from measurements made at 100 MHz and 300 MHz. 108

7.1 Skeletal formula of toluene ($C_6H_5CH_3$). 116

7.2 Source A frequency sweep of 5mM 4-oxo-TEMPO-d_{16}-^{15}N in toluene, used to find electron resonance frequencies at fixed magnetic field. $P_A \approx 429$ μW, Source B off. Arrows — frequencies used in later experiments corresponding to irradiating: off-resonance (1, 5); allowed EPR transitions (2, 4); and forbidden transitions (3). ν_i = 94.070, 94.155, 94.183, 94.211, 94.300 GHz; for i = 1, 2,... 5. 117
7.3 Dual irradiation experiment with Source B irradiating on-resonance at ν_4 with constant power ($P_B \approx 78$ μW), whilst simultaneously ramping Source A power ($P_A \approx$ 10–429 μW) off-resonance at ν_1. Inset — measured diode voltages indicating transmitted and reflected power. 118
7.4 Irradiation of both hyperfine lines. Source B at ν_4 with constant power ($P_B \approx 78$ μW), ramping Source A power ($P_A \approx$ 10–429 μW) at ν_2. 118
7.5 Source A frequency sweep of 2.5 mM TEMPOL in toluene, used to find electron resonance frequencies at fixed magnetic field. $P_A \approx P_B \approx 78$ μW. Arrows — frequencies used in later experiments corresponding to irradiating: off-resonance (1, 7); the allowed EPR transitions (2, 4, 6); and forbidden transitions (3, 5). ν_i = 94.100, 94.163, 94.185, 94.205, 94.230, 94.246, 94.300 GHz; for i = 1, 2,... 7. 121
7.6 Dual irradiation experiment with Source B irradiating central transition (ν_4) with constant power ($P_B \approx 78$ μW), whilst simultaneously ramping Source A power ($P_A \approx$ 10–429 μW) off-resonance at ν_1. . . 122
7.7 Irradiation of two hyperfine lines. Source B at central transition (ν_4) with constant power ($P_B \approx 78$ μW), ramping Source A power ($P_A \approx$ 10–429 μW) at low frequency transition (ν_2). 122
7.8 Schematic of part of the microwave assembly, showing the addition of a calibrated variable attenuator used to measure relative output powers of the EIK, cf. Figure 4.12. 125
7.9 Change in EIK output power corresponding to a 10 dB increase in input power, for varying levels of total power. As measured using a calibrated variable attenuator and diode power detector. 126
7.10 Frequency dependence of EIK amplifier output. Measured with single microwave source (Source A) using constant power $P_A \approx 429$ μW. Frequency of allowed EPR transitions for two TEMPO-derived radicals are shown. 126

Acknowledgments

Firstly, I would like to thank my supervisors Prof. Mark Newton, Prof. Ray Dupree and Prof. Mark Smith for their guidance.

I am grateful to the Warwick Solid State NMR Group, particularly the members of the DNP Project: Dr. Thomas Kemp, Dr. Eugeny Kryukov, Dr. Hiroki Takahashi, Dr. Radoslaw Kowalczyk and Dr. Andrew Howes for all their help throughout my PhD. Special thanks to my unofficial supervisor — Dr. Kevin Pike. I would also like to thank William Woodruff for his collaboration and Dr. Graham Smith and Dr. David Bolton for kindly lending me their equipment without which the final stages of my work would not have been complete.

I am incredibly thankful to my family and friends for their support and encouragement. To my wife Szevone, thank you for your love and companionship.

Finally, my deepest thanks go to my parents for their never-ending support and patience, this would not have been possible without you.

Declarations

I declare that the work presented in this thesis is my own except where stated, and was carried out entirely at the University of Warwick, during the period of October 2009 to March 2013, under the supervision of Prof. Mark E. Newton, Prof. Ray Dupree and Prof. Mark E. Smith. The research reported here has not been submitted, either wholly or in part, in this or any other academic institution for admission to a higher degree.

Some parts of the work reported in this thesis have been published in the following paper:

E. V. Kryukov, K. J. Pike, T. K. Y. Tam, M. E. Newton, M. E. Smith and R. Dupree, *Determination of the temperature dependence of the dynamic nuclear polarisation enhancement of water protons at 3.4 Tesla*, Phys. Chem. Chem. Phys., **13**, 4372-4380 (2011).

Abstract

Studies of Overhauser DNP in liquids are presented in this thesis, where the polarisation is achieved in-situ using TEMPO-derived radicals at a magnetic field of 3.4 T (143 MHz/94 GHz ^{1}H NMR/EPR frequency).

The dielectric heating of lossy water solvent is unavoidable at high field, and so knowledge of temperature effects is important to properly compare enhancement results. It is shown that the temperature dependent DNP enhancement of water protons can be determined provided that the ^{1}H NMR shift is sufficiently resolved and the nuclear relaxation $T_{1\mathrm{I}}$ is sufficiently fast. Considerable sensitivity gains are made at modest temperatures, e.g. $|\varepsilon| \sim 40$ at $\sim$40°C, and much greater enhancements are achievable at elevated temperatures, e.g. $|\varepsilon| \sim 130$ at $\sim$100°C. Since high radical concentrations (100 mM TEMPOL) are used, the leakage and saturation factors approach 1, enabling an experimental determination of the coupling factor from the enhancement. A value of $\xi = 0.055 \pm 0.003$ is found at 25°C, which agrees well with values in the literature calculated from molecular dynamics simulations.

The DNP enhancement is measured as a function of temperature for three organic compounds dissolved in water: glycine, L-proline and acrylic acid; with enhancements of -17, -16 and -11 at $\sim$40°C. To the author's knowledge, this is the first report of solute molecule enhancements for direct in-situ liquid DNP at this field. Significant enhancements are obtained, however, further analysis of the results reveals significantly weaker coupling of the electron spin to the solute molecule protons than to the solvent molecule protons. Discrepancies between experimental coupling factor ratios and those calculated from a force-free hard-sphere model suggest that the classical analytical models used to describe Overhauser DNP may require refinement.

In addition to these temperature studies, simultaneous saturation of two EPR hyperfine lines is investigated and achieved, resulting in an increase in observed DNP enhancement.

Abbreviations

ADC	Analogue-to-Digital Converter
BDPA	Bisdiphenylene-β-phenylallyl
BPA	Bisphenol A
bTbK	Bis-TEMPO-Bis-Ketal
BWO	Backward Wave Oscillator
CSA	Chemical Shift Anisotropy
CW	Continuous Wave
DNP	Dynamic Nuclear Polarisation
DPPH	2,2-diphenyl-1-picrylhydrazyl
EIK	Extended Interaction Klystron
ELDOR	Electron Electron Double Resonance
ENDOR	Electron Nuclear Double Resonance
EPR	Electron Paramagnetic Resonance
FFHS	Force-Free Hard-Sphere (model)
FID	Free Induction Decay
FPR	Fabry-Perot Resonator

FWHM	Full Width at Half Maximum
HPNO	4-hydroxy-2,2,6,6-tetramethyl piperid-1-yloxy
ID	Inner Diameter
IF	Intermediate Frequency
MAS	Magic Angle Spinning
MD	Molecular Dynamics
NMR	Nuclear Magnetic Resonance
NMRD	Nuclear Magnetic Relaxation Dispersion
OD	Outer Diameter
OE	Overhauser Effect
PEDRI	Proton-Electron Double-Resonance Imaging
ppm	Parts Per Million
r.f.	Radio-Frequency
SMI	Source Module Interface
SNR	Signal-to-Noise Ratio
TAM	Triarylmethyl
TEMPOL	4-hydroxy-2,2,6,6-tetramethyl piperidine (4-hydroxy-TEMPO)
TWT	Travelling Wave Tube

Chapter 1

Introduction

> *"Overhauser proposed ideas of startling originality, so unusual that they initially took portions of the scientific community back, but of such depth and significance that they opened vast new areas of science."*
>
> — Citation for honorary degree conferred on Dr. Albert Warner Overhauser by the University of Chicago (1979) [1].

Since the 1940s, nuclear magnetic resonance (NMR) spectroscopy has proven to be a remarkably effective and versatile analytical technique and as technological innovations have been made, so too have advances in NMR. Sensitivity, in particular, has improved greatly with the development of magnet technology — fields ∼20 T are not uncommon in modern-day NMR. However, even at these high field strengths NMR remains an intrinsically insensitive technique, in contrast to the analogous electron paramagnetic resonance (EPR) spectroscopy which exploits the much larger magnetic moment of the electron. For example, in order to reach comparable levels of polarisation achievable with electrons at room temperature in a 3.4 T magnetic field; ^{1}H NMR (protons having the highest γ of commonly studied nuclei) would have to be conducted at liquid helium temperatures (∼4 K) in a field of 30 T. Whilst such low-temperature NMR studies are often performed, suitably homogeneous magnetic fields ∼30 T are well beyond the current state-of-the-art. Overcoming these sensitivity limitations has been a major goal in NMR, and hyperpolarisation via microwave-driven dynamic nuclear polarisation (DNP) has had much success in this area.

1.1 Development of microwave-driven DNP

1.1.1 Early experiments

DNP was first proposed in 1953 by Overhauser in his seminal paper "Polarization of Nuclei in Metals" [2], and was experimentally confirmed in the same year by Carver and Slichter [3]. It was initially suggested as a phenomenon observable in metals where the saturation of conduction electron spins permitted polarisation transfer to nuclei via relaxation processes. Later, this concept would be extended to include the solution-state [4], the condition under which most Overhauser DNP work is now done. For the first three decades or so after the discovery of this 'Overhauser effect', many experiments were carried out in metals and liquids. Perhaps some of the most important liquid DNP results in the early stages of this emerging field came from Hausser and co-workers [5, 6], who predicted a steep drop in DNP efficiency (more specifically, the electron-nuclear coupling) at higher microwave excitation frequencies, i.e. higher magnetic field strengths. The data available at the time all seemed to support Hausser's prediction.

As NMR technology improved and superconducting magnets became available at greater and greater fields, Overhauser DNP no longer seemed to be a pragmatic solution to improving NMR sensitivity; it was easier to simply go to higher magnetic fields, where spectral resolution is also enhanced. Moreover, a lack of availability of microwave sources able to produce sufficiently strong and stable microwaves at the high frequencies necessary for the common NMR fields of the time prevented investigations beyond 1.3 T. DNP seemed to have, for the time being, reached its limits.

1.1.2 Modern revival

The development of NMR spectrometers operating at increasingly high magnetic field strengths is a lengthy process which, for example, took approximately 20 years for the state-of-the-art to increase from 10 T to 20 T [7]. The rate of development appears to have been relatively slow in recent years and the limits of what is practically achievable with the current technology may be fast approaching [8]. The nuclear spin polarisation, even at today's highest field strengths, is still much less than 1%; so in order for NMR to further push the boundaries of what is possible and open up to new areas of application, it seems advances in methodology may need to play a greater role rather than adopting a 'brute force' approach. Hyperpolarisation by dynamic nuclear polarisation is one such method.

The field of DNP was revitalised by the work of the Griffin group at the

Massachusetts Institute of Technology who utilised a novel microwave source — a cyclotron resonance maser or gyrotron — to successfully conduct DNP experiments at high fields (5 T) in the solid-state [9]. This new type of microwave source (for DNP) was later used for solution-state Overhauser DNP experiments at 5 T [10]. Modern DNP research was further invigorated by Ardenkjaer-Larsen and co-workers when they reported massive (∼10,000) signal enhancements at high field (3.4 T) in the liquid-state using a novel experimental design — now commonly referred to as 'dissolution DNP'. Following these landmark results, DNP became the subject of intense focus in the magnetic resonance community and has begun to 'catch up' with modern magnetic fields, allowing never-before-achieved levels of sensitivity in NMR.

1.2 Thesis overview and motivation

This thesis is focused solely on DNP-enhanced NMR in the solution-state, driven by the Overhauser effect mechanism. Over the last decade or so, liquid DNP has shown the potential to be a useful analytical tool at high fields, with sizable enhancements being reported at fields up to 9.2 T [11, 12]. However, there still remain some doubts as to its applicability. For instance, whilst high DNP enhancements have been observed for solvents into which polarising agents are dissolved, there is little data in the literature regarding the polarisation of other solute compounds in the sample. The high-field DNP data that is available has called into question the validity of the theoretical framework in which the Overhauser effect has been traditionally described: enhancements are actually higher than expected. The work presented here aims to address some of these issues, the organisation of which is described below.

The theoretical background to the relevant areas of magnetic resonance is given in Chapter 2, and should provide the basic physics required to understand the experimental results and conclusions. Chapter 3 provides an overview of the progress made in dynamic nuclear polarisation in the last 60 years. The emphasis is strongly on liquid DNP developments, providing a context for the present work. Chapter 4 gives specific details of the equipment and methods used to study the chosen systems, particularly the use of any non-standard hardware and procedures. In Chapter 5, results are presented for a study of water protons with the nitroxide radical TEMPOL (4-hydroxy-2,2,6,6-tetramethyl piperidine). Substantial enhancements are reported reaching a factor of >100 times the thermal equilibrium signal. The temperature dependence of the Overhauser DNP enhancement was measured

and a method for determining the maximum enhancement and coupling factor is demonstrated. The work in Chapter 6 continues with temperature dependent DNP studies, but on organic molecules dissolved in water in addition to the usually studied solvent molecules. The enhancement of solvent and solute molecules is compared, and the magnitude of enhancement attainable for small (solute) target molecules over a range of temperatures is reported. These results, the first of their kind at 3.4 T (to the author's knowledge), give an indication of the possible applicability of this type of DNP to larger molecules at physiological temperatures. In Chapter 7, the effect of simultaneous irradiation of two EPR resonances is investigated, with the aim of increasing the effective electron spin saturation, thereby generating greater enhancement of the NMR signal. The potential benefits of constructing such a dual irradiation system are discussed. This is believed to be the first study of this type at 3.4 T (having been attempted once previously by Höfer's group at 0.35 T [13]). Finally, the main findings of this thesis are summarised in Chapter 8, followed by a discussion of possible continuation of the work.

Chapter 2

Theoretical background

2.1 Nuclear magnetic resonance

Nuclear magnetic resonance (NMR) spectroscopy was first utilised in solids in 1946 by Bloch et al. [14] and Purcell et al. [15]. Since its inception, many advances have been made in both technology and methodology to improve the sensitivity of this technique. Dynamic nuclear polarisation (DNP) is one such method, which is the topic of this thesis, and the theory of which will be addressed later in this chapter. First, some theoretical background of NMR will be presented as it is the basis of all DNP experiments. Further information can be found in References [16], [17], [18], [19], [20], [21], [22] and [23].

2.1.1 Spin angular momentum and nuclear magnetism

Magnetic nuclei have an intrinsic property called spin angular momentum characterised by the spin quantum number I, which can take either integer or half-integer values (i.e. $I = 0, 1/2, 1, 3/2, \ldots$). The magnitude of this spin is quantised in units of $\hbar$ and is equal to $\sqrt{I(I+1)}\hbar$.

The vast majority of elements on the periodic table have at least one isotope with spin $I > 0$, making NMR an incredibly powerful tool for probing the structures and dynamics of materials. For example, the most abundant isotope of hydrogen, ^{1}H (i.e. a proton), has spin $I = 1/2$. Neutrons are also spin-1/2 particles, and the total spin of a nucleus is the sum of the proton and neutron spin contributions. However, for any given nucleus, there exists numerous possible configurations of the spins (parallel or anti-parallel). Calculating the lowest energy nuclear spin state of all these possibilities (the ground state) is not usually possible and is generally considered an empirical property of each isotope. Closely connected to a spin angular

momentum is a magnetic moment $\boldsymbol{\mu}$:

$$\boldsymbol{\mu} = \gamma \boldsymbol{I} \tag{2.1}$$

where the constant γ is called the gyromagnetic (or magnetogyric) ratio, which can take either a positive or negative value for a given nucleus.

In a sample containing magnetic nuclei, the distribution of the direction of spin angular momentum vectors (the spin polarisation axes) and, therefore, the magnetic moments, will be isotropic in the absence of a magnetic field. If a field is externally applied, the magnetic moments will begin to precess about the field on a cone of constant angle dependent on the initial angle of the spin polarisation. The rate of this precession is given by

$$\omega_0 = -\gamma B \tag{2.2}$$

where the angular frequency ω_0 is the precession frequency known as the Larmor frequency, and B is the magnetic field at the nucleus.

2.1.2 Zeeman splitting

The spin angular momentum $\boldsymbol{I}$ can be considered as a vector with $2I+1$ projections onto an arbitrary axis, usually chosen to be the z-axis. In that case, the z-component is quantised by the magnetic quantum number m_I so that

$$I_z = m_\mathrm{I} \hbar \tag{2.3}$$

where m_I takes $2I+1$ values between I and $-I$ in integer steps (e.g. for ^{14}N, $I = 1$, so there exists three allowed states for the spin $I_z = -\hbar, 0, \hbar$), and $\hbar$ is the Planck constant divided by 2π.

Upon the application of an external magnetic field $\boldsymbol{B_0}$, the degeneracy of the $2I + 1$ spin states of the nucleus is lifted, and the nuclear ground state is split into sublevels by the Zeeman effect. In this field, the energy of a magnetic moment is given by the scalar product of magnetic moment and the magnetic field. If the magnetic field is assumed to be in the z-direction, so $\boldsymbol{B_0} = (0, 0, B_z)$ the energy is

$$E = -\mu_z B_0 = -m_\mathrm{I} \hbar \gamma B_0 \tag{2.4}$$

The selection rule for allowed NMR transitions is $\Delta m_\mathrm{I} = \pm 1$, resulting in the reso-

nance condition

$$\Delta E = h\nu = \hbar\gamma B_0 \tag{2.5}$$

where ν is the electromagnetic radiation frequency used to excite transitions.

2.1.3 Longitudinal magnetisation

The bulk magnetisation of a sample is the vector sum of the individual magnetic moments, $\boldsymbol{M} = \sum_i \boldsymbol{\mu_i}$, which is zero in the absence of an applied magnetic field due to the isotropic distribution of spins. This situation changes as an external field is applied. Not only do nuclear spins experience the applied field, they also experience small local fields from other magnetic particles (i.e. the magnetic moments of unpaired electrons and other nuclei) which fluctuate due to thermal motion. This allows the angle of each cone of precession to vary, with a slight bias towards parallel alignment of the magnetic moments with the magnetic field, i.e. towards to the lowest energy state — thermal equilibrium.

So the application of an external magnetic field causes the sample to 'relax' from its initial state of equilibrium towards a new thermal equilibrium, resulting in a bulk magnetisation in the direction of the external field (typically defined to be the z-direction). The build up of this longitudinal magnetisation M_z, as a function of time t, is given by

$$M_z(t) = M_0(1 - \exp(-t/T_1)) \tag{2.6}$$

where M_0 is the equilibrium magnetisation in the z-direction and T_1 is a time constant for the spin-lattice or longitudinal relaxation process (see Section 2.1.5).

For a sample of $I = 1/2$ nuclei, such as ^{1}H, two energy states exist ($m_\mathrm{I} = \pm 1/2$). The probability of occupation of these states is given by the Boltzmann distribution and the polarisation can be defined as [24]:

$$p = \frac{N_{+1/2} - N_{-1/2}}{N_{+1/2} + N_{-1/2}} = \frac{\exp(-E_{1/2}/kT) - \exp(-E_{-1/2}/kT)}{\exp(-E_{1/2}/kT) + \exp(-E_{-1/2}/kT)} = \tanh\left(\frac{\gamma\hbar B_0}{2kT}\right) \tag{2.7}$$

where N_i is the probability of a nuclear spin occupying the i^{th} state, k is the Boltzmann constant, and T is the temperature in Kelvin. From Equation 2.7, it can be seen that NMR is an inherently insensitive technique, e.g. for ^{1}H nuclei in a 3.4 T field, at room temperature, $p = 0.0012\%$. In contrast, the much larger γ for electrons gives a much greater population difference and a polarisation $p = 0.78\%$. It is this fact which DNP takes advantage of (see Section 2.3). To approach similar nuclear polarisations would require very high fields and low temperatures, e.g. ^{1}H polarisation at 20 T at a temperature of 4 K is 0.51%.

2.1.4 Transverse magnetisation

A bulk longitudinal magnetisation is not practically detectable in NMR (at high fields) due to its cylindrically symmetric nature. A transverse magnetisation is therefore generated by rotating all the spin polarisations by 90° about, say, the x-axis. The result is a bulk magnetisation along the $-y$-axis, with the spins precessing about the z-axis on a plane perpendicular to $\boldsymbol{B_0}$ at the Larmor frequency ω_0. The motion of this transverse magnetisation is described by the following equations:

$$M_x = M_0 \sin(\omega_0 t) \exp(-t/T_2) \tag{2.8}$$

$$M_y = -M_0 \cos(\omega_0 t) \exp(-t/T_2) \tag{2.9}$$

where T_2 is the time constant for spin-spin or transverse relaxation, which takes into account the decay of the transverse magnetisation (see Section 2.1.5).

This transverse magnetisation is generated by use of a r.f. (radio-frequency) pulse carried in the wire coil of a probe in the NMR spectrometer, whose winding axis is perpendicular to the main magnetic field. This creates a time-dependent oscillating field, which can be represented by two vectors rotating with frequency $\pm\omega_{\mathrm{rf}}$, in opposite directions on the xy-plane of the laboratory reference frame. The component rotating in the same sense as the precessing magnetisation is known as the B_1 field; whilst the other (counter-rotating) component will have very little interaction with the bulk magnetisation and can be neglected since it is far from resonance.

Consider transferring from the laboratory frame (x, y, z) to a reference frame (x', y', z') rotating about the z-axis with frequency $\omega_{\mathrm{rf}} = \omega_0$. Both the B_1 field and the bulk magnetisation would then appear to halt their precessing motion, and $\boldsymbol{M}$ would then precess about $\boldsymbol{B_1}$. Adjusting the strength and length of the r.f. pulse used allows the magnetisation to be rotated through any angle. This 'flip angle' θ_{p} is given by the relation:

$$\theta_{\mathrm{p}} = -\gamma B_1 t \tag{2.10}$$

where t is the duration of the pulse.

2.1.5 Spin relaxation

When a system of nuclear spins is perturbed from thermal equilibrium, e.g. by a resonant r.f. field, it experiences transitions that will tend to restore it to equilibrium over time.

Spin-lattice relaxation — T_1

After an r.f. pulse, the bulk magnetisation will undergo spin-lattice (or longitudinal) relaxation back to equilibrium along the $\boldsymbol{B_0}$ direction. In a time T_1, the magnetisation will have returned to approximately 63% ($\approx 1-(1/e)$) of its initial value. This process requires the flipping of nuclear spins and an exchange of energy between the excited spins and surrounding environment (or 'lattice'). So T_1 is a measure of the time taken for the nuclear spins to transfer the energy they gained from the r.f. pulse to the rest of the sample. T_1 is critical in setting up an NMR experiment as it determines how quickly scans can be repeated and, hence, the signal-to-noise ratio achievable in a given time frame.

For $I = 1/2$ nuclei, such as ^{1}H, there are three main causes of spin-lattice relaxation: the dipolar interaction, where the local magnetic fields at the nucleus vary in time due to the motion of nearby spins; the chemical shift anisotropy, where the chemical shielding due to the surrounding electron density fluctuates with molecular motion; and spin-rotation interactions, where the tumbling of molecules causes the circulating electron and nuclear charges to generate small fluctuating magnetic fields at the nucleus. Of these interactions, the dipolar interaction usually has the greatest effect.

In order for energy to be transferred to the lattice, there must be a component of the randomly fluctuating magnetic field (caused by motion) at the Larmor frequency to induce transitions which eventually allow the spins to return to equilibrium. The random molecular tumbling motion has a range of frequencies, and the probability of a component of that motion occurring at a given frequency is described by the spectral density $J(\omega)$ (see Figure 2.1). The typical frequencies of motion in liquids are much greater than nuclear Larmor frequencies, so only the relatively low proportion of slow molecular motions contribute to spin-lattice relaxation, making it a relatively slow process. The precise form of the spectral density function is usually unknown, but often assumed to be Lorentzian, with the correlation time τ_c of the fluctuations then assumed to be exponential. A plot of T_1 as a function of τ_c is given in Figure 2.2.

It can be seen from Figure 2.2 that there is a maximum relaxation rate which occurs when $1/\tau_c$ matches the Larmor frequency, i.e. $\omega_0\tau_c = 1$. This can be understood by examining the spectral density function in various regimes of motion (Figure 2.1). When the molecular tumbling is slow ($\omega_0\tau_c \gg 1$) only a small component of the motion is at the Larmor frequency. As the motion becomes more rapid, a larger proportion is at ω_0, eventually reaching some optimum value. Beyond this, as the rate of tumbling increases ($\omega_0\tau_c \ll 1$), the component at ω_0 decreases

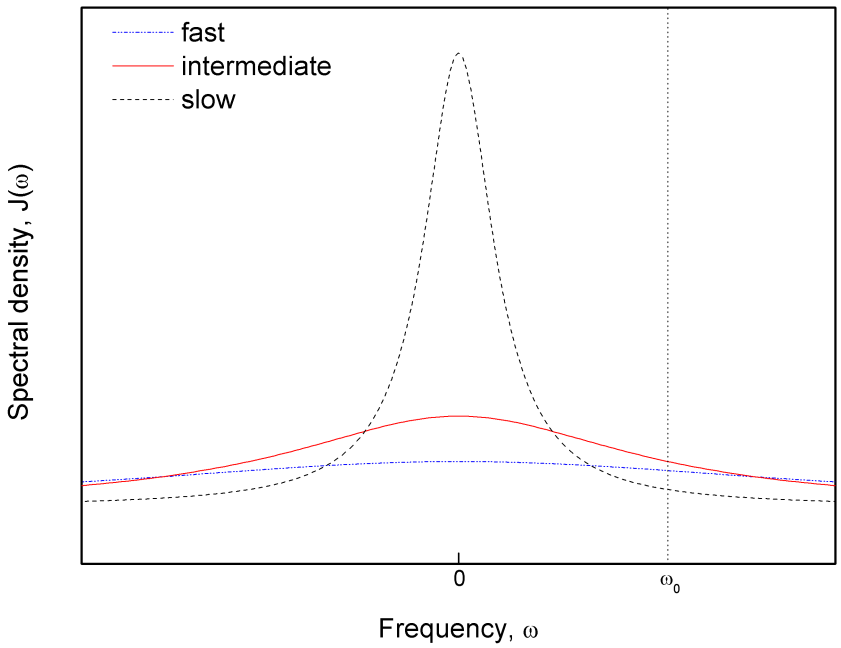

Figure 2.1: Lorentzian spectral density functions showing molecular motion in the slow, intermediate and fast regimes.

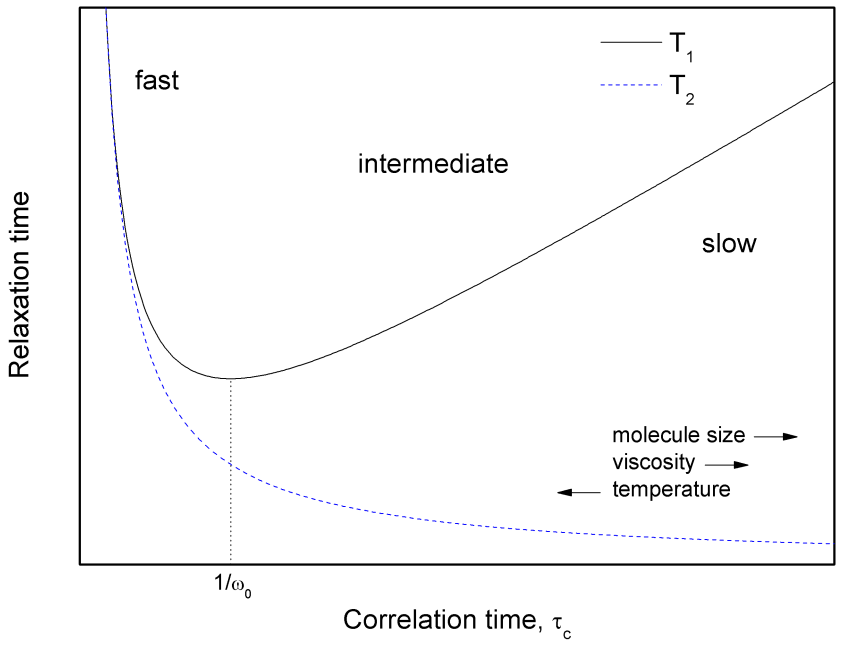

Figure 2.2: Plot illustrating the variation of the spin-lattice ($1/T_1 \propto \tau_c/(1+(\omega_0\tau_c)^2)$) and spin-spin ($1/T_2 \propto 3J(0)+5J(\omega_0)+2J(2\omega_0)$) relaxation time constants with the correlation time of molecular motion [16]. Regions for slow, intermediate and fast motion are indicated, as well as the effect of increasing molecule size, liquid viscosity and temperature on relaxation.

thereby reducing the relaxation rate.

It should be noted that the regions of slow tumbling correspond to low temperatures, large molecules and high viscosity liquids, and the regions of fast tumbling to high temperatures, small molecules and low viscosity liquids. This is indicated in Figure 2.2.

Spin-spin relaxation — T_2

Spin-spin (or transverse) relaxation describes the decay of transverse magnetisation and is characterised by the exponential time constant T_2. It is a result of the slightly different local magnetic fields experienced by each spin, which causes a gradual dephasing of the magnetisation in the xy-plane. The process involves no energy exchange with the lattice (in contrast to T_1 processes), only the redistribution of energy amongst the spins (hence 'spin-spin' relaxation).

In liquids, the physical processes responsible for longitudinal and transverse relaxation are often the same, so T_1 and T_2 are often the same. However, there can be additional transverse relaxation caused by chemical exchange or J-coupling modulated by chemical exchange or fast longitudinal relaxation of the coupled nucleus. Spin-spin relaxation, like spin-lattice relaxation, is sensitive to field fluctuations at ω_0; but in addition, it is also sensitive to fluctuations at $\omega \sim 0$ [22]. So in the case of fast motion, T_1 and T_2 are equal, but as the motion significantly slows down (and the spectral density has a larger low frequency component) T_2 continues to fall past the T_1 minimum (see Figure 2.2).

In actuality, in real NMR experiments, the measured time constant is smaller than T_2 and called T_2^*. This includes the additional effect of destructive interference of spins caused by the spatial inhomogeneity present in all real applied magnetic fields.

Bloch equations

The combined effect of spin-lattice and spin-spin relaxation on the 'motion' of the bulk magnetisation $\boldsymbol{M}$ can be described using the classical, phenomenological equations known as the Bloch equations, which can be written as [20, 17]:

$$\frac{d\boldsymbol{M}}{dt} = \gamma \boldsymbol{M} \times \boldsymbol{B} - \frac{M_x \boldsymbol{i} + M_y \boldsymbol{j}}{T_2} - \frac{M_z - M_0}{T_1}\boldsymbol{k} \tag{2.11}$$

2.1.6 Internal spin interactions

In addition to the external fields applied, magnetic nuclei within a sample will also experience internal interactions from the surrounding environment. The most commonly encountered interactions in NMR are chemical shielding (CS), direct dipole-dipole coupling (DD), J-coupling (J) and quadrupolar coupling (Q). The total interaction energy of a nucleus can be expressed as the sum of the Hamiltonians for each of these interactions:

$$H_{\text{total}} = H_{\text{Z}} + H_{\text{rf}} + H_{\text{CS}} + H_{\text{DD}} + H_{\text{J}} + H_{\text{Q}} \tag{2.12}$$

where the first two terms on the right-hand side represent the Zeeman interaction with the main magnetic field and the interaction with the radio-frequency pulse, respectively. H_{Z} is usually by far the greatest at high magnetic fields.

Nuclei in different chemical environments will experience slightly different magnetic fields as a result of induced fields (proportional to the applied field B_0) from the surrounding electrons. For an atom, this effect generally reduces the total magnetic field at the nucleus, hence the term 'shielding' used to describe this phenomenon, although in molecules the net effect may be to increase the field. As a result, the local field at the nucleus is

$$\boldsymbol{B} = (1 - \sigma)\boldsymbol{B_0} \tag{2.13}$$

where σ is in general a rank-2 tensor representing the chemical shielding. However, the fast molecular motion in liquids causes σ to become a scalar quantity known as the isotropic chemical shift [21]. Equation 2.2 can now be rewritten:

$$\omega_0 = -\gamma B_0(1 - \sigma) \tag{2.14}$$

Nuclei with different chemical shielding are chemically different. This is what makes NMR so useful as an analytical tool, because the precise resonance frequency is dependent on the surrounding electron density and hence the local chemical bonds, allowing nuclei in different structural positions to be distinguished by the shifts of resonant peaks in the spectrum. The field-dependent chemical shift is usually expressed as a field-independent ratio for convenience:

$$\delta_{\text{ppm}} = \frac{\omega_0 - \omega_0^{\text{REF}}}{\omega_0^{\text{REF}}} \times 10^6 \tag{2.15}$$

where ω_0^{REF} is the Larmor frequency of some reference nucleus (either a separate

compound, or an internal reference), and the chemical shift is given in parts per million (ppm).

J-coupling, also referred to as indirect spin-spin coupling, is the interaction of two nuclear spins mediated through the electrons in chemical bonds. The corresponding Hamiltonian can be written [17]:

$$H_{\mathrm{J}} = hJ_{ij}\boldsymbol{I}_i\boldsymbol{I}_j \tag{2.16}$$

where J_{ij} is the scalar coupling constant (in Hz). This 'through-bond' interaction is isotropic so is not averaged out by the fast molecular reorientation that occurs in liquids, and is also independent of field strength. The effect can result from spin-orbital, spin-dipolar or Fermi contact interactions and causes the splitting of resonant lines in the NMR spectrum. The resulting multiplet pattern depends on the type of spins and also the number, with intensities: 1:1 for a doublet, 1:2:1 for a triplet, 1:3:3:1 for a quartet, and so on, in accordance with Pascal's triangle.

Spins can also couple through space, via a dipolar (or direct dipole-dipole) interaction. The strength of this coupling between two spins i and j is given by

$$D_{\mathrm{c}} \propto \frac{\gamma_i\gamma_j}{r_{ij}^3} \tag{2.17}$$

where r is the distance between the spins. The splitting is also dependent on the angle between the inter-nuclear vector and the applied field θ. This orientation dependence gives rise to an averaging to zero of short-range dipolar couplings in liquids due to molecular motion. Long-range couplings are still present in liquids, but are usually very weak and so are generally ignored [21]. Hence, to a good approximation

$$H_{\mathrm{DD}} = 0 \tag{2.18}$$

and line splitting due to dipolar interactions is not typically observed in liquid NMR. It does, however, play an important role in relaxation.

Quadrupolar nuclei ($I > 1/2$) possess non-spherically symmetric nuclear electric charge distributions which give rise to an electric quadrupole moment. This interacts with electric field gradients in molecules, which have electric charge distributed asymmetrically. Whilst quadrupolar coupling can cause large line splitting in solids; in liquids, to a first approximation, the interaction is averaged to zero [16]:

$$H_{\mathrm{Q}} = 0 \tag{2.19}$$

2.1.7 Detection and Fourier transformation

The rotating transverse magnetisation generated by the r.f. pulse causes an oscillating magnetic field, which in turn induces a detectable oscillating current in the transmitter/receiver coil. This is the NMR signal, known as the free induction decay (FID). In the spectrometer, this signal is mixed down with two r.f. waveforms with frequency ω_{ref} but 90° out of phase with each other. This allows the frequency of the signal to be reduced to a value, detectable by modern analogue-to-digital converters (rather than $\omega_0 \sim$ hundreds of MHz), called the resonance offset $\Omega^0 = \omega_0 - \omega_{\text{ref}}$, whilst also detecting its sign. The resulting two signals constitute the real and imaginary parts of an oscillating and decaying complex time-domain signal

$$s(t) \propto \exp((i\Omega^0 - 1/T_2)t) \tag{2.20}$$

Fourier transformation of this signal gives a complex frequency-domain signal with an absorptive and dispersive mode (real and imaginary parts) Lorentizian lineshape centred at Ω^0. The full width at half maximum (FWHM) of the absorptive-mode lineshape is given by

$$\text{FWHM} = \frac{1}{\pi T_2} \tag{2.21}$$

where FHWM is measured in Hz.

The signal intensity in NMR is directly proportional to the number of spins in the sample N and inversely proportional to the temperature T

$$\text{signal} \propto \frac{N\gamma^3 B_0^2}{T} \tag{2.22}$$

It is also directly proportional to the number of repetitions of the experiment n; with the noise proportional to $\sqrt{n}$, the signal-to-noise ratio (SNR) is then

$$\text{SNR} \propto \sqrt{n} \tag{2.23}$$

From Equations 2.22 and 2.23 it is clear that the sensitivity of the NMR experiment can be improved in several ways: increasing the sample size, increasing the external magnetic field strength, reducing the temperature, or acquiring a larger number of scans and adding the FIDs.

2.2 Electron paramagnetic resonance

Electron paramagnetic resonance (discovered in 1945 [25]) is largely based on similar principles to NMR, except that it is electron spin transitions rather than nuclear transitions that are observed. There are also considerable experimental differences in actually carrying out the two spectroscopic techniques. Only a very brief summary of the relevant theoretical framework will be given here, with more detailed accounts of EPR theory available in References [26], [27], [28] and [29].

2.2.1 Electron spin and the Zeeman effect

The electron has a spin angular momentum $S = 1/2$, the magnitude of which is quantised in units of $\hbar$ and given by $\sqrt{S(S+1)}\hbar$. Similarly to nuclear spin, the z-component of the electron spin $S_z = m_S\hbar$ can be in one of two states, $m_S = \pm 1/2$. Associated with each electron spin, is a magnetic moment

$$\boldsymbol{\mu}_e = -g\mu_B \boldsymbol{S} \tag{2.24}$$

where g is a dimensionless quantity known as the g-factor and $\mu_B = |e|h/4\pi m_e$ is a constant called the Bohr magneton, here defined to be a positive quantity (m_e is the electron mass).

In a magnetic field of strength B_0 (conventionally defined in the z-direction), an electron spin will have an energy of

$$E = m_S g\mu_B B_0 = \pm\frac{1}{2} g\mu_B B_0 \tag{2.25}$$

and the degeneracy of the spin states will be lifted, resulting in the splitting of the energy level into two (the Zeeman effect) with an energy difference that gives the resonance condition for EPR:

$$\Delta E = g\mu_B B_0 = h\nu \tag{2.26}$$

where ν is the frequency of electromagnetic field (usually in the microwave region) used to induce transitions.

2.2.2 The g-factor

The magnetic field actually experienced by each spin will differ from the externally applied $\boldsymbol{B_0}$ field; there will also be a contribution from fields induced by (and hence dependent on the strength of) $\boldsymbol{B_0}$. This can be accounted for by replacing the field

in Equation 2.26 with an effective field:

$$\boldsymbol{B}_{\text{eff}} = \boldsymbol{B_0} + \boldsymbol{B}_{\text{local}} \tag{2.27}$$

where $\boldsymbol{B}_{\text{local}}$ is the induced field at the electron. However, it is more practical to continue using the externally applied field $\boldsymbol{B_0}$ and use an effective g-factor g that varies from the g-factor of a free electron g_{e}:

$$\boldsymbol{B}_{\text{eff}} = (1 - \sigma_{\text{S}})\boldsymbol{B_0} \tag{2.28}$$

where σ_{S} is a term analogous to the chemical shielding constant σ in NMR (see Section 2.1.6).

2.2.3 Hyperfine interaction

Measuring the g-factor provides useful information about electronic structure, but insight into the molecular structure of the sample comes from the hyperfine interaction between the electron spin and nuclear spins in the molecule. The hyperfine interaction can be split into two contributions: a Fermi contact interaction, which accounts for the hyperfine field in the region inside the nucleus and is independent of direction; and dipole-dipole interaction in the region outside the nucleus whose strength has a $1/r^3$ dependence (where r is the electron-nuclear distance) and is also orientation dependent. In liquid samples, as considered in this thesis, the dipole-dipole contribution is averaged to zero by rapid molecular tumbling. So only the Fermi contact contribution needs to be considered.

The strength of the hyperfine interaction is characterised by the hyperfine coupling constant

$$a = \frac{8\pi}{3} g\mu_{\text{B}} g_{\text{N}}\mu_{\text{N}} |\psi(0)|^2 \tag{2.29}$$

where the EPR notation $g_{\text{N}}\mu_{\text{N}}$ is equivalent to the NMR notation $\gamma\hbar$ and $|\psi(0)|$ is the wavefunction describing the motion of the electron calculated at the nucleus. In the strong field approximation ($|a| \ll g\mu_{\text{B}}B_0$), the energy of the electron spin is given by:

$$E = g\mu_{\text{B}}B_0 m_{\text{S}} - g_{\text{N}}\mu_{\text{N}}B_0 m_{\text{I}} + a m_{\text{S}} m_{\text{I}} \tag{2.30}$$

where the first and second terms on the right-hand side are the electron and nuclear Zeeman terms, respectively [27].

This interaction gives rise to the (hyperfine) splitting of EPR lines into $2I+1$ components when the electron interacts with a nucleus of spin I. For example, if an

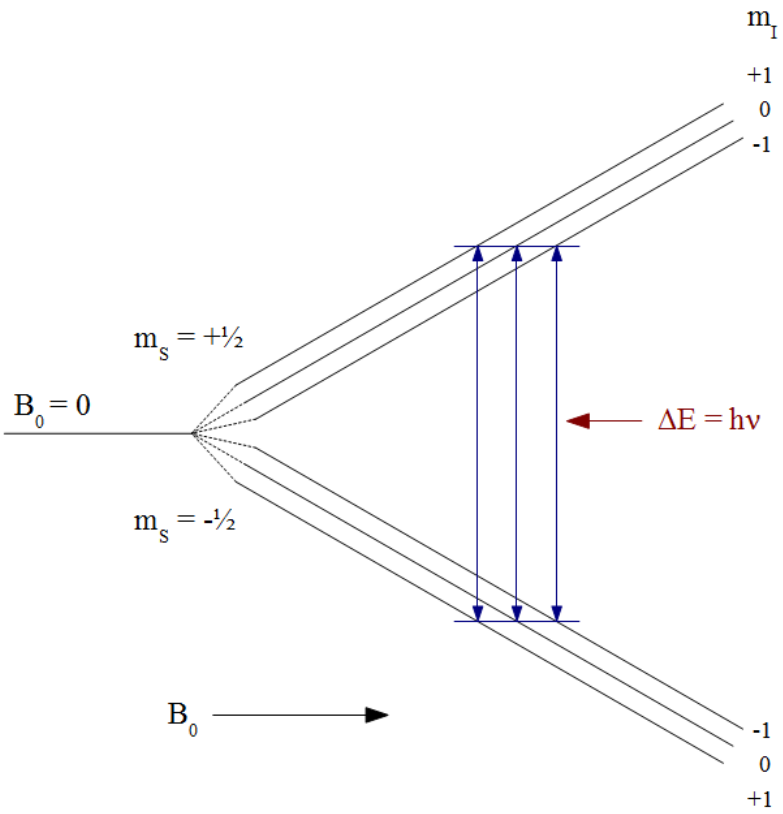

Figure 2.3: Energy levels resulting from the Zeeman effect and hyperfine splitting for an $S = 1/2$ electron and $I = 1$ nucleus. The 3 allowed EPR transitions are indicated by the blue arrows, corresponding to an energy gap $h\nu$.

electron with $S = 1/2$ is hyperfine coupled to a nucleus, such as ^{14}N, with $I = 1$ then there are 6 possible energy states, corresponding to $m_{\mathrm{S}} = \pm 1/2$ and $m_{\mathrm{I}} = -1, 0, 1$. The following selection rules then apply:

$$\Delta m_{\mathrm{S}} = \pm 1, \quad \Delta m_{\mathrm{I}} = 0 \tag{2.31}$$

for EPR transitions, and

$$\Delta m_{\mathrm{S}} = 0, \quad \Delta m_{\mathrm{I}} = \pm 1 \tag{2.32}$$

for NMR transitions. The EPR selection rule (Equation 2.31) is for allowed transitions which apply in the strong field approximation, as already mentioned. If, however, the hyperfine interaction becomes very large and $|a| \ll g\mu_{\mathrm{B}}B_0$ is no longer the case, so-called forbidden transitions ($\Delta m_{\mathrm{S}} = \pm 1, \Delta m_{\mathrm{I}} = \pm 1$) are observable (though small compared to the allowed transitions). The hyperfine splitting and allowed EPR transitions for a $S = 1/2$, $I = 1$ coupled system are shown in Figure 2.3.

2.2.4 Electron-spin exchange

The rapid tumbling motion of radicals in low viscosity solutions results in the averaging out of anisotropies and results in narrow lineshapes. For the case considered in Figure 2.3, for example, three well-resolved hyperfine lines can be observed in dilute solution. However, as the radical concentration is increased, a quantum mechanical effect known as electron-spin exchange broadens the hyperfine lines as the unpaired electrons on two different molecules swap spin orientations. Eventually this broadening results in the lines collapsing into a single broad resonance. Upon further increase of the radical concentration the line will begin to narrow (exchange-narrowing) since the spin exchange is occurring on such a rapid timescale that the average hyperfine field approaches zero [26].

2.2.5 Detection

In EPR spectrometers a resonant cavity (analogous to a coil in NMR) is used to amplify the sample signals. The efficiency of this cavity is expressed as its quality factor

$$Q = \frac{2\pi E_{\text{sto}}}{E_{\text{dis}}} \tag{2.33}$$

where E_{sto} is the energy stored and E_{dis} is the energy dissipated per microwave period. Use of a resonant cavity is especially important in liquid-state DNP, where lossy solvents such as water are frequently used, as it maximises the magnetic field whilst minimising the electric field at the sample. In an EPR experiment, and a DNP experiment, the cavity must be coupled to the microwaves by matching the impedance of the cavity to the microwave-carrying waveguide.

Continuous-wave (CW)-EPR utilises phase-sensitive detection, where the magnetic field applied to the sample is modulated sinusoidally. The modulated EPR signal is then compared to a reference signal with the same frequency as the field modulation, so noise and other interference is suppressed and the experimental sensitivity improved. In contrast to NMR, EPR spectra are usually recorded and reported as the first derivative of the corresponding absorption spectrum.

2.3 Dynamic nuclear polarisation

Dynamic nuclear polarisation (DNP) is a technique that exploits the large gyromagnetic ratio of the electron by transferring the thermal polarisation of electron spins to nuclear spins to provide enhanced sensitivity to an NMR experiment. This transfer can proceed through various mechanisms depending on the experimental

conditions. For solids, DNP can occur via the Overhauser effect, the solid effect, thermal mixing, or the cross effect; for liquids, the Overhauser effect is the only known mechanism. An overview of the Overhauser effect in liquids is given in the following sections.

2.3.1 Electron-nuclear spin system

The Hamiltonian for a electron-nucleus coupled system in a magnetic field can be written as:

$$H = \omega_{\mathrm{S}} S_{\mathrm{z}} - \omega_{\mathrm{I}} I_{\mathrm{z}} + H_{\mathrm{SS}} + H_{\mathrm{SI}} + H_{\mathrm{II}} \tag{2.34}$$

The first two terms represent the electron and nuclear Zeeman interactions, respectively; whilst the third, fourth and fifth terms represent the spin-spin interactions between electrons, electrons and nuclei, and nuclei, respectively. The term of most interest for DNP is the hyperfine term H_{SI}, which can be considered in two separate parts: a scalar Fermi contact interaction part $H_{\mathrm{SI}}^{\mathrm{S}}$ (isotropic) and a dipolar interaction part $H_{\mathrm{SI}}^{\mathrm{D}}$ (anisotropic), given by [20, 30]:

$$H_{\mathrm{SI}}^{\mathrm{S}} = \sum_{i,j} a_{ij} \boldsymbol{I_i}.\boldsymbol{S_j} = \sum_{i,j} \frac{1}{2} a_{ij} (I_i^+ S_j^- + I_i^- S_j^+) + I_z^i S_z^j \tag{2.35}$$

$$H_{\mathrm{SI}}^{\mathrm{D}} = \sum_{i,j} \frac{\gamma_{\mathrm{S}} \gamma_{\mathrm{I}} \hbar}{r_{ij}^3} (A_{ij} + B_{ij} + C_{ij} + D_{ij} + E_{ij} + F_{ij}) \tag{2.36}$$

$$A_{ij} = (1 - 3\mathrm{cos}^2\theta_{ij}) I_z^i I_z^j \tag{2.37}$$

$$B_{ij} = -\frac{1}{4}(1 - 3\mathrm{cos}^2\theta_{ij})(I_i^+ S_j^- + I_i^- S_j^+) \tag{2.38}$$

$$C_{ij} = -\frac{3}{2}\mathrm{sin}\theta_{ij}\mathrm{cos}\theta_{ij}\mathrm{e}^{-i\varphi_{ij}}(I_z^i S_j^+ + I_i^+ S_z^j) \tag{2.39}$$

$$D_{ij} = -\frac{3}{2}\mathrm{sin}\theta_{ij}\mathrm{cos}\theta_{ij}\mathrm{e}^{i\varphi_{ij}}(I_z^i S_j^- + I_i^- S_z^j) \tag{2.40}$$

$$E_{ij} = -\frac{3}{4}\mathrm{sin}^2\theta_{ij}\mathrm{e}^{-2i\varphi_{ij}} I_i^+ S_j^+ \tag{2.41}$$

$$F_{ij} = -\frac{3}{4}\mathrm{sin}^2\theta_{ij}\mathrm{e}^{2i\varphi_{ij}} I_i^- S_j^- \tag{2.42}$$

where r_{ij}, θ_{ij} and φ_{ij} are the polar coordinates of the vector joining the nucleus i and electron j.

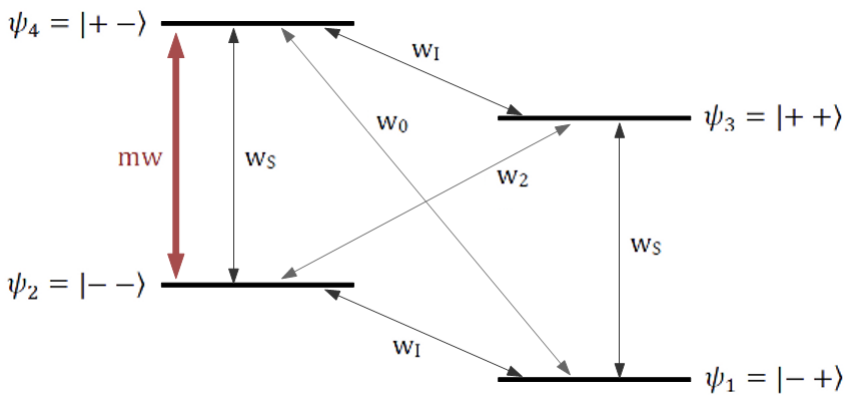

Figure 2.4: Energy level diagram for an electron spin $S = 1/2$ coupled to a nuclear spin $I = 1/2$. All possible transition probabilities are shown, where w_I is the nuclear spin relaxation rate, w_S is the electron spin relaxation rate, w_2 is the double-quantum relaxation rate, w_0 is the zero-quantum relaxation rate. The microwave excitation of an electron transition is also indicated.

2.3.2 The Overhauser effect

In the Overhauser effect, the polarisation transfer is not direct, rather it is achieved via relaxation processes. Initially, the allowed EPR transitions are saturated by microwave irradiation which equalises the populations. The system then undergoes spin-lattice relaxation which acts to generate a non-thermal equilibrium population of the energy levels that results in greater nuclear polarisation.

As mentioned in Section 2.1.5, spin-lattice relaxation processes involve loss of energy to the surrounding environment or lattice. This energy transfer requires energy $\approx \hbar\omega_\mathrm{S}$, and so modulation of the hyperfine term H_SI (Equation 2.34) is needed on a timescale $\approx 1/\omega_\mathrm{S}$ ($\sim$ 2 ps at 3.4 T). This modulation is generally considered to come from random molecular motion, as contributions from fluctuations due to electron relaxation ($\sim$ nanoseconds [31, 32]) are negligible [30].

Understanding of the Overhauser effect is most easily achieved by considering a simple system in which an electron spin $S = 1/2$ is coupled to a proton $I = 1/2$. The resulting four energy levels are shown in Figure 2.4, where w_i is the transition probability between a pair of levels.

The effect on the population of each level N_i of the various relaxation processes can be seen by evaluating the differential equations that account for all pos-

sible transitions. These can be written as [33]:

$$\frac{d}{dt}\begin{pmatrix} N_1 \\ N_2 \\ N_3 \\ N_4 \end{pmatrix} = \begin{pmatrix} -w_{\mathrm{A}} & w_{\mathrm{I}} & w_{\mathrm{S}} & w_0 \\ w_{\mathrm{I}} & -w_{\mathrm{B}} & w_2 & w_{\mathrm{S}} \\ w_{\mathrm{S}} & w_2 & -w_{\mathrm{B}} & w_{\mathrm{I}} \\ w_0 & w_{\mathrm{S}} & w_{\mathrm{I}} & -w_{\mathrm{A}} \end{pmatrix} \begin{pmatrix} N_1 - N_1^0 \\ N_2 - N_2^0 \\ N_3 - N_3^0 \\ N_4 - N_4^0 \end{pmatrix} \tag{2.43}$$

where N_i^0 are the thermal equilibrium Boltzmann populations, $w_{\mathrm{A}} = w_{\mathrm{I}} + w_{\mathrm{S}} + w_0$ and $w_{\mathrm{B}} = w_{\mathrm{I}} + w_{\mathrm{S}} + w_2$.

Solomon [34] derived a rate equation for the nuclear polarisation expectation value $\langle I_z \rangle$ of such a two-spin system:

$$\frac{d\langle I_z \rangle}{dt} = -(w_2 + 2w_{\mathrm{I}} + w_0 + w^0)(\langle I_z \rangle - I_0) - (w_2 - w_0)(\langle S_z \rangle - S_0) \tag{2.44}$$

where $\langle S_z \rangle$ is the expectation value of the electron polarisation; I_0 and S_0 are the thermal equilibrium values of $\langle I_z \rangle$ and $\langle S_z \rangle$, respectively; and w^0 represents the nuclear relaxation rate in the absence of a radical. Taking the steady state solution of Equation 2.44, i.e. $d\langle I_z \rangle / dt = 0$, multiplying the top and bottom by $S_0(w_2 + 2w_{\mathrm{I}} + w_0)$ and appropriate rearrangement gives:

$$\langle I_z \rangle = I_0 \left(1 + \frac{w_2 - w_0}{w_2 + 2w_{\mathrm{I}} + w_0} . \frac{w_2 + 2w_{\mathrm{I}} + w_0}{w_2 + 2w_{\mathrm{I}} + w_0 + w^0} . \frac{S_0 - \langle S_z \rangle}{S_0} . \frac{S_0}{I_0} \right) \tag{2.45}$$

At this point it is common to define the following parameters:

$$\rho = w_2 + 2w_{\mathrm{I}} + w_0; \quad \sigma = w_2 - w_0 \tag{2.46}$$

and

$$\xi = \frac{w_2 - w_0}{w_2 + 2w_{\mathrm{I}} + w_0} = \frac{\sigma}{\rho} \tag{2.47}$$

$$f = \frac{w_2 + 2w_{\mathrm{I}} + w_0}{w_2 + 2w_{\mathrm{I}} + w_0 + w^0} = \frac{\rho}{\rho + w^0} \tag{2.48}$$

$$s = \frac{S_0 - \langle S_z \rangle}{S_0} = \frac{\gamma_{\mathrm{S}}^2 B_1^2 T_{1\mathrm{S}} T_{2\mathrm{S}}}{1 + \gamma_{\mathrm{S}}^2 B_1^2 T_{1\mathrm{S}} T_{2\mathrm{S}}} \tag{2.49}$$

where σ is sometimes called the cross relaxation rate constant, and ξ, f and s are known as the coupling constant, leakage factor and saturation factor, respectively. Equation 2.45 can now be rewritten in the much more convenient form:

$$\langle I_z \rangle = I_0 \left(1 + \xi f s \frac{\gamma_{\mathrm{S}}}{\gamma_{\mathrm{I}}} \right) \tag{2.50}$$

This leads to defining the Overhauser DNP enhancement as [6]:

$$\varepsilon = \frac{\langle I_z \rangle - I_0}{I_0} = \xi f s \frac{\gamma_S}{\gamma_I} \tag{2.51}$$

The three parameters ξ, f and s of Equation 2.51, sometimes referred to as the Overhauser equation, can take a range of values with the maximum magnitude being 1. So the ratio of the gyromagnetic ratios γ_S/γ_I, which is a constant, is the maximum achievable enhancement in an Overhauser DNP experiment. Therefore, the three aforementioned variable parameters are of great interest since they are limiting factors of the DNP enhancement; each will now be considered in turn.

Leakage factor — f

The leakage factor accounts for the effect of electron spins on the nuclear relaxation, and can also be written:

$$f = 1 - \frac{T_{1I}}{T_{1I0}} \tag{2.52}$$

where T_{1I} and T_{1I0} are the nuclear spin-lattice relaxation times in the presence and absence of a radical, respectively. The value of f can range from 0 to 1, and can be measured relatively easily using standard NMR T_1 experiments on samples with and without the polarising agent. The value generally approaches, and is often assumed to be, 1 for radical concentrations of about 10–20 mM and higher [35].

Saturation factor — s

The saturation factor is a measure of the extent of electron spin saturation and varies from 0 to 1. In theory, it can be measured using EPR but is practically challenging due to short T_{2S} times (in the low ns range [36] [37]) at the common liquid DNP conditions of nitroxide radicals in high magnetic fields at room temperature. Achieving complete saturation often requires high microwave powers, which can lead to significant heating in cases where lossy solvents such as water are used.

If the radical EPR spectrum displays a single line, the DNP enhancement varies linearly with applied microwave power P_{mw} in the low power region ($\gamma_S^2 B_1^2 T_{1S} T_{2S} \ll 1$) where $s \ll 1$. Therefore, a plot of $1/\varepsilon$ as a function of $1/P_{mw}$ can be used to extrapolate to infinite power, complete saturation, and hence maximum enhancement. However, the situation is more complex for EPR spectra displaying hyperfine splitting, as is frequently the case since commonly used nitroxide radicals with ^{14}N and ^{15}N have three and two lines (separated by $\sim$ 50 MHz at 3.4 T), respectively. Predicting the saturation factor in this case is more complicated since

hyperfine lines not being directly pumped by microwave irradiation are still partially saturated due to electron spin exchange and nuclear relaxation processes. Whilst the presence of non-resonant EPR lines does not prevent high saturation as previously thought (see Section 3.5.2), it does make full saturation more difficult, typically requiring a combination of high microwave power and high radical concentration to approach $s = 1$.

Coupling factor — ξ

The coupling factor is dependent on the inherent physical properties of the electron-nuclear spin system and, in particular, is directly proportional to the difference between the double- and zero-quantum relaxation rates. It can take a range of values from -1 for pure dipolar relaxation and 0.5 for pure scalar relaxation. The variation of ξ with field is the primary cause for reduced Overhauser DNP enhancement at higher magnetic fields. Therefore, accurate modelling of this parameter is very important.

— Analytical approach

The expression for the coupling factor in Equation 2.47 can be split into scalar (s) and dipolar (d) contributions:

$$\xi = \frac{\sigma}{\rho} = \frac{\sigma_\mathrm{s} + \sigma_\mathrm{d}}{\rho_\mathrm{s} + \rho_\mathrm{d}} \tag{2.53}$$

A semi-classical approach can be evoked to derive the spectral densities of the molecular motions responsible for scalar and dipolar relaxation [34, 20, 6]:

$$\rho_\mathrm{s} = -\sigma_\mathrm{s} = \frac{a^2}{2} J_\mathrm{s}(\omega_\mathrm{I} - \omega_\mathrm{S}) + \beta J_\mathrm{s}(\omega_\mathrm{I}) \tag{2.54}$$

$$\rho_\mathrm{d} = \frac{\gamma_\mathrm{I}^2 \gamma_\mathrm{S}^2 h^2}{10 r_\mathrm{SI}^6} [6J_\mathrm{d}(\omega_\mathrm{I} + \omega_\mathrm{S}) + J_\mathrm{d}(\omega_\mathrm{I} - \omega_\mathrm{S}) + 3J_\mathrm{d}(\omega_\mathrm{I})] \tag{2.55}$$

$$\sigma_\mathrm{d} = \frac{\gamma_\mathrm{I}^2 \gamma_\mathrm{S}^2 h^2}{10 r_\mathrm{SI}^6} [6J_\mathrm{d}(\omega_\mathrm{I} + \omega_\mathrm{S}) - J_\mathrm{d}(\omega_\mathrm{I} - \omega_\mathrm{S})] \tag{2.56}$$

where the last term in Equation 2.54 is to account for fast electron relaxation which reduces the DNP effect, and β is a weighting factor that takes values from 0 to 1. The spectral density is characterised by a Lorentz function:

$$J(\omega) = \frac{\tau_\mathrm{c}}{1 + \omega^2 \tau_\mathrm{c}^2} \tag{2.57}$$

where τ_c is the correlation time. For the case of pure dipolar relaxation, the coupling factor becomes:

$$\xi_d = \frac{\sigma_d}{\rho_d} \approx \frac{5J_d(\omega_S)}{7J_d(\omega_S) + 3J_d(\omega_I)} \tag{2.58}$$

using the approximations $\omega_I \pm \omega_S \approx \omega_S$ since $\omega_I \ll \omega_S$. This model is based on rotational motion of the electron and nucleus. However, for nitroxides in water, it has been shown that the translational diffusion component dominates the modulation of the dipolar coupling [38], and so a Lorentzian spectral density function is no longer suitable. Various models for the spectral density have been proposed, but the most commonly used is based on a force-free hard-sphere (FFHS) model [39] where the spins are modelled as being in the centre of hard spheres undergoing diffusion without the influence of any other forces. The resulting spectral density function was found to be:

$$J_t(z) = \frac{8 + 5z + z^2}{81 + 81z + (81/2)z^2 + (27/2)z^3 + 4z^4 + z^5 + z^6/8} \tag{2.59}$$

where $z = \sqrt{2\omega\tau_t}$ and the correlation time is the translation diffusion time:

$$\tau_t = \frac{d^2}{D_S + D_I} \tag{2.60}$$

where D_S and D_I are the diffusion constants for the radical and solvent (or other target) molecules, and d is their distance of closest approach. Equations 2.57 and 2.59 have been used with Equation 2.58 to calculate the field dependence of the coupling factor for rotational and translational diffusion, which is shown in Figure 2.5. The dramatic fall in the coupling factor, and thus the DNP enhancement, at high fields is clear, with a somewhat flatter curve observed for translational diffusion models.

This model has frequently been used to describe the coupling factor, since it provides soluble analytical equations. However, it is not clear whether it is still sufficiently precise at higher magnetic fields where other types of motion may become important. It may be that the spectral densities in use at present need to be revised or replaced, which is currently an important open question in liquid DNP. It should come as no surprise that a model based on hard spheres with centralised spins, that does not reflect the physical reality, would likely breakdown eventually.

— Atomistic simulation approach

The use of atomistic molecular dynamics (MD) simulations, led by Sezer and coworkers [40], is a promising alternative approach for interpreting liquid DNP data

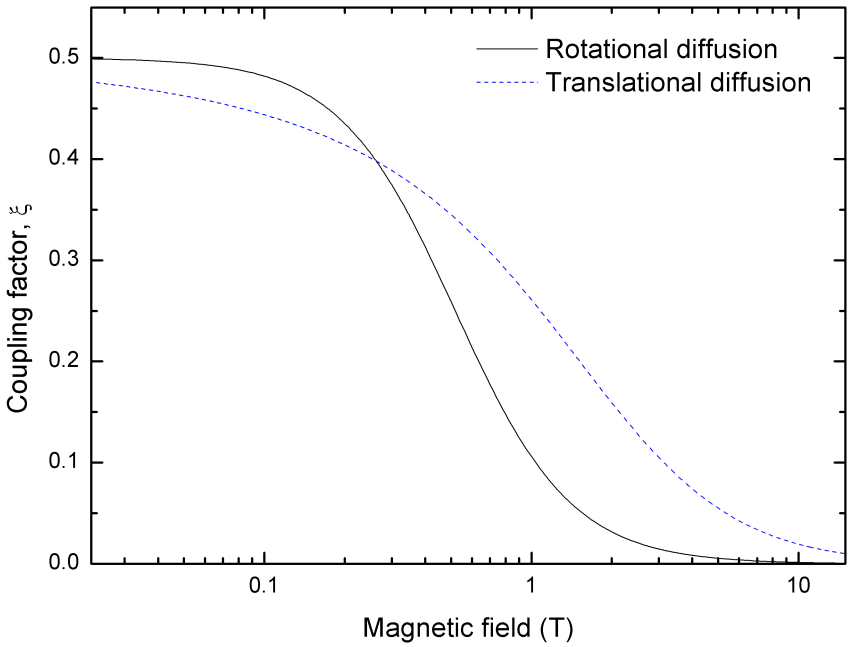

Figure 2.5: Calculated field dependence of coupling factor for pure dipolar relaxation, modeled with rotational (solid black line) and translational (dashed blue line) diffusion, using a correlation time $\tau = 20$ ps.

and calculating coupling factors. Such simulations allow the dynamics of the radical-solvent system to be probed to atomic detail, down to sub-picosecond timescales.

MD simulations have been applied to study the nitroxide radical TEMPOL in water [40]. A simulation box was filled with water molecules (1000 or 2991) and one radical molecule was used, and numerical integrations with 2 fs time steps were carried out. The model used for water is known to result in unrealistically fast dynamics, so this was corrected for by adjusting a friction coefficient in the simulation to match the simulated and experimentally determined diffusion constant.

Scalar and dipolar electron-nuclear interaction energies were calculated from first principles, for 5 different orientations of the water molecules relative to the radical. The simulations were then used to calculate the correlation functions:

$$C^{(m)}(\tau) = \overline{F^{(m)}(\boldsymbol{r}(t))F^{(m)*}(\boldsymbol{r}(t+\tau))} \tag{2.61}$$

where the superscript (m) denotes three different spatial directions, which were calculated separately but found to be equal to within the uncertainty of the calculations, indicating adequate sampling to reflect the isotropic nature of the molecular tumbling in solution.

The distribution of the electron density on the TEMPOL molecule is known to be almost equal between the nearby nitrogen and oxygen nuclei, though this does vary with factors such as solvent polarity [41]. Therefore, for the calculations the simplification of 50% at the nitrogen and 50% at the oxygen of the N-O group was made. So when calculating correlation functions (Equation 2.61), two contributions to the dipolar function had to be considered:

$$F^{(m)}(\boldsymbol{r}) = \frac{1}{2}[F^{(m)}(\boldsymbol{r}_{\mathrm{Op}}) + F^{(m)}(\boldsymbol{r}_{\mathrm{Np}})] \tag{2.62}$$

where $\boldsymbol{r}_{\mathrm{Op}}$ and $\boldsymbol{r}_{\mathrm{Np}}$ are the oxygen-proton and nitrogen-proton distance vectors, respectively.

The dipolar correlation functions $C^{(m)}(\tau)$ were fit arbitrarily to the function:

$$a_1 e^{-\tau/\tau_1} + a_2 e^{-\tau/\tau_2} + (1 - a_1 - a_2) e^{-\tau/\tau_3} \tag{2.63}$$

where the a_i and τ_i are amplitudes and timescales used to fit the correlation functions. The molecular motion of the water and TEMPOL molecules was found to occur on three distinct time scales of approximately 0.4, 4 and 30 ps.

Spectral density functions were calculated from these correlation functions for the dipolar interaction. A spectral density for scalar coupling was also calculated and found to have a negligible (<2%) contribution to the coupling factor compared to dipolar coupling, as expected.

Coupling factors were calculated and found to agree well with other values in the literature (see Section 3.5.1). In addition, ξ values were calculated for the electron on the oxygen ($\xi = 0.0918$) and nitrogen ($\xi = 0.0257$) only, finding an almost 4-fold decrease in the coupling factor at 94 GHz when moving the electron from the outer sphere of the radical molecule (O) to a position closer to the centre (N). This shows the importance of the distance of closest approach (since dipolar interaction $\propto 1/r^6$), and rationalises the relative ineffectiveness for Overhauser DNP of larger radicals such as trityl (see Section 3.4).

The MD simulations were also found to provide good agreement of calculated diffusion constants compared with experiment for TEMPONE [38], demonstrating the feasibility of using MD to calculate distances of closest approach via the FFHS model. However, the authors noted that this 'distance' cannot really be the physical distance between unpaired electron and solvent nucleus, and is really more of an 'effective distance'. The FFHS model allows solvent molecules to approach the electron spin from all directions and up to the same distance. Most real molecules, however, including TEMPOL, lack this kind of spherical symmetry.

Finally, the simulations were used to examine the hydrogen bonding between the water and radical molecules, and also the lifetimes of those bonds. The authors suggest that the three distinct timescales that were observed in fitting the correlation functions may correspond to different "modes of motion": short lifetime, where bonds rapidly decay due to thermal librational movements of the water (∼0.4 ps); intermediate lifetime, where hydrogen bonds are formed and broken (∼4 ps); and long lifetime motions, which is the translational diffusion of water (∼30 ps). Analytical approaches such as the FFHS model cannot describe the first two of these processes, and do not seem to provide the same depth of insight as MD simulations, which have been demonstrated to provide good estimates of ξ over a wide range of field strengths.

Sezer has very recently suggested a further improvement to this computational method [42], where he suggested the previous approach does not utilise sufficiently large simulation boxes to fully sample the rapidly diffusing water molecules. In his most recent paper, he has shown that a synergy of the analytical and computational approaches is a feasible method for describing liquid DNP experiments [43]. This promising methodology utilises MD to describe short range interactions (near the centre of the polarising agent) and a modified FFHS model to describe the long range interactions, whilst ensuring a matching of the two in the intermediate region.

Chapter 3

Review of dynamic nuclear polarisation experiments

The wide-ranging applicability of dynamic nuclear polarisation to numerous areas of scientific research has led to the publication of large volumes of work in many disciplines, as illustrated by the recent special issues of the journals Physical Chemistry Chemical Physics [44] and Applied Magnetic Resonance [45]. Reviewing the entire field would be an incredibly difficult undertaking and not particularly instructive in providing background for the work presented in this thesis. Therefore, only microwave-driven DNP will be considered. Some work in solid-state DNP will be briefly reviewed to provide historical context, but the focus of this chapter will be on solution-state studies of the Overhauser effect (OE).

Other areas of active research within the broad umbrella term of 'DNP', but beyond the scope of this review, include: chemically-induced dynamic nuclear polarisation (CIDNP), parahydrogen-induced polarisation (PHIP) and optical pumping. The interested reader is referred to References: [46], [47], [48] and [49] for early work and more recent reviews of CIDNP; [50], [51] and [52] for reviews of PHIP; and [53], [54], [55] and [56] for work in the area of optical pumping.

3.1 Discovery and early investigations of the Overhauser effect

The birth of DNP can be traced back to Albert W. Overhauser, who presented his theory in May 1953 at a meeting of the American Physical Society [57]. His idea was originally met with considerable scepticism by many prominent figures in the magnetic resonance community including Felix Bloch, Edward Purcell, Isidor

Rabi, Norman Ramsey, Nicolaas Bloembergen and Anatole Abragam [58]. However, experimental confirmation of what came to be known as the 'Overhauser effect' was provided by Carver and Slichter [3] three months later, before Overhauser's paper was even published. An interesting and personal review of the early efforts in DNP by one its pioneers can be found in Reference [58].

DNP had its beginnings in solids, specifically metals, where the Overhauser effect was originally predicted and subsequently demonstrated by the observation of an enhanced ^{7}Li resonance. Shortly after, it was suggested that the OE might also be observable in non-metals, which was confirmed by Beljers et al. [59] when they observed the proton resonance of the free radical DPPH (2,2-diphenyl-1-picrylhydrazyl).

It was soon realised that similar experiments to those carried out in metals and paramagnetically doped solids could be conducted in liquids. The first solution-state DNP experiments were reported by Carver and Slichter in 1956 [4], followed by Bennett and Torrey the next year [60] who for the first time observed large negative enhancements of solvent protons (in a solution of sodium and naphthalene in 1,2-dimethoxyethane), which they termed an "inverted Overhauser effect".

During the 1960s, through to the early 1980s, the OE in liquids was a topic of intense research. In particular the groups of Hausser, Müller-Warmuth and Richards made significant contributions to the field. By the late 1960s, in addition to ^{1}H nuclei, liquid DNP was also used to observe ^{13}C [61], ^{19}F [62] and ^{31}P [63] nuclei.

The frequency dependence of this DNP effect was investigated using standard organic radicals, such as DPPH and BPA (bisphenol A), in solutions. Perhaps one of the most important conclusions of these early experiments was that the sign of the coupling factor is dependent on the rotational and translational motion between the radical and solvent molecules, and that modulation of the scalar hyperfine interaction results in positive enhancement whilst modulation of the dipolar interaction gives a negative enhancement (Bennett's "inverted Overhauser effect"). In 1983, Müller-Warmuth and Meise-Gresch conducted experiments on various nuclei using different radicals and found the behaviour of the coupling factor to be somewhat more complicated than that of theoretical curves for scalar and dipolar relaxation [64]. They suggested that contributions from both were usually at play and that the proportions were dependent on the details of the experiments, i.e. the nuclei, solvent and polarising agent chosen. The effect of having a mixture of these two processes (scalar and dipolar) can lead to reducing the effective enhancement or cancelling it out all together. Since the relaxation mechanism is not usually known, quantitative predictions can be challenging. However, they also found that for protons in solution, the dipolar relaxation mechanism is almost always dominant (with

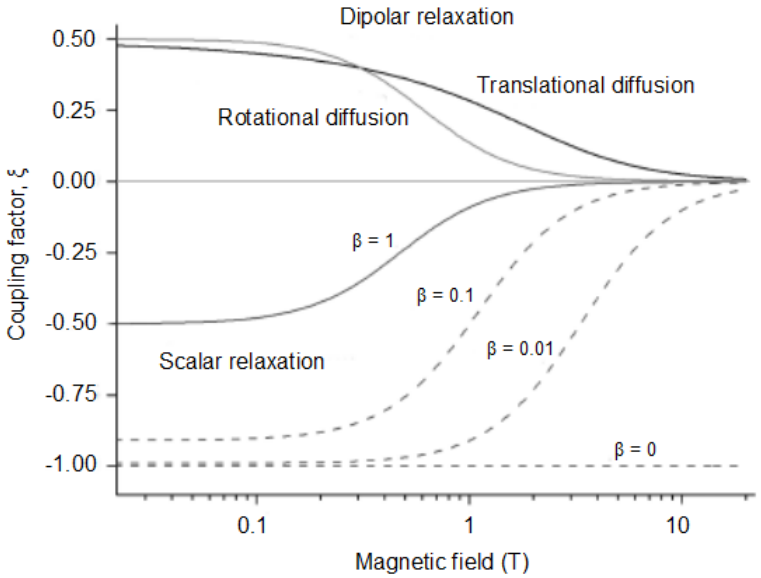

Figure 3.1: Theoretical field dependence of coupling factors, calculated using a 20 ps correlation time (from Reference [33]). Top 2 lines — pure dipolar relaxation mechanism, modelled with rotational and translational diffusion; bottom 4 lines — pure scalar relaxation mechanism, shown for various values of the fast electron spin relaxation correction term β.

the exceptions observed being aromatic protons and the protons of trifluroacetic acid). This is the case for all work presented in this thesis, so dipolar relaxation leading to negative enhancement can be safely assumed.

The other major result of these first studies of the OE was the theoretically predicted curves for the frequency dependence of the coupling factor (see Figure 3.1), still a topic of great interest today. First expounded by Hausser in 1965 [5], he predicted a rapid decrease at high fields, approaching values close to zero at the commonly used magnetic field strengths in today's high-resolution NMR. The reported results available seemed to agree well with this theory, with an observed decrease in the efficiency of this DNP effect with increasing magnetic field. However, measurements were only made up to 1.3 T [65], owing to the technological limits of the time. These results seemed to show that Overhauser DNP in liquids would be an extremely inefficient process at high magnetic fields and, therefore, likely an unfruitful endeavour.

3.2 Solid-state mechanisms and DNP at high magnetic field strengths

Perhaps due in part to the discouraging predictions for the usefulness of the OE at high fields, throughout most of the 1980s and 1990s, the focus of DNP research was largely on the solid-state and mechanisms such as the solid effect [66, 67], thermal mixing [68, 69], and the cross effect [70, 71, 72, 73, 74, 75]. Excellent reviews of this earlier work in solid-state DNP can be found in References [24], [76] and [30].

During the late 1970s and the 1980s the development of DNP was hindered by a lack of suitable high frequency microwave sources, until Griffin and co-workers pushed the field forward when they developed novel high power gyrotron microwave sources operating at 140 GHz [77, 9, 78] and 250 GHz [79]. Over the last two decades, they have been at the forefront of the continued drive of gyrotron technology to higher and higher limits with the current highest frequency (applied to DNP) reported, at the time of writing, being 460 GHz (700 MHz ^{1}H NMR frequency) [80].

The evolution of the gyrotron has undoubtedly revitalised the field of DNP and its use in solid-state studies has shown great potential in the last decade or so where numerous studies of biomolecules [81, 82, 83, 84, 85, 86], as well as other solids [87, 88] have been reported at high fields.

3.3 Feasibility of high-field liquid DNP

The prediction of a very small coupling factor at high fields for the OE led to a period of relative inactivity in this area of research. However, several key results after the turn of the century — in particular the work of the Griffin group [10] and Ardenkjaer-Larsen [89] — brought about a new era of optimism and extensive research for liquid DNP.

As more and more research groups began to turn their attention to DNP in liquids, several different methodologies developed; these can be broadly divided into two groups: in-situ and sample transfer (ex-situ) methods.

3.3.1 Direct polarisation in-situ

In this type of DNP, commonly referred to as simply (high-field) liquid DNP, the polarisation and detection phases of the experiment are conducted at the same magnetic field in the liquid state. This is the type of experimental setup (see Chapter 4) used for the work presented throughout this thesis and will, therefore, be the focus of this chapter.

It was with this technique that, in 2002, Loening et al. [10] provided solution-state DNP with its first boost by utilising a gyrotron to successfully carry out Overhauser DNP experiments at room temperature at 5 T (140 GHz microwave frequency). They studied ^{31}P, ^{13}C, ^{15}N and ^{19}F dissolved in deuterated benzene with the radical BDPA (bisdiphenylene-β-phenylallyl), achieving enhancements in the range $\sim$10–100. These results showed the feasibility of using the DNP technique in liquids at high fields; something which had long been thought of as unpractical.

By polarising the sample in-situ, the experimental complications of shuttling the sample need not be addressed and also (in the case of dissolution) the potentially sample damaging freeze-thaw process can be avoided. It does, of course, come with its own challenges. For example, in order to reach the kinds of magnetic field strengths common in modern-day NMR, very high frequency microwave sources are required, e.g. a 9.2 T magnetic field corresponds to a 400 MHz/260 GHz Larmor frequency for protons/electrons. Numerous technological advances have provided solutions to this, amongst them gyrotrons [9, 90, 91, 12, 80] and extended interaction klystron (EIK) amplifiers [92, 43], which have been used to great success in DNP of liquids as well as solids.

Concurrently, as higher frequency microwaves are required as the field strength (and frequency) increases, the possible sample size decreases, scaling with $\sim 1/f^3$ [93]. This has necessitated the development of double resonance structures for NMR and EPR of increasingly small scale. A review of the development of high-field EPR instrumentation often used for DNP experiments is given by Smith et al. [94]. Significant strides in resonator development have been made by the Prisner group in particular who, for example, recently combined a Fabry-Perot resonator (FPR) with a stripline NMR resonance structure to improve the usually poor NMR performance and also increase sample size by a factor of 30 (since FPRs do not have the same constraints as the single-mode cavities often used). The disadvantage of such a system, compared to one with say a cylindrical cavity as used here (see Chapter 4), is that much higher microwave power is required to compensate for the lower microwave conversion factor. Given the sample volume limitations, when designing a high-field DNP experiment and choosing a sample to study, it is especially important to consider the potential magnitude of the enhancement and whether it might be large enough to be worthwhile if the volume of available sample is not already limited. On the other hand, for applications where the amount of the sample under study is limited even relatively modest enhancements would be welcomed.

Over the last few years, a significant body of work has been published at 3.4 T. Substantial enhancements have been reported in water protons for example.

In 2010, Türke et al. [95] reported significant enhancements of water protons using the TEMPONE-D, ^{15}N radical at a concentration of 25 mM. With acquisition occurring after 1 s of microwave irradiation, they observed a maximum enhancement of $\varepsilon = -43$. Their experimental setup allowed them to measure B_{1S} at the sample as well as T_{1S} and T_{2S}, leading them to calculate almost complete saturation of the two hyperfine lines, i.e. $s = 0.98$. However, an aspect omitted from their analysis was the temperature at which this enhancement occurred. They were not able to use any kind of external temperature sensor due to the small sample size, and did not have sufficient resolution to use the water proton chemical shift as an internal temperature reference. They estimated an $\sim$15 K temperature rise from the change in the cavity quality factor, but admitted the likelihood of large errors.

In the same issue of Physical Chemistry Chemical Physics, Villanueva-Garibay et al. [96] reported similar measurements of Overhauser DNP of water protons using 10 mM TEMPO. Using an efficient, novel double-resonance structure — consisting of a non-radiative microwave cavity combined with an r.f. coil inside the dielectric part of the resonator — they bettered previously measured enhancements, reaching a maximum of $\varepsilon = -65$. Like other DNP experiments on the very lossy water solvent, heating was unavoidable. Unfortunately, a lack of sufficient B_0 field homogeneity again prevented the use of water proton shifts to measure sample temperature. Another problem they encountered, common with liquid DNP at these high fields is that due to the small resonator size, the NMR active sample volume was larger than the DNP-enhanced sample volume. They attempted to compensate for this by calculating the proportion of sample contributing towards the DNP enhancement, from calculations of the cavity microwave field profile. Using this correction, they stated a maximum enhancement at the centre of the cavity of $\varepsilon = -94$. It should be noted that no signal averaging was used as they experienced problems with movement of the sample droplet inside the capillary as heating occurred. They also observed an almost linear increase of ε at their highest microwave powers (up to 140 mW), as opposed to a plateau associated with full saturation. They reasoned that this may be an effect of heating, reducing the translational correlation time and increasing the enhancement [97, 38], but again the absence of accurate temperature measurements for their data precluded further quantitative analysis.

In Chapter 5 of this thesis, these temperature issues are addressed by utilising the chemical shift of water protons. In addition, enhancements greater than those reported by Villanueva-Garibay et al. [96] are presented.

Results at the higher field of 9.2 T are also demonstrating the promising future of high-field DNP in liquids with reported enhancements of $\varepsilon \approx -29$ for water

protons [12]. In addition, the first reports are beginning to appear of DNP enhancements of nuclei on solute as well as solvent molecules. In a study of metabolites at 9.2 T, Krummenacker et al. [98] showed that whilst polarisation transfer from solvent protons to other dissolved molecule protons seems plausible, it does not appear to happen. Polarisation is transferred directly from the electron on the free radical to the target molecule proton. Similar results, showing the DNP enhancement of small organic compounds in solution at 3.4 T are presented in Chapter 6 of this thesis.

3.3.2 Sample transfer

These experiments take advantage of the higher achievable polarisations and greater sample volumes (due to larger resonators) at low fields, before transferring the sample to a higher magnetic field for higher resolution detection of the DNP-enhanced NMR signal. The principle disadvantage of these methods (besides their technically challenging nature) is the loss of polarisation during sample transfer, as well as the lower maximum obtainable enhancement determined by the ratio of the two fields.

Dissolution method

In 2003, the work of Ardenkjaer-Larsen and co-workers sparked great interest in DNP when they proposed the novel dissolution DNP experiment [89]: the sample was frozen and cooled to 1.2 K where polarisation in the solid-state was accomplished at 3.35 T (94 GHz), and then rapidly dissolved in hot solvent and transferred to a 9.4 T NMR magnet where the signal was detected. Using this new method, they reported massive enhancements of 44,400 and 23,500 for ^{13}C and ^{15}N, respectively, in an aqueous solution of ^{13}C-urea. It should be noted, however, that these enhancements are relative to a thermal equilibrium signal at 9.4 T at room temperature and that much of the enhancement comes from the different Boltzmann distributions at temperatures differing by $\sim$300 K. Also, whilst this method allows greatly enhanced DNP-NMR spectra to be recorded in the liquid-state, the polarisation mechanisms at work are based on the solid-state, i.e. solid-effect, thermal mixing or cross effect. Nevertheless, this landmark publication was instrumental in reviving DNP research in both liquids and solids.

Whilst the advantages of dissolution DNP are clear, namely the incredible enhancements that can be achieved, the polarisation stage typically takes several hours and the method is not repeatable, allowing only a single measurement. Therefore signal averaging and conventional multidimensional NMR experiments are not

possible. However, 2D spectra have been successfully acquired using spatially encoded ultrafast NMR [99]. The potential of this dissolution technique has garnered much attention in the medical field, with applications including imaging and cancer research [100, 101, 102].

Leggett et al. [103] recently demonstrated a new strategy to deal with polarisation loss during sample transfer: they constructed a spectrometer for dissolution-DNP using a magnet with two isocentres — 3.35 T and 9.4 T. The short distance between these two isocentres (85 cm) allows transfer of the sample in the solid-state with little polarisation loss. In addition to giving greater enhancements than comparable experiments using two separate magnets, this method also allows the study of samples with shorter T_1 times.

The dissolution method has opened up DNP to many new applications and played a major part in rejuvenating the field (with Ardenkjaer-Larsen's 2003 paper being cited > 500 times at the time of writing) and much progress has been made in challenging areas such as 2D spectroscopy [99, 104]. However, there are samples (e.g. some proteins) which will likely never be suitable for study via this method due to the stresses imposed by the freezing and dissolving process. Here is where direct in-situ polarisation has its strengths as biomolecules can be studied under more biologically relevant conditions.

Shuttle method

The concept of shuttling samples between two different magnetic fields dates back to the early 1950s, when Purcell and Pound [105] conducted NMR experiments at 10 mT and 0.6 T on crystal LiF. This idea was later applied to CIDNP [106], and has since been successfully utilised in solution-state DNP [107, 108].

For further information about shuttle-DNP the interested reader is directed to extensive solution-state DNP reviews, which cover the topic in more detail, by Griesinger et al. [36], Bennati et al. [33] and Lingwood and Han [37].

3.4 Polarising agents

In general, polarising agents can be either exogenous (e.g. radical or metal ion added to sample) or endogenous (e.g. a protein with a naturally occurring radical [109]). However, the vast majority of examples in high-field DNP are of exogenous radicals, and to the author's knowledge, no examples of endogenous radicals have been reported in high-field liquid DNP.

Whilst initially radicals such as DPPH and BPA were in common use for liquids [6], as the field developed and applications to biological studies became a major goal two types of radical have dominated the literature: nitroxide radicals and triarylmethyl-based (TAM) radicals. Both display good stability and high water solubility, in addition to sufficiently narrow EPR lines.

In 1995, Grucker et al. [110] carried out an extensive investigation of the DNP performance of eighteen different nitroxide radicals in biological fluids. They found that nitroxides with shorter side chains (smaller molecule size) gave the greatest enhancements, and also noted that $^{2}H/^{15}N$ labelling improves saturation by narrowing/reducing the number of EPR lines. The findings of Armstrong and Han [111] in 2007 confirmed this at 0.35 T. They conducted similar experiments with ^{14}N- and ^{15}N-labelled 4-oxo-TEMPO over a range of concentrations (0.5–15 mM) and found the ^{15}N-labelled radical to give larger DNP enhancements, e.g. $\varepsilon \approx -46$ compared with $\varepsilon \approx -32$ for water protons with 15 mM radical concentration. The superior performance of ^{15}N- and ^{2}H-labelled radicals at 0.34 T was again confirmed by Höfer et al. [13], who in addition found that there was no difference between using TEMPO derivatives with either hydroxy or oxo groups.

In 1999, Wind et al. [112] demonstrated an appreciable enhancement using a TAM radical (also known as trityl) at 1.4 T. They suggested that in addition to the stability and high water solubility properties of the commonly used nitroxide radicals, trityl also has a single narrow EPR line (improving saturation) and gives much larger enhancements than nitroxides at low fields (e.g. -280 at 9.5 mT compared to -36 at 6.7 mT [110]). However, despite having three hyperfine lines which can be difficult to fully saturate, TEMPOL has been compared to trityl at 0.34 T and 3.3 T and found to consistently perform better [113]. This has been attributed to its smaller molecular size and therefore faster correlation time.

In the last few years, Fremy's Salt has emerged as a possible alternative to nitroxides at high fields, where it has much narrower EPR lines and is therefore easier to saturate [97]. ^{15}N-Fremy's Salt has been compared to ^{15}N-TEMPOL in liquid DNP experiments at 9.2 T and found to give larger enhancements. The coupling factor was found to be similar for the two radicals, so the dominating factor contributing to this improved DNP efficiency was thought to be better saturation. It was predicted that at high microwave powers, the enhancements of the two radicals would be similar. Further investigation of Fremy's Salt was conducted by Türke et al. [114], when they compared ^{15}N-Fremy's Salt with TEMPONE-D, ^{15}N at 0.35 T. At this relatively low field (frequency) full saturation is readily achievable, and at maximum saturation TEMPONE-D, ^{15}N was found to give the greater

enhancements at lower concentrations (5 mM and 10 mM), but their performance was similar at 25 mM. These initial studies seem to support the idea that Fremy's Salt may be an advantageous polariser at high fields when microwave power is limited and full saturation not feasible, or where the sample is particularly sensitive to heating effects.

A further avenue of investigation when designing polarising agents has been biradicals. Having been used with tremendous success in the solid-state [85, 115, 116], Gafurov et al. [117] attempted to use the biradical bTbK (bis-TEMPO-bis-Ketal) in liquid DNP experiments at 9.2 T. It was found to give no advantages over monoradicals, which they attributed to fast tumbling in solution impeding the energy matching conditions necessary for the cross effect DNP mechanism. They suggested that the cross effect might be possible if the radical tumbling could be reduced by either increasing their size or by attaching them to larger molecules. Thus far, no successful demonstrations of this have been reported.

Overall, TEMPO and its derivatives are still the most popular polarising agents for liquid DNP, especially at the more common field strength of 3.4 T. ^{15}N- and ^{2}H-labelled radicals are preferable, though they are typically quite costly compared to the cheap and readily available non-isotopically-enriched radicals. Furthermore, the benefit of using such polarisers depends on the concentration used and power available, which if sufficiently high can allow saturation approaching the maximum value anyway. Throughout most of the work presented in the chapters that follow, ^{14}N-TEMPOL was used, with a more expensive ^{15}N-enriched TEMPO derivative utilised in a saturation study in Chapter 7.

3.5 Overhauser equation parameters

There are three parameters (see Section 2.3.2) which can reduce the Overhauser DNP enhancement from the theoretical maximum of $\gamma_S/\gamma_I = 658$ or 329 (for protons with pure scalar or dipolar coupling to electron spin): the leakage factor f, the saturation factor s and the coupling factor ξ. If these parameters are known, then the maximum achievable enhancement can be predicted. Of these three, the leakage factor has always been the simplest to measure as it is dependent only on the relaxation time of the sample with and without the radical. Furthermore, in the ($\sim$mM) radical concentrations frequently used in DNP experiments, f often tends to 1. Obtaining independent measurements of the coupling and saturation factors, on the other hand, has proven much more complicated. This has been the focus of much of the research in high-field liquid DNP, in particular using ^{1}H DNP-NMR in aqueous

solutions where the dipolar mechanism dominates [118, 64] and the competing effects of scalar relaxation do not have to be considered.

3.5.1 Coupling factors at high frequency

The decreasing coupling factor with increasing field strength is the primary cause for lower Overhauser DNP efficiency at higher fields, so understanding and quantifying it has become particularly important as common NMR field strengths are at the level where the OE should no longer be very efficient. In addition, the coupling factor can provide useful information about the molecular motion of the radical-solvent system since it is dependent on the intermolecular distance and diffusion.

Previously, the models used for the molecular dynamics (based on translational or rotational diffusion) gave results that fit the available experimental data well. However, this was at low fields. Since liquid DNP research has undergone a shift into the high-field regime, reports at 3.4 T and 9.2 T have given enhancements greater than expected [113, 97, 43]. These encouragingly high results have led many to suggest that the models currently in use need to be improved or replaced.

In order to improve our understanding of the dynamics involved in liquid DNP, and the models used to describe them, accurate ξ values must be measured experimentally. This has proved somewhat challenging. Extracting ξ from DNP enhancements is possible, but f and s must also be known (γ_S/γ_I is a constant). As mentioned above, obtaining f is simple, but accessing s can be more complicated. If the polariser chosen has only a single EPR line [119], then full saturation is more readily achieved and $s \approx 1$ is possible. However, as discussed in Section 3.4, nitroxide radicals are most commonly employed as polarising agents (as is the case here) and TEMPO derivatives display either two or three hyperfine lines. This makes determining s, or maximising it, more difficult. A fuller discussion of the saturation factor will be given in the next section.

An alternative strategy to determine ξ, without the need for s, was first proposed by Hausser and Stehlik [6] and applied to the trityl radical by Ardenkjaer-Larsen et al. [120], where the field dependence of the nuclear relaxation rate was measured. In 2008, similar nuclear magnetic relaxation dispersion (NMRD) measurements were made for TEMPOL in water [113], where the proton longitudinal relaxation rate ($1/T_1$) was measured as a function of the applied magnetic field. The data acquired were fitted to a model for pure dipolar relaxation, which gave a value for the correlation time of the dipolar interaction of 15-20 ps. From this, coupling factors of $\xi = 0.36 \pm 0.02$ and $\xi = 0.06 \pm 0.02$ were calculated for fields of 0.35 T and 3.4 T.

Bennati et al. [121] also applied this NMRD method to find a value for the coupling factor of ^{15}N-^{2}H-TEMPONE in water at 0.35 T of $\xi = 0.35 \pm 0.02$ at 25°C. This was found to be in good agreement with the value calculated from DNP experiments of $\xi \leq 0.34$ at 27°C measured by Türke et al. [95]. However, Armstrong and Han previously found a value of $\xi \approx 0.22$ for the same system at the same field [111, 38]. They calculated this from DNP measurements they made as a function of radical concentration and applied microwave power, which were then extrapolated to infinity.

Another method for calculating coupling factors was proposed by Sezer et al. in 2009 [40]. They utilised molecular dynamics (MD) simulations to calculate correlation functions corresponding to the coupling of the unpaired electron on TEMPOL to water protons. They argued that high-field DNP in liquids should be dependent on the relative motion of solvent and radical molecules on an atomic scale. Therefore, the classical models usually used such as the force-free hard-sphere (FFHS) model (which assumes spins to be in the centre of spherical molecules subject to translational diffusion) are unrealistic and not fully suited to this application. From their results, they were able to calculate spectral densities and ultimately coupling factors at various fields and temperatures. For 0.35 T, they calculated $\xi = 0.30$ at 25°C; which is slightly below, but close to the NMRD values determined by Bennati et al. [121]. Values of ξ were also calculated for 3.4 T, which are in good agreement with results at room temperature presented in this thesis — this will be discussed further in Chapter 5.

Clearly there is a discrepancy between the various reported coupling factors. Up until now, despite the development of more physical models (e.g. which allow spins in non-central positions), the FFHS model has been favoured for its simplicity — it provides an uncomplicated analytical formula for dipolar spectral densities. However, whilst there have been many reports of successful high-field liquid DNP experiments with significant enhancements, recent experiments show that the models used to quantify the results are not sufficiently robust and require improvement.

To this end, Sezer very recently proposed a new 'multi-resolution' strategy for calculating coupling factors [42]. Building on his previous work [40], he combined MD simulations with a modified FFHS model to treat the interactions in two distance regimes. He suggested that his previously reported MD calculations were flawed in dealing with small solvent molecules such as water. In that system, consisting of TEMPOL dissolved in water, the solvent molecules undergo fast diffusion; moving approximately 3.5 nm in 1 ns. He noted that these length scales of molecular motion were similar to the size of simulation boxes applied, placing 'unrealistic

demands' on the calculation. As suggested elsewhere in the literature [122], whilst at short distances the shape of the molecules and the specifics of their interaction with one another are important, at greater distances the dynamics of small solvents (e.g. water and toluene) should depend almost entirely on their size and diffusion constant and not their detailed structure. Hence, MD simulations can be used to treat solvent molecules close to the radical and the FFHS model (with its simple analytical formulae) can be applied to the solvent molecules at long range. In the short range (close to the radical), solvent molecule trajectories are treated using MD up to a finite limit, which is accounted for explicitly in Sezer's calculations. By fitting the long range analytical expressions of the modified FFHS model to spectral densities calculated from MD, he was able to match the trajectories of solvent molecules in the intermediate distance range, thereby 'seamlessly sewing' the two methods together.

This approach was applied to TEMPOL in toluene and compared with existing data in the literature published by the Warwick group [43]. This system has the advantage of displaying two well-resolved proton resonances at this field — ring and methyl protons — which can be compared with each other. This allows the uncertain saturation factor to be eliminated from the analysis (see Section 3.5.2). The calculated ratio of the coupling factors for the ring and methyl protons $\xi_{\mathrm{ring}}/\xi_{\mathrm{methyl}}$ was found to agree within 7% of the experimental value.

These early results from this novel method seem to be encouraging; however, further testing across different magnetic field strengths is required (reported to be underway). Furthermore, application of this (or a similar) method more generally would be demanding computationally when studying large biomolecules for example. How easily these challenges can be overcome remains to be seen.

The above review shows that no consensus has yet been reached on how best to calculate coupling factors, and that some uncertainty still remains over some analyses carried out to date. This thesis (Chapters 5 and 6) provides more data to this particular field of research, with coupling factors for the TEMPOL-water system obtained at 3.4 T. The study has also been extended to include small organic compounds, reporting coupling factors for solute molecules for the first time at this magnetic field.

3.5.2 Saturation factor

The importance of the saturation factor is evident from the discussion of the previous section: if coupling factors are to be extracted from DNP enhancements, s must be determined. Furthermore, increasing saturation to its maximum value of $s = 1$

improves sensitivity. However, this situation is more complicated for radicals such as TEMPO because the EPR spectrum typically displays several (two or three) hyperfine lines as a result of strong hyperfine coupling of the unpaired electron with the nearby nitrogen nucleus (^{15}N or ^{14}N). Therefore, only partial saturation of non-resonant lines can be achieved, though this improves as the radical concentration is increased.

It was initially assumed that saturation of one resonance of a hyperfine-split EPR spectrum would leave the populations of the other levels unaffected [20], resulting in a saturation factor of $s = 1/3$ or $s = 1/2$ for nitroxides with ^{14}N and ^{15}N, respectively. This assumption has been made as recently as 1994 when TEMPOL was used in a study of proton-electron double-resonance imaging (PEDRI) [123]. However, since the 1970s it has been realised that this is far too pessimistic a view of electron spin saturation.

In 1977, Bates and Drozdoski [124] developed a mathematical model based on Heisenberg spin exchange which allowed the electron spins of two nitrogen nuclei in different spin states to be exchanged. This was compared with experiments of the radical HPNO (4-hydroxy-2,2,6,6-tetramethyl piperid-1-yloxy) in benzene, and found to be in good agreement. Little work was done in this area and saturation factors for nitroxide radicals were consistently underestimated until Armstrong and Han [111] improved the spin exchange-based model that had been proposed 30 years earlier. They presented a new model which, in addition to spin exchange, incorporated intramolecular nitrogen spin relaxation by explicitly accounting for the populations of the 12 energy levels in the proton-electron-nitrogen system. With this treatment, they derived equations for the maximum saturation in nitroxide radicals with ^{14}N (Equation 3.1) and ^{15}N (Equation 3.2) which are dependent on the intrinsic electron relaxation rate p (neglecting dipolar contributions from solvent protons and intermolecular dipolar interactions of electrons), the nitrogen relaxation rate w_{N} and the (concentration dependent) electron exchange rate κ:

$$s_{\max} = \frac{1}{3}\left(\frac{(2 + w_{\mathrm{N}}/p + 6\kappa/p)(2 + 3w_{\mathrm{N}}/p + 6\kappa/p)}{4 + (w_{\mathrm{N}}/p + 2\kappa/p)(w_{\mathrm{N}}/p + 6\kappa/p) + 2(3w_{\mathrm{N}}/p + 8\kappa/p)}\right) \tag{3.1}$$

$$s_{\max} = \frac{1}{2}\left(\frac{1 + w_{\mathrm{N}}/p + 2\kappa/p}{1 + w_{\mathrm{N}}/2p + \kappa/p}\right) \tag{3.2}$$

In their analysis they noted that, whilst electron spin exchange is only really significant at higher radical concentrations, nitrogen spin relaxation effects are concentration independent and significant even when little radical is used. They found their theory to be consistent with data they collected at 0.35 T.

An alternative for calculating the electron spin saturation in a DNP experiment was proposed in 2009 by Sezer et al. [125]. Here, semi-classical theory was used to treat the electron-nitrogen interaction, whilst ignoring the relaxation effects of coupling to the proton spin. This method, for the first time, explicitly accounted for spin-spin relaxation of the electron and obtained DNP enhancement values (using ξ from Reference [40]) as a function of frequency that closely replicate experimental values at 9.2 T. This approach has been shown to describe experiments well provided the input parameters can be determined: the frequency and strength of the microwave field, the electron spin-lattice and spin-spin relaxation times, the Heisenberg exchange rate and the magnetic tensors. Independent measurements can often be made of these parameters using EPR, however, the information is not always obtainable for a given setup, especially at high-field. In the example given by Sezer et al., approximations had to be made for T_{1S} and the microwave field strength. The usefulness of this as a general approach is further brought into question by the fact that it is only valid in the regime of fast tumbling. This is the case for most high-field liquid DNP experiments at present, which often utilise small nitroxide radicals, but the calculations may break down for radicals tethered to macromolecules or larger polarising agents (such as the biradicals proposed to induce a cross-effect, see Section 3.4).

Finally, after years of theoretical debate in the literature, Türke et al. [31] applied an experimental strategy for determining s — using pulsed ELDOR (electron double resonance) to pump one hyperfine EPR line whilst monitoring a coupled hyperfine line. This was demonstrated with TEMPONE-D, ^{15}N at 0.35 T and found to give a coupling factor of $\xi = 0.33 \pm 0.02$ consistent with NMRD and MD calculations (see Section 3.5.1), providing further validation for those approaches.

As demonstrated by the above discussion, determining electron spin saturation for nitroxide radicals is non-trivial, and far from the simplistic view of the early 1960s. The work of Türke, Sezer and co-workers presents a very strong case for determination of s through either NMRD, MD or pulsed ELDOR, at least at the field strengths currently available. However, avoiding the issue of saturation (by comparing distinguishable nuclei within the same sample and calculating ξ ratios) may be a necessary tactic for situations where such measurements and calculations are not readily available. This has been demonstrated by Krummenacker et al. [98] and is adopted by the author in Chapter 6.

Other than extracting precise values of s from theory and experiment, simply maximising it is also an important goal. To this end, Höfer et al. [13] attempted a 'dual irradiation' DNP experiment with 2.5 mM ^{2}H/^{15}N TEMPONE in water

at 0.35 T, where irradiation of both hyperfine lines was attempted simultaneously in an effort to boost the NMR signal. This was accomplished with two separate microwave sources and two separate amplifiers combining to give a maximum total power of 1.5 W. However, they found no benefit to this method, providing yet more data supporting the mixing of hyperfine lines via electron spin exchange and nuclear spin relaxation allowing s to approach 1. A similar approach has been attempted at 3.4 T for the first time, and is presented in Chapter 7.

Chapter 4

Experimental details

Liquid-state dynamic nuclear polarisation experiments provide results for the vast majority of this thesis, and were all conducted on the same spectrometer at a magnetic field of 3.35 T. There are many texts on NMR and EPR hardware which give detailed accounts of their design and physical properties, for example, see references [126], [16], [17], [27], [26] and [93]. However, a detailed discussion of equipment is beyond the scope of this study and only a brief summary will be given here; though particular attention will be given to any non-standard equipment and special techniques developed in or utilised in the work reported in this thesis. This chapter will first give a description of the hardware used, followed by details of the sample preparation techniques and experimental parameters used to obtain the results presented in the following chapters.

4.1 A 94 GHz spectrometer for in-situ DNP-NMR at 3.4 T

In order to carry out microwave-driven DNP-NMR experiments, the primary additions required to an NMR spectrometer are a microwave source, a suitable double resonance probe, and a system to transfer the microwaves from the source and couple them into the probe. A paramagnetic species is also required in the sample, usually in the form of a free radical polarising agent; this aspect of the DNP experiment will be discussed in Section 4.2.

A vertical-field Bruker 150 mm bore 7 T magnet was used at 3.35 T (corresponding to a proton NMR frequency of 143 MHz), as well as a water-cooled sweep coil leaving a bore of ∼88 mm. This was combined with a modified ENDOR (electron nuclear double resonance) probe connected to a Varian/Chemagnetics NMR

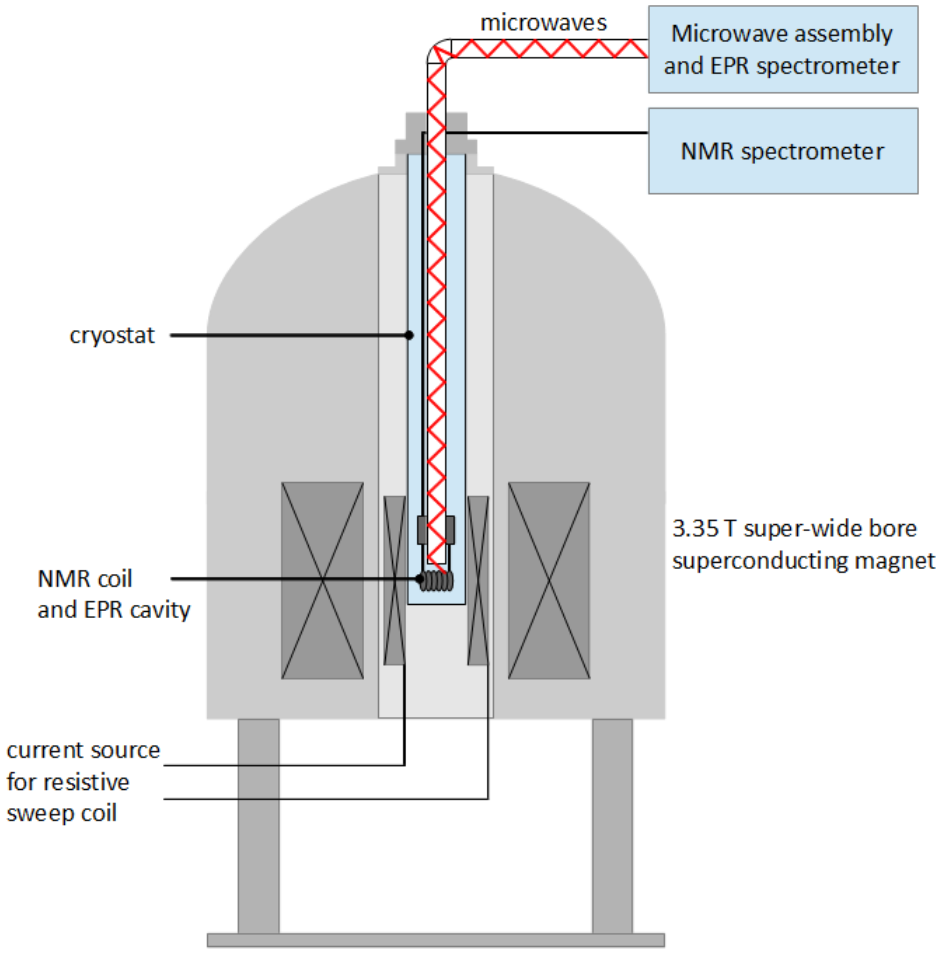

Figure 4.1: 94 GHz spectrometer for in-situ DNP-NMR at 3.35 T

console to allow NMR detection. The microwaves were provided by a Bruker W-band EPR system and an extended interaction klystron (EIK) amplifier. This setup enables high-power (up to $\sim$ 100 W) continuous-wave (CW)-DNP experiments at a microwave frequency of 94 GHz. A schematic representation of the spectrometer is shown in Figure 4.1 and a photograph of the experimental setup is given in Figure 4.2.

4.1.1 Microwave source

The type of microwave source implemented in a DNP spectrometer is largely dependent on the experiments that are to be performed. In general, a source is required to be stable and produce sufficient power at the electron resonance frequency corresponding to the NMR frequency being used — here, 94 GHz. The power required

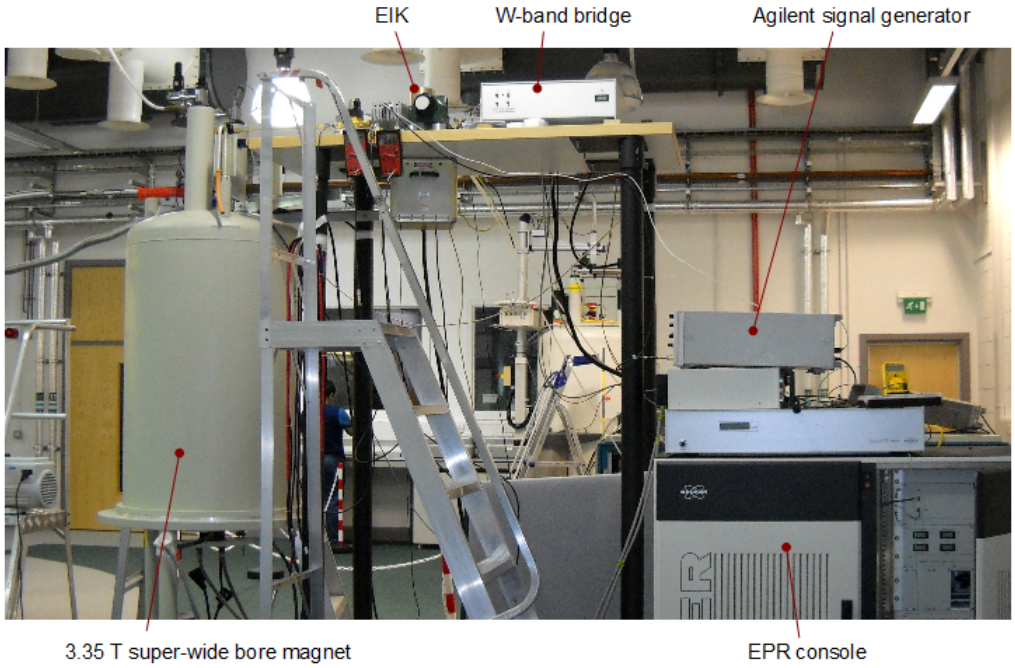

Figure 4.2: Photograph of the Warwick 94 GHz DNP-NMR spectrometer.

will depend on the nature of the experiments and the rest of the instrumentation. For example, in static experiments, a high-Q resonant microwave cavity may be used lowering the microwave power requirements; in magic-angle-spinning (MAS) experiments, on the other hand, the lack of a resonant structure necessitates the use of high-power sources. There are many different types of microwave generator available, but they can be broadly grouped into two categories: solid-state sources, such as Gunn and IMPATT diodes; and vacuum electronic devices, such as klystrons, travelling wave tube (TWT) amplifiers and gyrotrons. For an overview of common microwave generators used in EPR, the reader is referred to reference [93], and for more information on vacuum electronics see references [127] and [128].

This spectrometer utilises both technologies. A Bruker ELEXSYS E680 EPR spectrometer with a W-band microwave bridge operating at 94 GHz is the microwave source. The W-band bridge was modified to enable switching between two paths: one provides relatively low powers (<50 mW) directly from the microwave circulator to the EPR/DNP probe; and another provides high powers to the probe (up to ∼100 W in CW or pulsed mode) by switching the microwaves before the circulator to an extended interaction klystron (EIK) amplifier (see Figure 4.12). The EIK was used for DNP experiments where the EPR receiver system is not needed, whilst the low power path was used when acquiring EPR spectra. A relatively high-Q

microwave cavity was used in all the DNP experiments reported here, so not all of the EIK output power was required. A 10.5 dB directional coupler was used after the EIK in order to limit the power to the probe as well as protect the amplifier from any unwanted reflected power. Using the EIK, up to ∼9 W can be delivered to the probe with excess power being dumped into a high power load. Details of this spectrometer, and initial results demonstrating the effectiveness of the system can be found in reference [43].

Figure 4.3 shows a schematic of the W-band bridge. A Gunn oscillator inside the bridge supplies 84.5 GHz microwaves to a directional coupler that divides the power to the upconverter and downconverter. An intermediate frequency (IF) in the range of 9.2–9.9 GHz (X-band) is sent, via a microwave switch, to the upconverter. The upconverter combines the IF with the 84.5 GHz from the oscillator to generate 94 GHz microwaves. This signal leaves the bridge via the circulator. The EPR signal later returns from the cavity via the circulator and is directed towards a low-noise amplifier and the downconverter where it is mixed with the IF frequency and leaves the W-band bridge at the IF output. All microwave pulses and detection are carried out at ∼9.5 GHz.

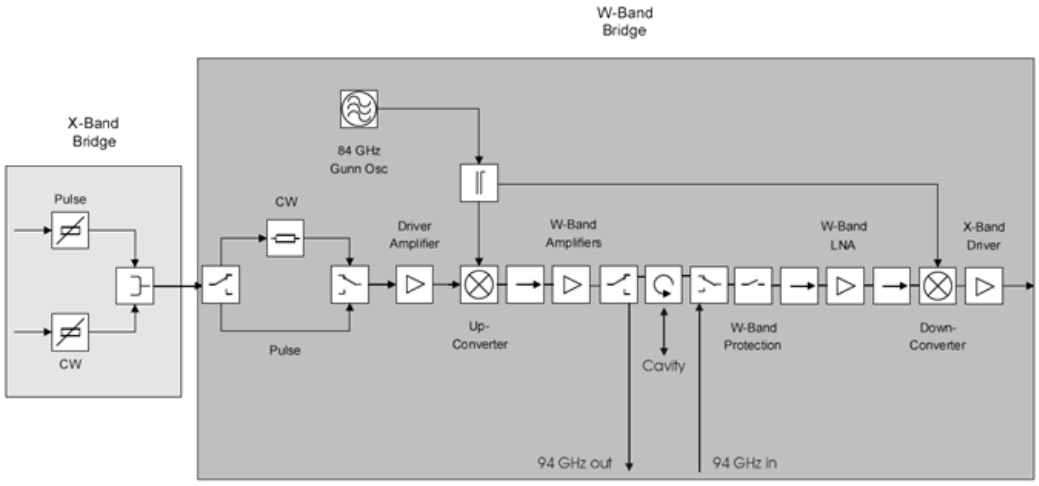

Figure 4.3: Schematic of W-band microwave bridge for Bruker ELEXSYS E680 EPR system.

Extended interaction klystron amplifier

The EIK amplifier utilised in this spectrometer (Varian VKB246321) was manufactured by Communications & Power Industries Canada. It is an air-cooled EIK which

can produce ∼100 W of continuous-wave output power, with a 3 dB bandwidth of 300 MHz. It has a typical gain of +43 dB for input powers up to about 5 mW, after which the gain begins to decrease, eventually reaching a maximum output power of about 110 W for 10 mW input power, see Figure 4.4.

4.1.2 Modified ENDOR probe and cavity

Microwaves from the bridge are transferred via a combination of Q-band and W-band waveguide (also known as WR-22 and WR-10) through a switch into a modified Bruker EN600-1021H 94 GHz ENDOR probe. The probe was modified so that the sample is loaded and positioned perpendicular to the axis of the probe and hence the B_0 field in the vertical-bore NMR magnet; standard EPR setups, in contrast, usually use horizontal B_0 fields. A cylindrical microwave cavity with an unloaded $Q \sim 3000$ was utilised, with the NMR r.f. coils wrapped around the outside (see Figure 4.5). The cavity operates in TE_{011} mode, has an inner diameter of slightly larger than 4 mm and a length of 4–5 mm. The most sensitive region of the cavity has previously been found to have a full width at half maximum of ∼2.5 mm by plotting EPR signal intensity as a function of position using a small sample [130]. The successful application of this probe for DNP has been demonstrated [43, 130]. Whilst the performance is optimised for use with microwaves, leading to very good coupling, its properties for NMR are not so good. The RF homogeneity is poor and the filling factor of the coil is at most 6%, leading to low sensitivity.

Cavities can be thought of as metal boxes which have dimensions similar to the wavelengths of the microwaves with which they are to be used. Modes are chosen to maximise the magnetic component of the microwaves whilst minimising the electric component at the centre of the cavity where the sample is positioned. This functions to amplify weak signals so that they can be detected, whilst minimisation of the electric field reduces sample heating; which is of particular importance for dielectrically lossy samples such as water, the solvent utilised in most of the experiments presented in this thesis.

Resonant cavities should be critically coupled to the transmission waveguide, i.e. matched to it so that no power is reflected. This is achieved by manually adjusting the probe. When the electron spins in the sample are resonant, the impedance of the system changes, power is reflected back towards the circulator and an EPR signal is detected.

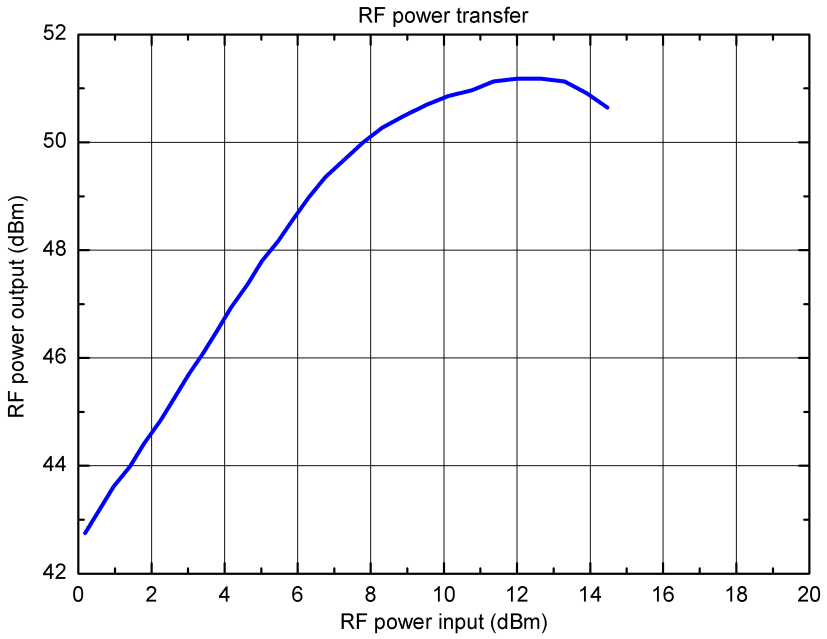

(a) Typical EIK output power as a function of drive power. From datasheet for Model Series VKB 2463, not specific to amplifier [129].

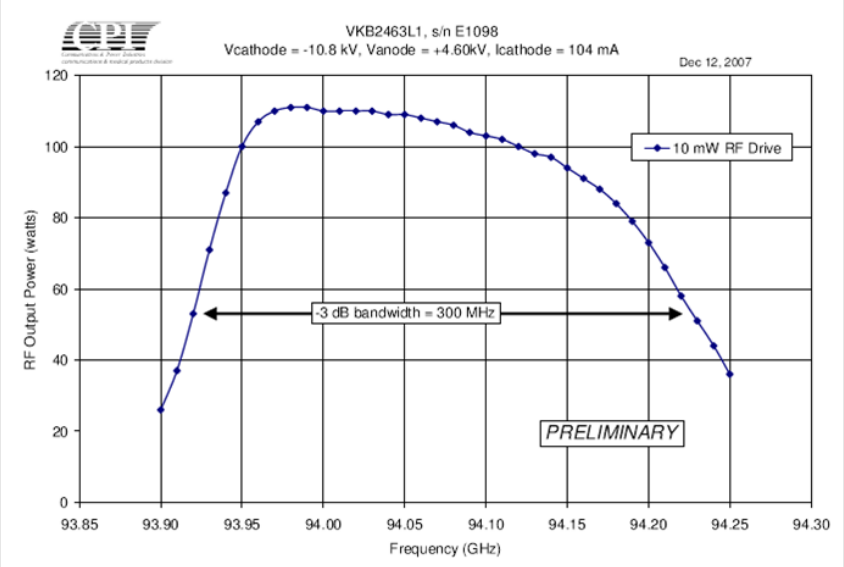

(b) Frequency dependence of EIK output power. Measured by CPI for specific amplifier being used.

Figure 4.4: EIK amplifier characteristics.

4.1.3 NMR spectrometer

A Varian/Chemagnetics Infinity-600 NMR console was used to acquire NMR spectra, and connected to the EPR console in order to provide the correct timings of

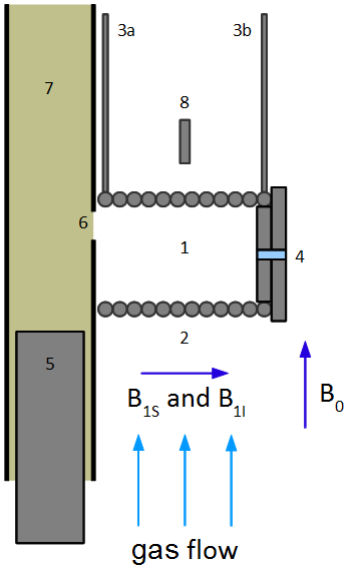

Figure 4.5: Diagram of modified ENDOR probe: (1) W-band cavity, (2) RF coil, (3a,b) RF leads, (4) sample access, (5) variable tuner, (6) coupling iris, (7) waveguide to microwave assembly, (8) thermocouple [43].

the microwave and NMR acquisition pulses.

The ability to sweep the magnetic field was required since CW-EPR is usually carried out at fixed frequency; NMR, in contrast, is usually carried out at fixed field. This was achieved by positioning a water-cooled solenoid inside the magnet bore, which was powered by an Oxford Instruments IPS 120-10 superconducting magnet power supply. This sweep coil (manufactured in-house) provides a linear field sweep of $\pm$350 G, which was calibrated using the EPR spectrum of the Mn^{2+} ion in MgO.

The choice of a Bruker super-wide bore magnet allowed more space for the resistive sweep coil, as well as a resistive shim coil and an Oxford Instruments SpectrostatNMR liquid helium continuous-flow cryostat that can allow measurements between 2.7 and 400 K. Unless otherwise stated, all DNP experiments in Chapters 5 and 6 were carried out with a continuous flow of nitrogen to stabilise the cavity at a base temperature of about 6°C. This temperature was measured using a thermocouple close to the cavity (see Figure 4.5).

4.2 Sample preparation and positioning

The nitroxide radical TEMPOL (4-hydroxy-2,2,6,6-tetramethylpiperidine-1-oxyl, also known as 4-hydroxy-TEMPO), with ^{14}N at natural abundance, was used as the po-

larising agent in the majority of the studies presented in this thesis. Section 7.3 describes the results of experiments using a similar nitroxide radical that has been deuterated and labelled with ^{15}N: 4-oxo-TEMPO-d$_{16}$-^{15}N. The structures of these two radicals are shown in Figure 4.6.

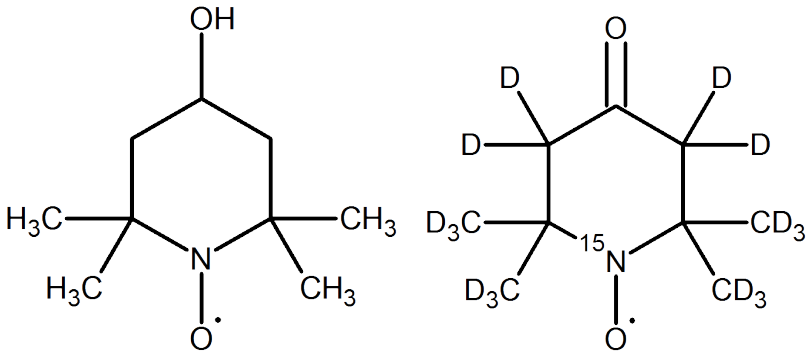

(a) TEMPOL (b) 4-oxo-TEMPO-d$_{16}$-^{15}N

Figure 4.6: Structures of derivatives of the nitroxide free radical TEMPO.

For all samples, the solutes were simply dissolved in solvent (water or toluene) by mixing. In the case of organic compounds (as in Chapter 6), the samples were prepared with an amount of solute approaching their maximum water solubility in order to get as large a signal as possible.

Unless otherwise stated, sample tubes were prepared using the following procedure:

- Sample was drawn into a quartz capillary tube with 0.1/0.4 mm ID/OD (inner/outer diameter), and the ends were sealed with a fast-setting epoxy resin (Araldite 2012) to prevent sample from leaking out or evaporating.
- The sealed capillary tube was inserted into a larger quartz capillary tube with 0.7/0.87 mm ID/OD. A slow-setting epoxy resin (Araldite 2011) was then injected into the larger capillary to reinforce the seals of the inner tube (see Figure 4.7).
- The epoxy-resin was allowed to cure overnight before beginning experiments.

Typical inner tube lengths, i.e. sample lengths, were approximately 10 mm long (typical volume $\sim$ 80 nl). This is significantly longer than the length of the cavity ($\sim$4–5 mm), to ensure the sample completely fills the cavity and also that the epoxy resin remains outside, thereby minimising dielectric loss of microwaves. The penetration depth of 94 GHz microwaves in water is 0.24 mm [95], so very narrow

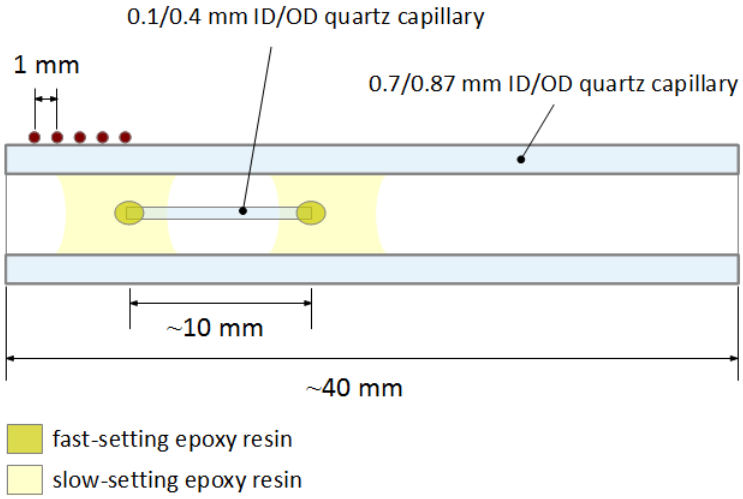

Figure 4.7: Typical sample. Surface of outer capillary tube marked with red dots with a separation of 1 mm in order to ensure proper sample positioning in the sample holder and cavity.

tubes had to be used for all samples dissolved in water; small samples also helped to reduce heating effects.

4.3 One-pulse NMR experiment

A simple one-pulse NMR experiment was used before any DNP experiments were done. This gave a reference for calculating the DNP enhancement, and in Chapters 5 and 6 the known proton chemical shift of water was used as an internal reference for the chemical shift scale and allowed temperature changes to be calculated. The simple pulse sequence, with a 90° pulse, is shown in Figure 4.8. The delay between the r.f. pulse and acquisition is indicated as the 'deadtime', where the spectrometer cannot record an NMR signal as electronic components such as amplifiers, filters and the receiver cannot switch off instantaneously.

4.4 Nuclear T_1 measurements — inversion-recovery and saturation-recovery experiments

Measurements of the nuclear longitudinal relaxation time T_1 were made at 100 MHz, 143 MHz, 284 MHz and 300 MHz. Where possible, measurements were made at 143 MHz, i.e. on the 94 GHz/143 MHz DNP spectrometer, so that direct comparisons with DNP enhancements at the same frequency could be made. However, some

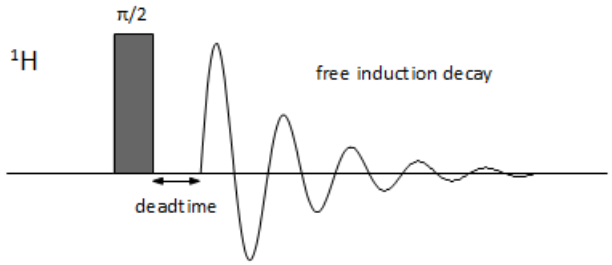

Figure 4.8: One-pulse sequence.

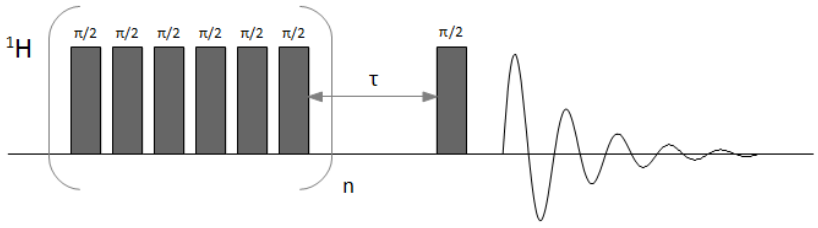

(a) Saturation-recovery

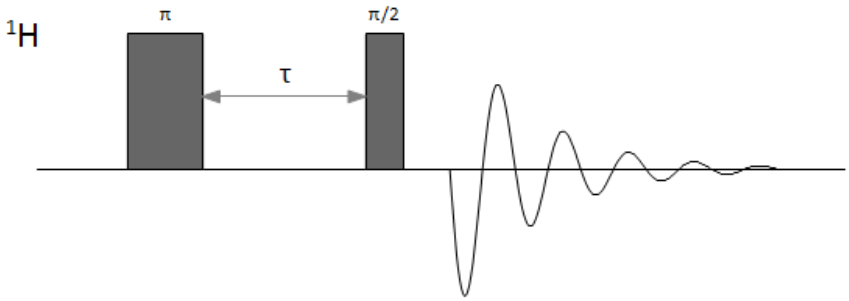

(b) Inversion-recovery

Figure 4.9: Pulse sequences used to measure spin-lattice relaxation time T_1.

measurements were made at different magnetic fields either for reasons of improved resolution at higher fields, or for better sensitivity when measuring non-doped samples. The choice of field is rationalised in the relevant sections in Chapter 6. Two pulse sequences were utilised: saturation-recovery and inversion-recovery (see Figure 4.9).

In both experiments, the magnetisation is perturbed away from equilibrium and immediately after it begins an exponential recovery with characteristic time T_1; after a delay τ an FID is acquired. The signal is proportional to the z-magnetisation $M_z(\tau)$ that has recovered in time τ, so by incrementally increasing this delay, the longitudinal magnetisation can be effectively sampled at various points in its recov-

ery. T_1 can then be calculated from Equation 4.1 for a saturation-recovery experiment, where the initial set of pulses (almost) eliminates the net z-magnetisation; or from Equation 4.2 for an inversion-recovery experiment, where the initial 180° pulse results in magnetisation in the $-z$-direction.

$$M_{z,\mathrm{sat}}(\tau) = M_0(1 - \exp(-\tau/T_1)) \tag{4.1}$$

$$M_{z,\mathrm{inv}}(\tau) = M_0(1 - 2\exp(-\tau/T_1)) \tag{4.2}$$

Both methods have their merits. With an inversion-recovery sequence, the magnetisation recovers over a larger range, i.e. $2M_0$. However, it relies on full longitudinal magnetisation at the start of each acquisition, meaning there must be a delay of at least $5T_1$ between scans. The saturation-recovery sequence on the other hand can be repeated with very short delays between successive acquisitions. This was particularly advantageous on the 143 MHz/94 GHz spectrometer when very small samples were used that gave relatively poor signal-to-noise. In general, both sequences were used for the studies in this thesis, depending partly on the availability of pulse programmes on the spectrometer being used to make the measurements.

4.5 Acquisition of CW-EPR spectra

CW-EPR spectra were recorded before each DNP experiment using the low-power side of the Bruker W-band bridge, typical power used was ∼40 μW (see Figure 4.13 for power measurements). The microwave frequency was fixed and the magnetic field swept. This is a necessary step to determine the field to use for a DNP experiment so that the microwaves are irradiating the desired electron resonance. The central transition (see Figure 4.10) was irradiated for all the DNP experiments in Chapters 5 and 6.

4.6 Overhauser DNP experiments

The acquisition of DNP-NMR spectra were triggered by the EPR spectrometer so that the NMR acquisition pulses were timed to immediately follow the microwave pulses, see Figure 4.11. In Chapter 5 the build up of magnetisation/enhancement is measured as a function of irradiation time and a pulse sequence like that in Figure 4.11 is used, where the EPR console provides a microwave pulse followed by an acquisition trigger pulse and NMR acquisition during a period of delay between microwave pulses. For all the experiments in Chapters 6 and 7, the EPR spectrometer

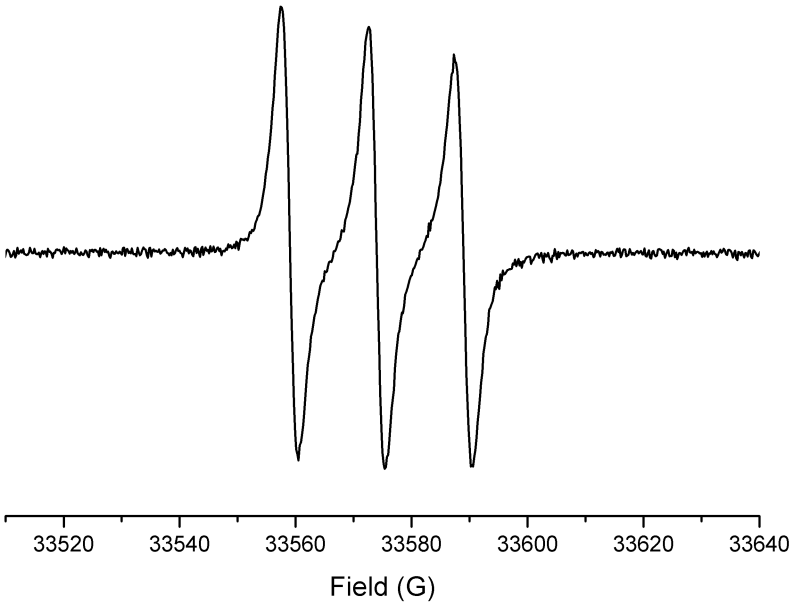

Figure 4.10: Example of 94 GHz CW-EPR spectrum for 100 mM TEMPOL radical in water at room temperature.

still operated in 'pulse-mode' (necessary to utilise the EIK) but pseudo-continuous-wave microwave irradiation was used throughout the experiment: the microwave pulses were repeated with a typical delay of 30 μs, i.e. pulsed irradiation with a duty cycle of 99.997%. In this case, the acquisition trigger pulse was still applied and effectively used to set a pulse delay for the NMR experiment. For simplicity, this type of irradiation will hereinafter be referred to as 'continuous-wave' irradiation. Whilst in 'pulse-mode', the microwave power is set by altering the transmitter level of the receiver and not the attenuation of the bridge; the actual corresponding output powers were measured up to a transmitter level of 23.003% (see Figure 4.15).

All DNP experiments in Chapters 5 and 6, unless otherwise stated, were conducted using a base temperature of approximately 6°C using a flow of heated nitrogen gas and measured by a thermocouple external to but near the cavity. Subsequent temperature increases resulting from microwave irradiation during the DNP experiments were measured using the ^{1}H NMR shift, δ_{water}, in ppm and Equation 4.3 where T is the temperature of the sample in °C [131].

$$\delta_{\text{water}} = 4.76 - 0.01(T - 25) \tag{4.3}$$

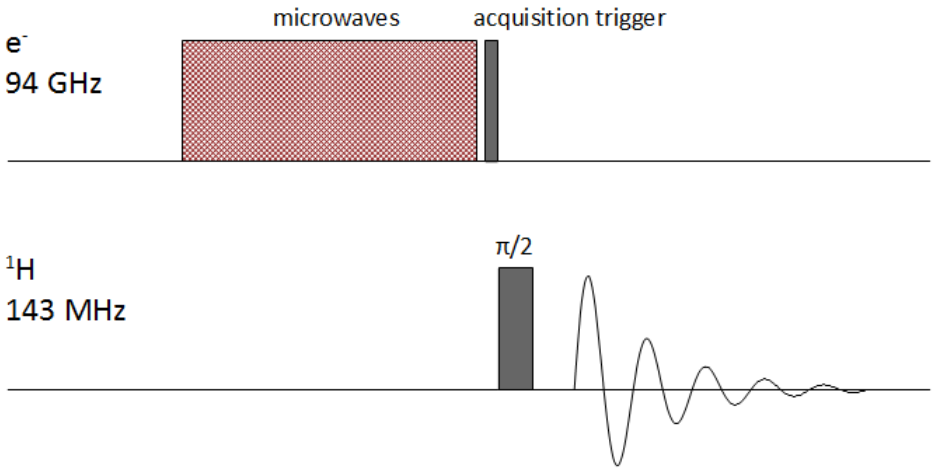

Figure 4.11: Typical pulse sequence for Overhauser DNP experiments.

4.7 Simultaneous use of two independent microwave sources

TEMPOL in toluene was chosen as the sample to study as toluene exhibits very low dielectric loss and so is not so susceptible to microwave heating, therefore a larger sample could be used and in turn a good signal-to-noise ratio obtained much faster. The ^{1}H NMR spectrum of toluene can also be easily resolved into two lines (ring protons and methyl protons) on this spectrometer [43]. Some changes to the experimental setup were made in order to accommodate a second microwave source in the system (see Figure 4.12).

An Agilent Technologies E8257D 250 kHz–50 GHz PSG Analog Signal Generator was connected to a S10MS-AG 70–110 GHz Millimeter Wave Source Module (OML, Inc.) to produce W-band microwaves. The mm-wave source module, designed for use with Agilent PSG signal generators, multiplies the output of the signal generator by a factor of 6. Its output frequency specifications are directly proportional to the generator characteristics. The Agilent PSG generators typically have resolution in the mHz range, giving the mm-wave source module a high frequency resolution even at high carrier frequencies. The source module produces a fixed output power of approximately 3.7 mW, so a rotary vane variable attenuator (Flann Microwave Instruments, Ltd.) providing 0–60 dB attenuation was attached to the output of the module to allow variation of the output power.

The output of the variable attenuator and the high-power side of the Bruker bridge were connected to the collinear arms of a magic-T, with the H-plane port (also known as the sum port, where the signals are added together [132]) connected

to the EIK.

In order to properly tune the microwave cavity, the low-power side of the Bruker bridge had to remain connected to the microwave setup. To accommodate the extra space required for the attenuator and source module, additional lengths and bends of oversized waveguide (Q-band) totalling approximately 50 cm in length were used to the connect the bridge to the microwave switch. This low-power channel could then continue to be used to run CW-EPR experiments, which were used to determine the approximate input frequency required for the Agilent signal generator to irradiate the desired hyperfine EPR lines. The additional loss of power from the extra waveguide did not hinder easy acquisition of EPR spectra.

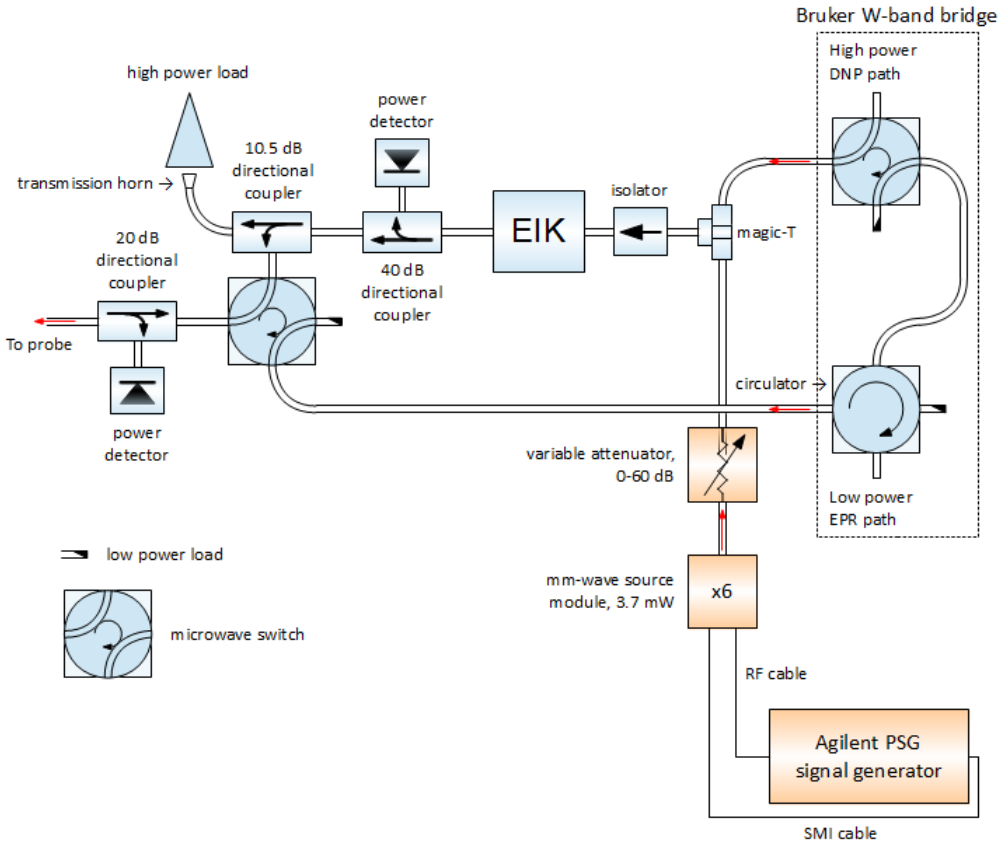

Figure 4.12: Schematic of the microwave assembly utilising two microwave sources. The orange coloured components were added as the second microwave source, whilst the blue coloured components constitute the original setup for the experiments in Chapters 5 and 6.

A Hewlett Packard W8486A Power Sensor (maximum power 0.2 W) and Hewlett Packard 437B Power Meter were used to make power measurements at various points in the microwave system before the EIK. The output of the millimetre

source module was measured and found to be in reasonable agreement with the specifications of fixed output power of approximately +5 dBm for an input power (signal generator output power) of +16 dBm. This signal generator output power was used for all subsequent experiments, as recommended by the manufacturer. The output of the low-power (EPR) side of the microwave bridge was measured for the full range of bridge attenuations and is presented in Figure 4.13. There may be some loss due to the use of a Q-band to W-band converter which had to be used in order to make the measurements as the sensor is designed for use with WR-10 waveguide. In all the EPR experiments presented in this thesis, oversized (Q-band) waveguide was used from the bridge to just before the switch where it was converted to W-band. Similar measurements were then made for the high-power (DNP) side of the bridge (see Figure 4.14). The power output of the magic-T was also measured; a comparison of the two data sets showed a loss in power of between 4 and 5.5 dB for the range measured. Finally, both the Bruker and Agilent sources were used simultaneously and the output of the magic-T monitored (see Figure 4.15). Data were recorded for the case where both sources were irradiating at the same frequency, and the case where they were irradiating at different frequencies. It was found that 80–98% of the total input power was transmitted. Despite the significant losses in transporting the microwaves to the magic-T from the source, the magic-T itself seems to be fairly efficient.

A range of experiments were carried out to investigate the effect of irradiating two hyperfine lines simultaneously. The appropriate field for irradiating a specific hyperfine line using the Bruker bridge was found in the usual way, i.e. a CW-EPR experiment. However, in order to find the exact frequency of irradiation (required for the input of the Agilent signal generator), the signal generator was used on its own as the source for DNP experiments, changing the microwave frequency incrementally, effectively 'sweeping' through the resonances and measuring the DNP enhancement (see Figure 4.16). Specific details of the individual experiments will be given in Chapter 7.

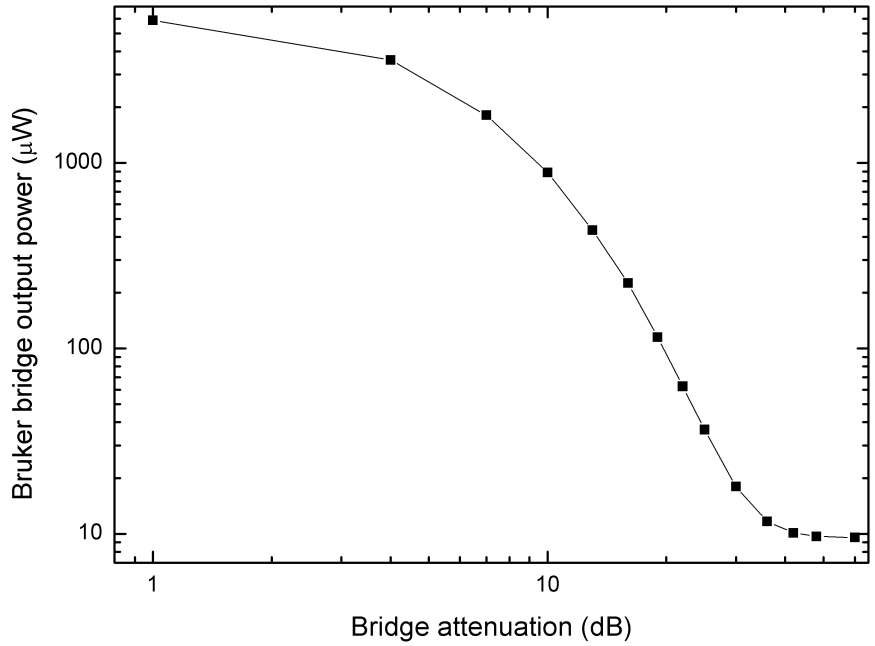

Figure 4.13: Output of low-power side of Bruker W-band bridge in CW-mode, measured using Hewlett Packard power meter.

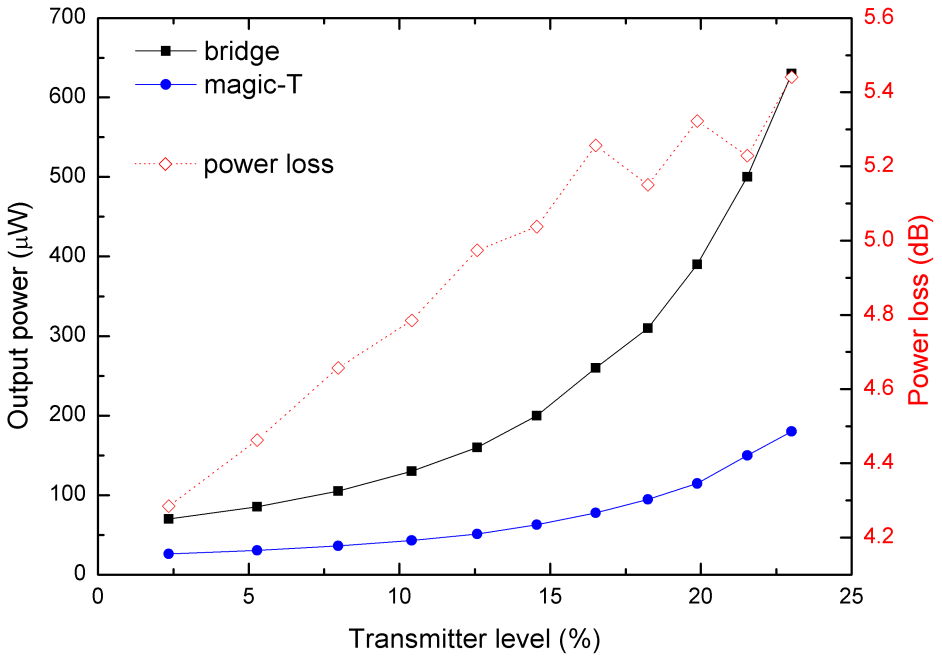

Figure 4.14: Output of high-power side of Bruker W-band bridge in pulse-mode, measured using Hewlett Packard power meter at the bridge and at the magic-T output. The loss in microwave power in travelling from the bridge through to the magic-T output is plotted in red (diamonds) and corresponds to the right-hand axis.

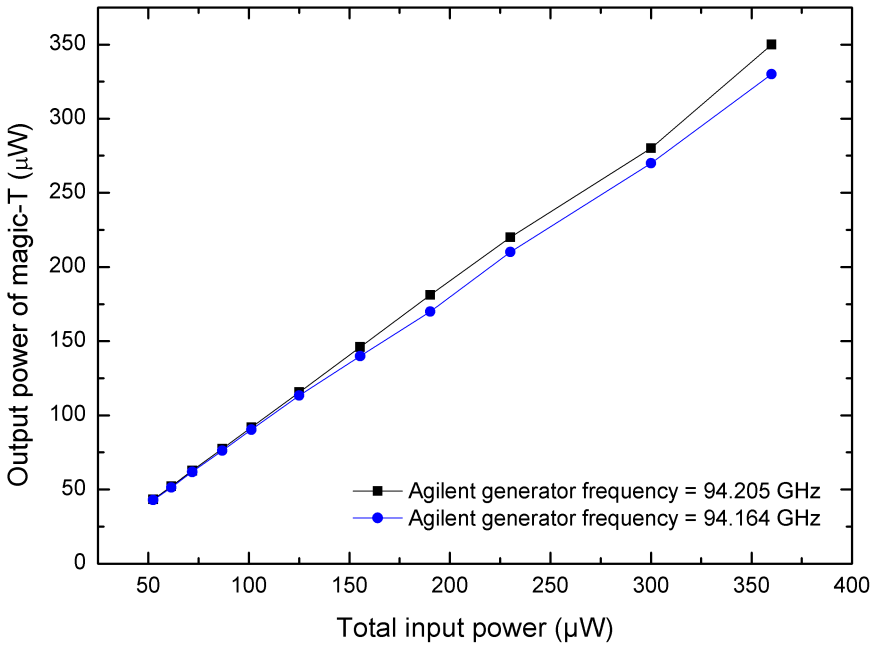

Figure 4.15: Output of magic-T when used with two sources simultaneously. The contributions to the total input power from each source is approximately equal.

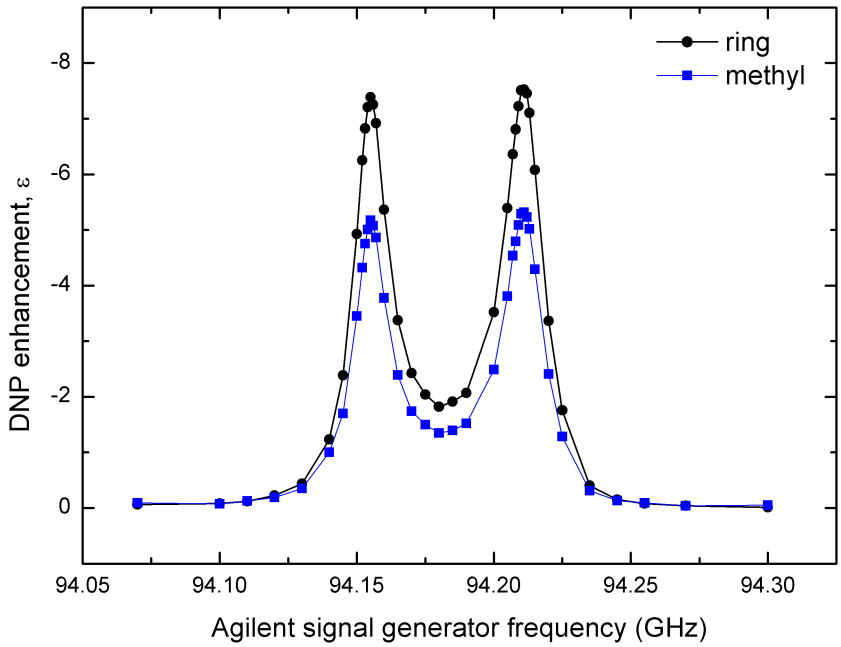

Figure 4.16: Agilent frequency 'sweep' in which DNP enhancement is plotted as a function of frequency; used to determine the required input frequency for two-source DNP experiments. DNP experiments were conducted on 5 mM 4-oxo-TEMPO-d_{16}-^{15}N in toluene at room temperature.

Chapter 5

DNP enhancement of water protons with TEMPOL radical

5.1 Introduction

Since the early years of DNP, it has been known that the enhancement in sensitivity resulting from the Overhauser effect in liquids decreases as the applied microwave frequency increases. In 1965, K. H. Hausser predicted that the coupling factor ξ, and hence enhancement, would rapidly drop off to a level which would not be large enough to be useful at the magnetic fields commonly used in modern NMR [5].

The effectiveness of Overhauser DNP at relatively low frequencies (X-band, 9.7 GHz electron Larmor frequency) has been well demonstrated, with Türke and Bennati achieving an enhancement of -178 — more than half of the maximum achievable enhancement $\varepsilon \sim -330$ [31].

However, it was not until recently that the original prediction of the practicality of Overhauser DNP at high fields has been brought into doubt. The last few years have provided numerous reports of increasingly large DNP enhancements in solutions from several European groups at W-band: In 2008, Höfer et al. achieved $\varepsilon \approx -40$ [113], followed by reports in 2010 of $\varepsilon \approx -50$ and $\varepsilon \approx -65$ by Kryukov et al. [43] and Villanueva-Garibay et al. [96], respectively.

A study of the temperature dependent enhancement of protons in water is presented in this chapter, where enhancements of ≈ -125 are obtained at W-band (94 GHz). These results have been previously published [130], where the author assisted in taking data and its subsequent analysis. Since the original publication of this work, further increases in enhancement ($\varepsilon \approx -165$) at W-band have been reported by van Bentum et al. [133]. In addition, a significant enhancement ($\varepsilon \approx -29$)

has been measured at 9.2 T (260 GHz electron Larmor frequency) by Denysenkov et al. [12], further casting doubt on the original theoretical predictions regarding high-field Overhauser DNP.

5.1.1 Polarisation of water protons

Due in part to its polar nature, many substances dissolve in water and it is sometimes referred to as 'the universal solvent'. It is ubiquitous in biology, and as such, is often the preferred solvent for biological applications. This motivates its study in NMR and DNP. However, it is extremely lossy at frequencies greater than ∼4 GHz. This creates difficulties for microwave-driven DNP, as the resulting heating from microwave irradiation can damage water-containing samples and leave the temperature an unknown variable. Thus, this heating leads to restrictions in sample sizes (see Section 4.2). Cavities are often employed in an attempt to overcome these problems, but this becomes practically very challenging at higher frequencies (shorter wavelengths), as the cavities must be manufactured with increasingly small dimensions, and some sample is unavoidably heated.

DNP of water has been measured at various magnetic fields using various polarising agents. Enhancements previously reported include: $\varepsilon \approx -170$ at 0.35 T using TEMPONE-D,^{15}N [95]; $\varepsilon \approx -65$ at 3.4 T using TEMPO [96]; and $\varepsilon \approx -29$ at 9.2 T using Fremy's Salt [12].

5.1.2 Factors reducing maximum enhancement

In order to understand the DNP enhancements ε obtained in experiments, the three factors which reduce the maximum achievable value must be understood, namely: the saturation factor, s; the leakage factor, f; and the coupling factor, ξ (see Section 2.3.2). For Overhauser DNP to be put to better use at high fields, a greater understanding of s and ξ in particular is essential.

$$\varepsilon = \xi f s \frac{\gamma_S}{\gamma_I} \tag{5.1}$$

At high radical concentrations, if the applied microwave field B_{1S} is strong enough to compete with the fast electron spin-lattice relaxation, then $s \approx 1$. Technology has now advanced to the state where high power sources are available that enable us to approach this limit. For example, EIKs have been used for $B_0 \leq 3.4$ T [92], and gyrotrons for $B_0 \geq 3.4$ T [134] [135]. It is also possible to use low power sources with resonant cavities up to fields of 9.4 T.

The leakage factor can be measured with relative ease and approaches the limit $f \approx 1$ for the high radical concentrations used here.

Molecular dynamics (MD) calculations have been used by others to predict coupling factors for nitroxide radical solutions of: ξ less than $\sim$0.1 for $B_0 \sim 1$ T and less than $\sim$0.01 for $B_0 \sim 10$ T.

In this chapter, the temperature dependence of the DNP effect is analysed. The leakage factor does not depend strongly on temperature since the variables which contribute to it ($T_{1\mathrm{I}}$ and $T_{1\mathrm{I}0}$) have similar temperature dependencies. The coupling factor, however, depends on dipolar correlation times and therefore varies significantly with temperature [40] [121]. So in the case of high concentration and high applied microwave power, the DNP enhancement is strongly dependent on temperature mostly due to the coupling factor.

Previously, there has been insufficient information on heating during microwave irradiation in high-field liquid DNP experiments. This has made it difficult to extract the coupling factor from experimental data. It has also made it somewhat unproductive to compare many of the reported enhancements since the temperature has only been indirectly determined and was likely changing during measurements [95].

5.2 Experimental details

5.2.1 Sample preparation

TEMPOL radical was dissolved in H_2O in concentrations varying from 10 to 160 mM. The field strength was set so that the central line of the ^{14}N-hyperfine EPR triplet was resonant in all the DNP experiments presented here.

The typical sample length was $\sim$10 mm, where the sample was sealed in a 0.1/0.4 mm ID/OD quartz capillary tube using the method described in Section 4.2. One 2 mm length sample was prepared with a radical concentration of 100 mM. This was prepared in a similar way to the rest of the samples, except no secondary (slow-setting) epoxy resin was used to secure the primary epoxy seals. No degassing was performed on any of the samples.

5.2.2 Experiment

A maximum applied microwave power of 1.3 W was used unless otherwise stated and the NMR chemical shift was used to calculate the temperature (Equation 4.3).

A continuous flow of nitrogen gas was found to be ineffective at preventing

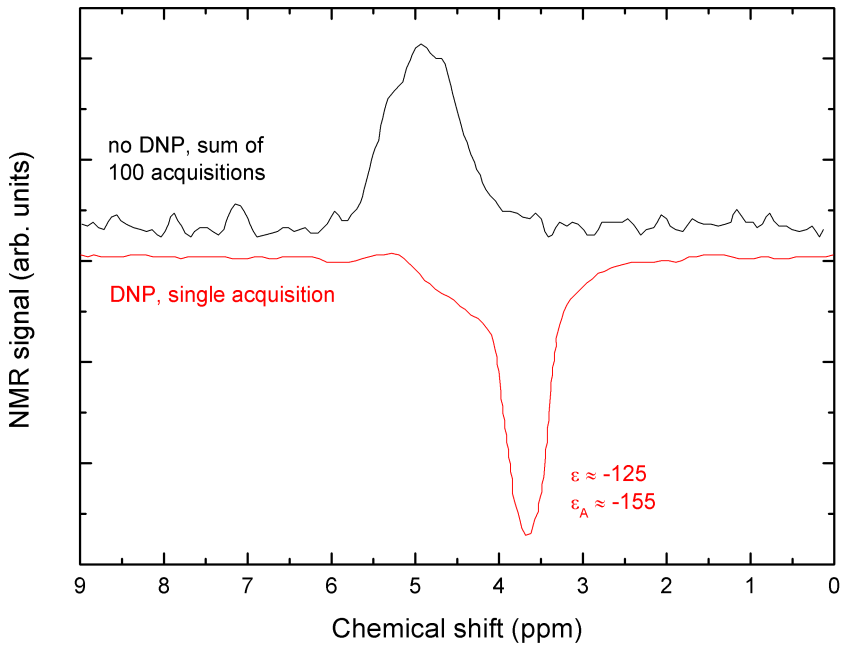

Figure 5.1: ^{1}H NMR spectra of water with 120 mM TEMPOL; top — no microwave irradiation, 100 acquisitions; bottom — 1.3 W microwave irradiation for one second, single acquisition.

significant sample heating, an effect previously noted by Türke et al. when they found the gas flow they applied was able to dissipate heat from the cavity to aid in the stability of the resonance conditions, but unable to prevent significant heating of the actual sample [95]. In the results that follow, a delay of at least 2 minutes was used between consecutive experiments to allow the sample to return to the base temperature of 6°C.

5.3 Results and discussion

5.3.1 Temperature dependence of enhancement, nuclear relaxation and EPR spectrum

An example of a DNP-enhanced ^{1}H NMR spectrum is shown in Figure 5.1. This was taken using a standard length (10 mm) sample of water with 120 mM TEMPOL and one second of 1.3 W microwave irradiation. An integrated enhancement of $\varepsilon \approx -125$ was obtained.

These spectra demonstrate a number of properties of our experimental setup. The enhanced spectrum is negative relative to the reference spectrum: this is because electron-nuclear dipolar coupling dominates the Overhauser effect in aqueous

solutions (see Chapter 2). The unenhanced spectrum appears to be a single broad peak, whilst the DNP spectrum seems to be composed of a narrow peak with a lower intensity, broader component. This is probably due to the effect of uneven heating of the 10 mm long sample which extends beyond the cavity and gives rise to a temperature gradient. As a result of this, it can be difficult to obtain reliable enhancement values, as what is actually being measured is an average polarisation which is less than the optimum value at the centre of the cavity. Therefore, unless otherwise stated, the following enhancement results will be calculated using Equation 5.2:

$$\varepsilon_{\mathrm{A}} = \frac{A_{\mathrm{enh}} - A_0}{A_0} \tag{5.2}$$

where A_{enh} and A_0 are the amplitudes of the enhanced and thermal equilibrium (taken at 6°C) NMR spectra, respectively. These values will be used in discussion of the behaviour of this system, although they do not account for the change in the Boltzmann distribution at different temperatures. This will be further discussed later. For the 10 mm long samples, ε was found to be $\sim$25% smaller than ε_{A} because there is less enhancement of the broad component. In reality, the true enhancement of the ^{1}H spins is neither ε_{A} nor ε. They can only serve as approximations if there exists a microwave magnetic field gradient or a temperature gradient in the system under study. Figure 5.1 also shows that the changes in chemical shift are much larger than the resolution limit caused by the magnetic field inhomogeneity and the faster relaxation at higher radical concentration, so the data to follow in this chapter are indicative of the instantaneous temperature and are even able to indicate its distribution through the sample.

The effect of radical concentration on the ^{1}H nuclear relaxation rate, $1/T_{1\mathrm{I}}$, is shown in Figure 5.2a. Concentrations from 10 mM to 160 mM were studied and, over this range, the nuclear relaxation rate was found to vary linearly with the concentration of TEMPOL c (as the frequency of encounters between the water and radical molecules increases); the rate of increase being 0.35 ± 0.02 s^{-1}mM^{-1}.

The temperature dependence of $T_{1\mathrm{I}}$ of a 160 mM TEMPOL in water sample is shown in Figure 5.2b. The sample temperature was varied using a flow of heated nitrogen gas and the temperature recorded using the thermocouple near the cavity. The relaxation time increases with the rise in temperature in an approximately linear fashion: increasing from 17 ms at 6°C to 85 ms at 89°C. The $T_{1\mathrm{I}}$ temperature dependence of pure water (scaled to agree at 6°C) is plotted along with the data, and it can be seen that the fractional change in $T_{1\mathrm{I}}$ of the doped sample (at the concentrations used here) is similar to that of pure water. Data with the temper-

ature calculated from the chemical shift (when heated using gas) are also plotted and yield similar behaviour to that of the thermocouple data, indicating that the shift is unaffected by the TEMPOL radical and thus giving further confidence to the analysis. However, whilst the agreement between the two temperature measurement methods appears good within experimental uncertainty, at high temperatures the thermocouple data indicates a slightly higher temperature compared with the chemical shift data. This is likely a result of poor thermal contact between the gas and sample, leading to a somewhat lower temperature of the sample itself than at the thermocouple position.

The change in chemical shift resulting from microwave irradiation is shown in Figure 5.3, with the calculated increase in temperature on the right-hand axis. Data are shown for radical concentrations of 80 mM, 120 mM and 160 mM for irradiation times up to one second (with irradiation periods up to five seconds for 80 mM and 120 mM shown in the inset), with temperatures >100°C being achieved in the sealed sample tubes. The change in temperature appears to be independent of the amount of TEMPOL in the sample and was fitted with a single exponential over the initial one second irradiation period, giving a characteristic time of $\tau_T = 0.25$s.

Figure 5.4 shows the increase in DNP enhancement with increasing microwave irradiation periods. This was measured for a range of concentrations (10 mM, 20 mM, 40 mM, 80 mM and 120 mM) and was found to vary in a similar way to temperature, but with different characteristic times for the different concentrations. There appears to be an approximately linear decrease in the characteristic time, τ, with increasing concentration at lower concentrations (10–80 mM); but this seems independent at higher concentrations (see inset of Figure 5.4). These characteristic times are significantly longer than those expected from the $T_{1\mathrm{I}}$ data at 6°C (see Figure 5.2a), for example: $T_{1\mathrm{I}} = 0.28$ s for the 10 mM sample, and is shorter for higher concentrations. Also, from the measurements in Figure 5.3, it has been established that the temperature varies on a timescale much less than one second. Therefore, the data for the enhancement as a function of time in Figure 5.4 are not characteristic of a single temperature and to properly plot ε as a function of t there must be a correction for the change in Boltzmann factor.

Due to the aforementioned problems with uneven heating in long samples, a shorter (2 mm long) sample was prepared despite potential difficulties with proper sealing. Using a sample length shorter than the cavity allowed the integrated enhancement to be measured as a function of microwave irradiation time (see Figure 5.5a). Note that the spectra of the short sample (see Figure 5.5a inset for example) are much more symmetric (cf. Figure 5.1) likely because of more even en-

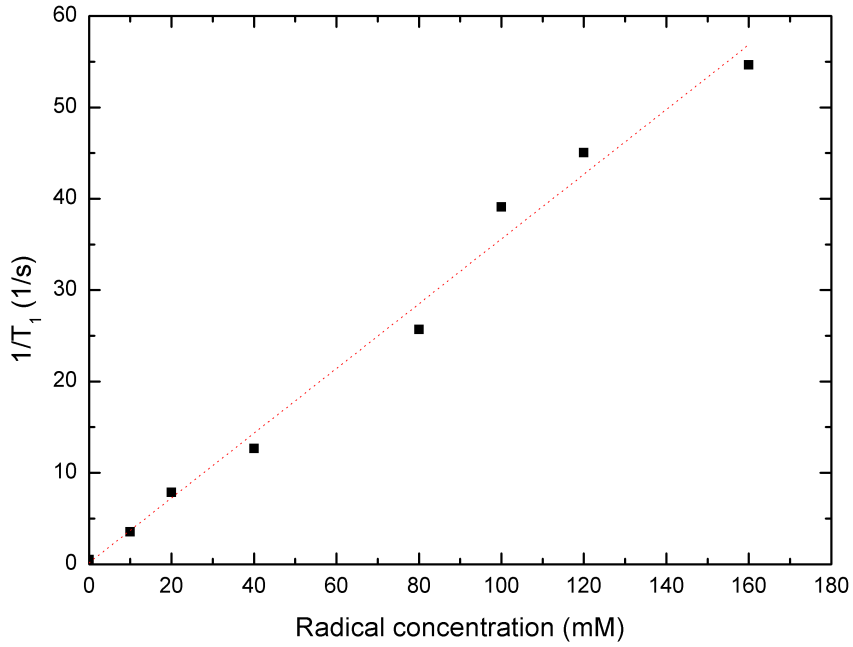

(a) Proton relaxation rate in water as a function of TEMPOL radical concentration. Dotted line — linear fit of data: $1/T_1 = (0.35 \pm 0.02)c$.

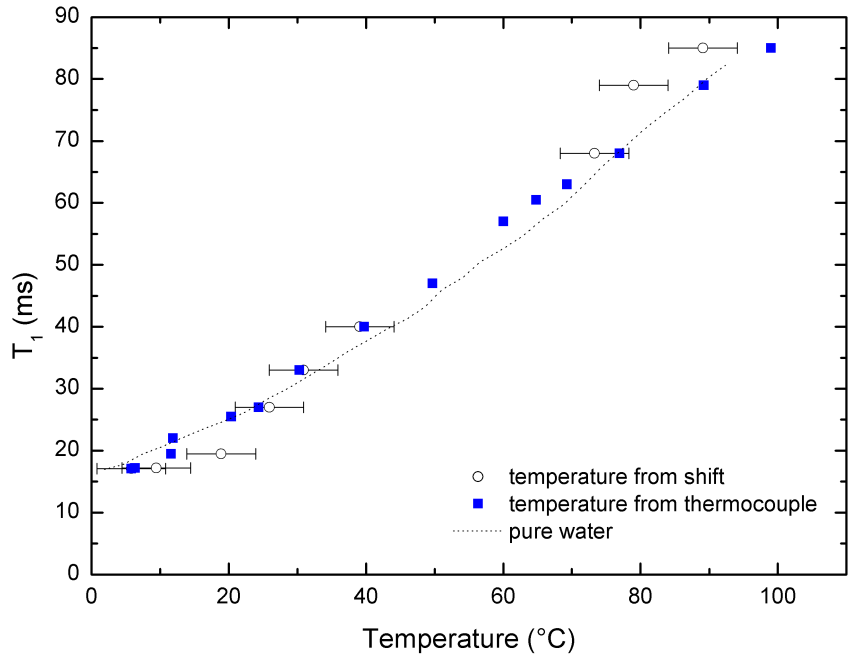

(b) Temperature dependence of proton $T_{1\mathrm{I}}$ in water doped with 160 mM TEMPOL. Data are shown with temperature indicated by chemical shift and by thermocouple external to cavity. The $T_{1\mathrm{I}}$ of pure water is shown as a dotted line and has been scaled to the doped sample value at 6°C [136].

Figure 5.2: Water proton spin-lattice relaxation rates.

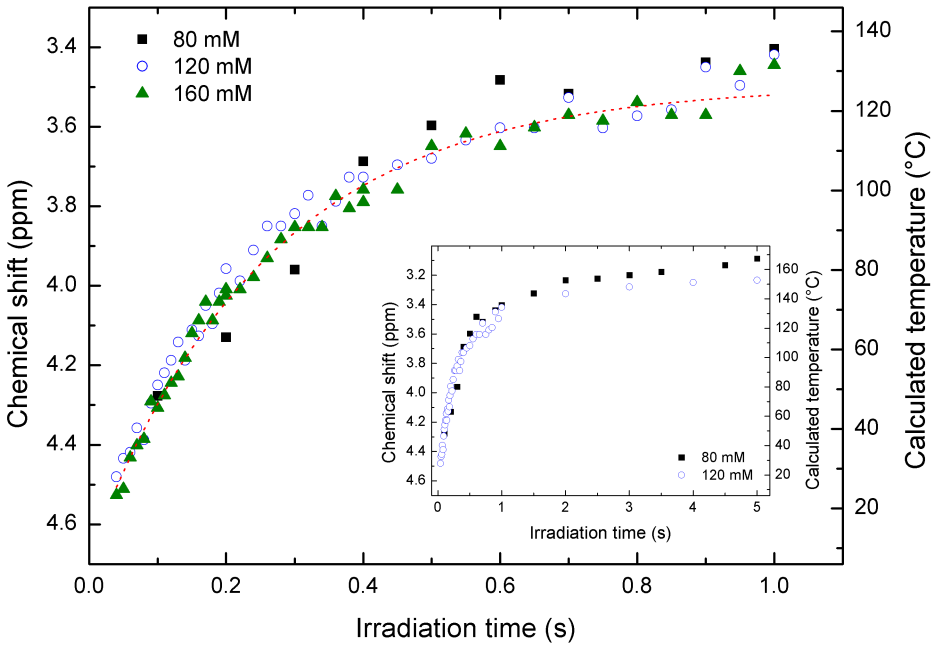

Figure 5.3: Proton chemical shift and inferred temperature in water as a function of duration of 1.3 W microwave irradiation, for different concentrations. Dotted line — fit of the form $(1-\exp(-t/\tau_T))$ with $\tau_T = 0.25$ s. The inset shows the same data for 80 mM and 120 mM over an extended irradiation period.

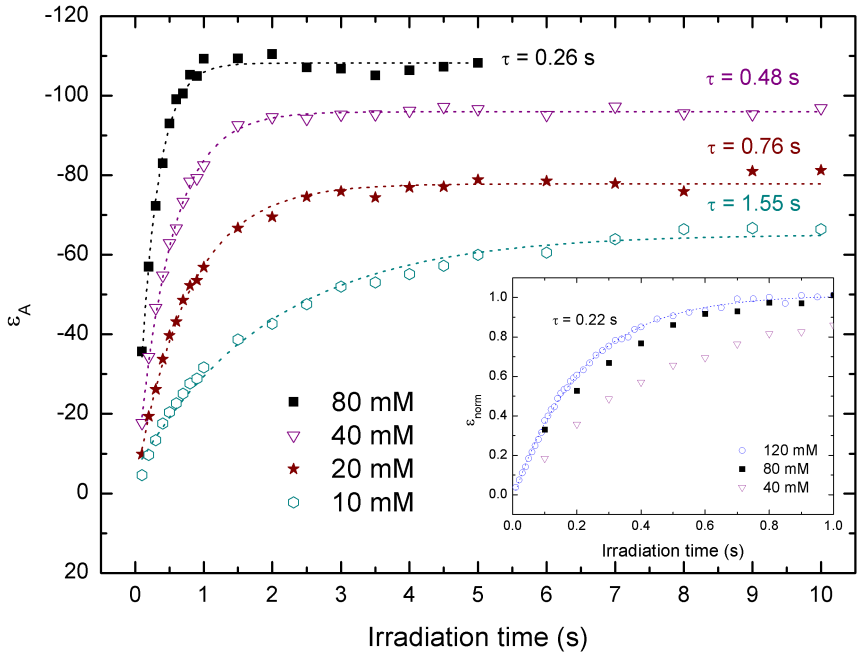

Figure 5.4: Enhancement as a function of 1.3 W microwave irradiation time for different radical concentrations. Dotted lines are single exponent fits of the data with time constants τ displayed. The inset shows the first second of irradiation for concentrations of 120 mM, 80 mM and 40 mM. The dotted line is once again a single exponent fit.

hancement and heating throughout the sample. Figure 5.5b shows that provided the nuclear relaxation is sufficiently fast ($T_{1\mathrm{I}} \ll 0.25$ s at 20°C) and the enhanced NMR spectra are sufficiently resolved to measure the shift accurately, the temperature dependence of ε can be found, and that this dependence is approximately linear in nature. The enhancements in Figure 5.5 were calculated with I_0 values that account for the change in Boltzmann factor as the temperature increases. This is important for the accurate determination of the coupling factor, ξ. The correction was not made previously, so ε_{A} in other figures presented here are not so useful for determining ξ and how it changes. They do, however, still show the increase in nuclear polarisation which is the aim of any DNP experiment.

The change in the CW-EPR spectrum with temperature of TEMPOL in water is shown for 40 mM and 120 mM concentrations in Figure 5.6. It can be seen that saturation is easier to achieve at either higher concentration or higher temperature. At higher temperatures, the dynamics of the molecules becomes faster and this rapid motion results in more frequent electron spin exchange. This is reflected in the spectrum which broadens and collapses into a single resonance as the sample is heated. The 120 mM spectra exhibit similar behaviour to the 40 mM, but the spectrum is narrower at higher temperatures. This narrowing makes the choice of field more crucial when conducting DNP experiments at higher concentrations and temperatures in order to optimise the electron saturation. There is also a shift of the resonance by ∼0.2 mT to a lower field from 6°C to 98°C.

The amplitude enhancement is plotted as a function of field in Figure 5.7. Data are shown for DNP experiments using 1.3 W and 250 mW microwaves. Integrated CW-EPR spectra (obtained with 18 μW microwave power) at 22°C and 98° are shown for comparison. The DNP spectra are broader, as expected, because of stronger $B_{1\mathrm{S}}$ fields. Note that the peak resulting from the higher power (temperature) DNP measurements (1.3 W) is shifted to a lower field. This is consistent with the shift seen in the CW-EPR spectra of Figure 5.6 and results from a drop of the cavity resonance frequency at high temperatures.

5.3.2 Modelling of data with time-step calculations using instantaneous $I_{\mathbf{enh}}$ and $T_{\mathbf{1I}}$ values

Time-step calculations were used to model the build-up of polarisation during irradiation and the enhancement as a function of temperature. Simple use of the Bloch equations is insufficient to describe the system under study, as microwave heating causes changes in the sample temperature on a timescale similar to the increase in ε at fixed temperature. The rapidly varying sample temperature (indicated in

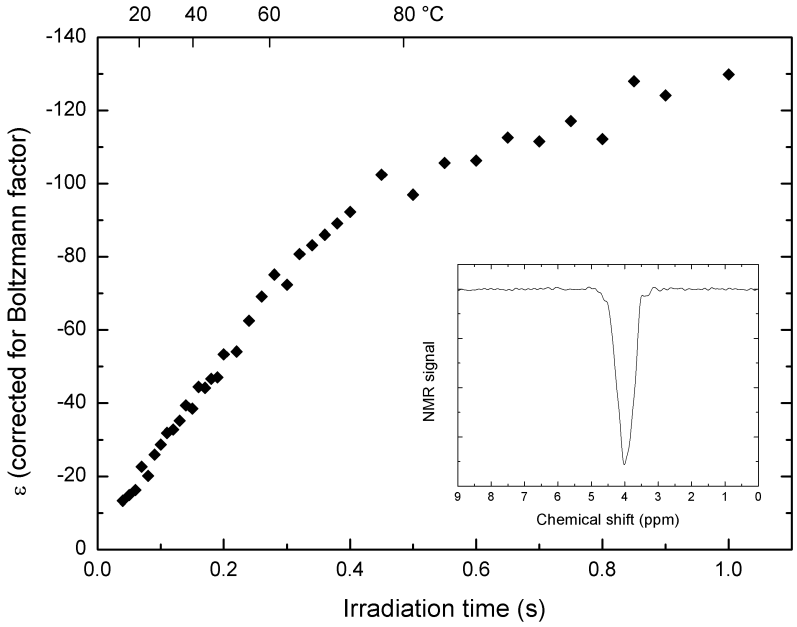

(a) DNP enhancement as a function of microwave irradiation time, for a 2 mm long sample of water doped with 100 mM TEMPOL. The corresponding sample temperature, calculated from chemical shift, is shown on the top x-axis. Inset shows the enhanced spectrum at 88°C where $\varepsilon = -95$ relative to the unenhanced signal at 6°C.

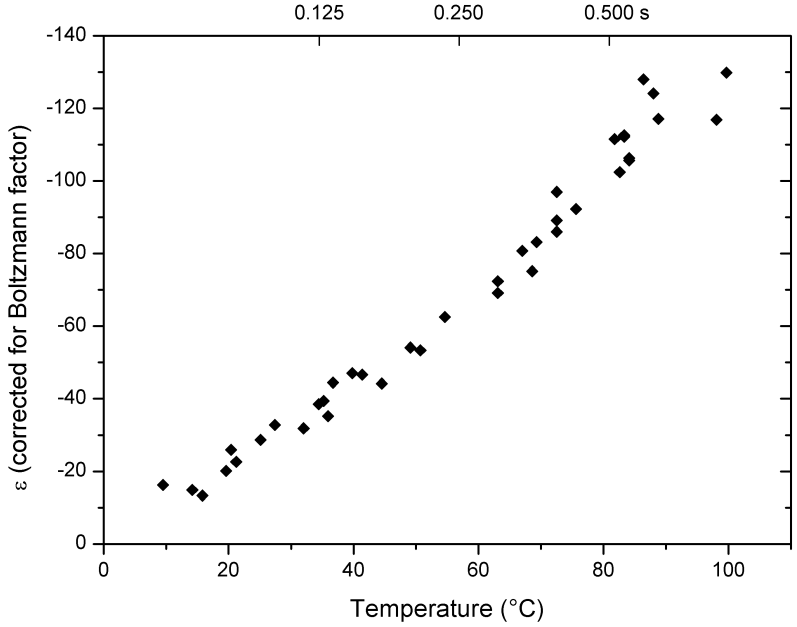

(b) DNP enhancement as a function of temperature, as calculated from the chemical shift. The corresponding irradiation time is shown on the top x-axis.

Figure 5.5: Evolution of nuclear spin polarisation with 1.3 W microwave irradiation. Enhancement values are corrected for the change in Boltzmann factor with temperature increase.

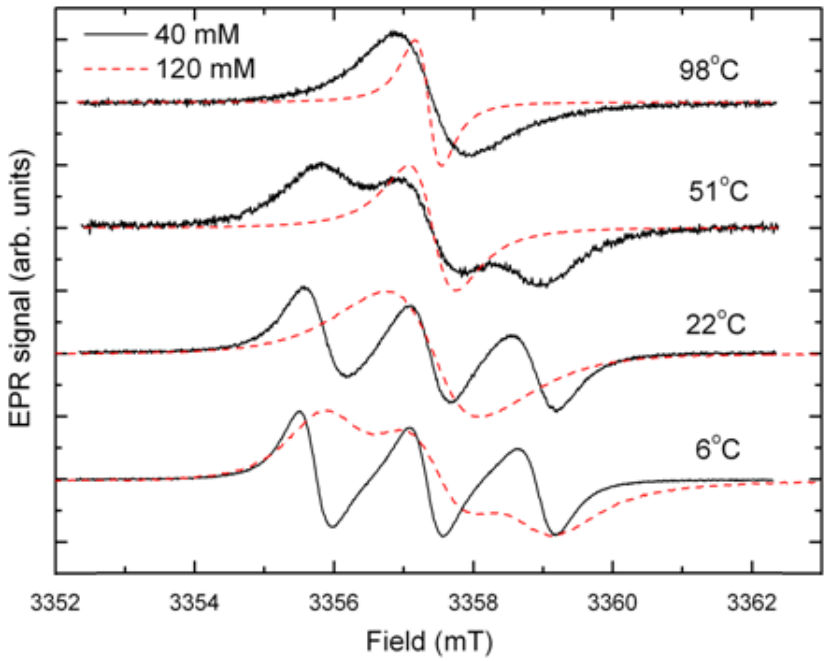

Figure 5.6: CW-EPR spectra of TEMPOL in water recorded at different temperatures, at two radical concentrations.

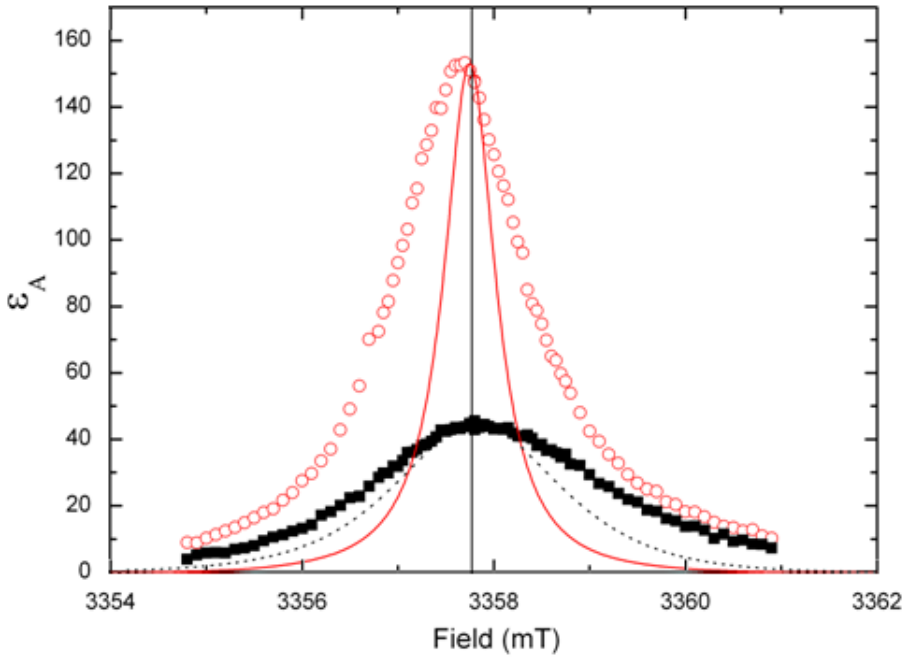

Figure 5.7: DNP enhancement as a function of magnetic field for a sample of water with 120 mM TEMPOL, 10 mm length. 1 s microwave irradiation. Circles — 1.3 W, 130°C; squares — 0.25 W, 40°C. Lines are integrated CW-EPR spectra: solid line — 98°C; dashed line — 22°C.

Figure 5.3) and, therefore, rapidly varying $T_{1\mathrm{I}}$, mean the time and temperature dependence of the enhancement must be modelled simultaneously using Equations 5.3 and 5.4. We define ε with Equation 5.3

$$\varepsilon = \frac{I_{\mathrm{enh}} - I_0}{I_0} \tag{5.3}$$

but calculated with instantaneous values for I_{enh}, rather than the standard Bloch equation solutions, and $T_{1\mathrm{I}}$ (Equation 5.4):

$$\frac{dI_{\mathrm{enh}}}{dt} = \frac{\varepsilon_0(T)I_0(T) - I_{\mathrm{enh}}}{T_{1\mathrm{I}}(T)} \tag{5.4}$$

and with I_0 corrected for the change in Boltzmann factor at different temperatures, e.g. scaled by a factor of 0.75 at 100°C. This adjustment had to be made so that the same reference spectrum at 6°C could be utilised, as recording a new reference for each enhancement measurement by using heated gas would be practically very time-consuming and could possibly also cause changes in the NMR circuit. $T(t)$ and $T_{1\mathrm{I}}(T(t))$ were found from fitting experimental data, and $\varepsilon_0(T)$ was modelled using a phenomenological equation, which is described below.

The dependence of the temperature (measured by chemical shift) on irradiation time for the short 2 mm 100 mM TEMPOL-water sample was found to vary in a similar way as in Figure 5.3, increasing approximately as $T(t) \sim (1-\exp(-t/T_\tau))$, with $\tau = 0.29$ s.

A universal equation for the temperature dependence of the nuclear spin-lattice relaxation time $T_{1\mathrm{I}}$ for samples in the concentration range 10–160 mM was determined from Figure 5.2:

$$T_{1\mathrm{I}}(T) = \frac{160}{1000c}(6.68 + 0.873T(t)) \tag{5.5}$$

$$T_{1\mathrm{I}}(T) = \frac{1}{c}(1.07 + 0.140T(t)) \tag{5.6}$$

where c is the concentration in mM.

The only parameter affecting ε that is expected to vary with temperature is ξ. A fit was performed of ξ data from MD calculations for TEMPOL in water between 25°C and 45°C [40], which revealed a near-linear ($T^{1.07}$) dependence of ξ on temperature. The spread of data in Figure 5.5b seems to show an approximately linear dependence of ε on temperature, so Equation 5.7 was chosen to describe the

change in the equilibrium enhancement with temperature

$$\varepsilon_0(T) = \varepsilon_0(0) + AT \tag{5.7}$$

where A depends only on the radical concentration.

A solution for $\varepsilon(t)$ was found by combining Equations 5.3, 5.4, 5.7 and 5.6 and running time-step calculations with $\Delta t \leq 10^{-3}$ s, fitting to the data in Figure 5.5a; at the same time Equation 5.7 was used to fit the data in Figure 5.5b. A first estimate of the only two variables in the model ($\varepsilon_0(0)$ and A) was given by using a linear fit of ε as a function of T (Figure 5.5b). The optimal values of these variables were restricted to a small range due to the necessity of fitting two data sets (Figures 5.5a and 5.5b) simultaneously. The resulting simulations, constrained almost completely by other experimental data, are shown in Figure 5.8.

In addition to the simulation fit using the experimentally determined $T_{1\mathrm{I}}(T)$ in Figure 5.8a, two further simulations are shown: one taking $T_{1\mathrm{I}}(T)$ to be twice the empirical value, showing a slightly slower build-up of polarisation; and one taking $T_{1\mathrm{I}}(T)$ to be close to zero, showing near-instantaneous transfer of magnetisation. These data show that $T_{1\mathrm{I}}(T)$ is sufficiently fast that the measured ε are close to $\varepsilon_0(T)$ and that the 'true' dependence of $\varepsilon_0(T)$ can be found since $T_{1\mathrm{I}}(T)$ is known. Figure 5.8b shows excellent agreement with the data for the simulation with the correct $T_{1\mathrm{I}}(T)$. The solid line shows a simulation where $T_{1\mathrm{I}}(T)$ is taken to be near zero, i.e. it is the dependence of $\varepsilon_0(T)$ on T. $\varepsilon_0(T)$ is, therefore, the maximum achievable DNP enhancement. It can be seen that at these high concentrations reducing the $T_{1\mathrm{I}}$ would have little effect in increasing the speed of enhancement. For this 100 mM TEMPOL-water sample:

$$\varepsilon_0(T) = (-2 \pm 2) - (1.35 \pm 0.02)T \text{ for } 6^\circ C \leq T \leq 100^\circ C \tag{5.8}$$

Extraction and comparison of coupling factor ξ

The apparent linear dependence of ε on temperature can be understood by examining the parameters f, s and ξ in turn.

From Figure 5.3, it can be seen that samples with different radical concentrations, and hence $T_{1\mathrm{I}}$ times, have approximately the same temperature dependence. Therefore, the relaxation times with and without the radical, the ratio of which f depends on, are expected to have similar temperature dependencies. So f is constant and approximately 1 since $T_{1\mathrm{I,\ doped}} \ll T_{1\mathrm{I,\ pure}}$.

Figure 5.6 shows that at low radical concentrations and temperatures (e.g.

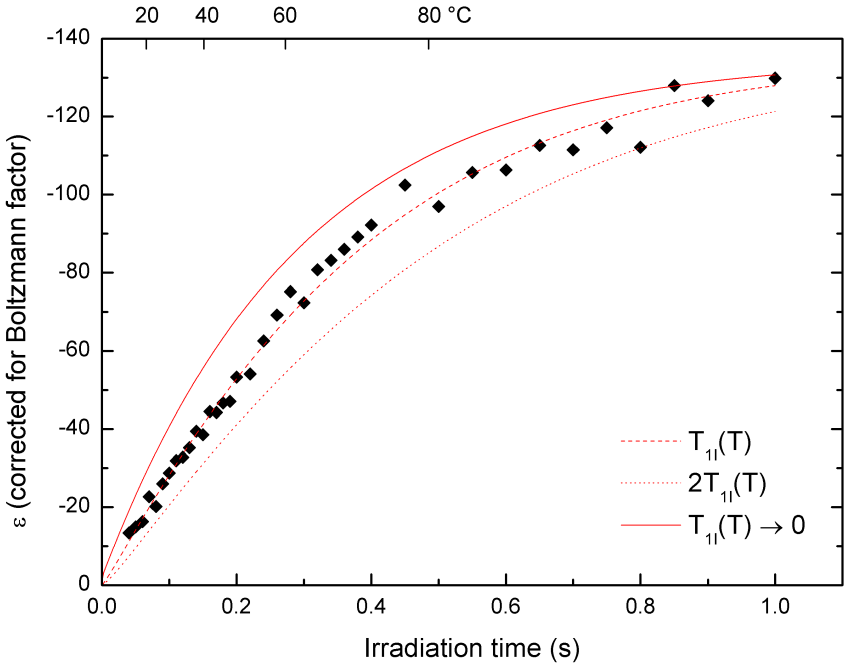

(a) DNP enhancement as a function of microwave irradiation time. Dashed line — fit to data using experimentally determined temperature dependence of $T_{1\mathrm{I}}$ (see Figure 5.2b); dotted line — simulation using $T_{1\mathrm{I}}$ twice experimental value; solid line — simulation using very small $T_{1\mathrm{I}}$ approaching zero, i.e. assuming near-instantaneous polarisation.

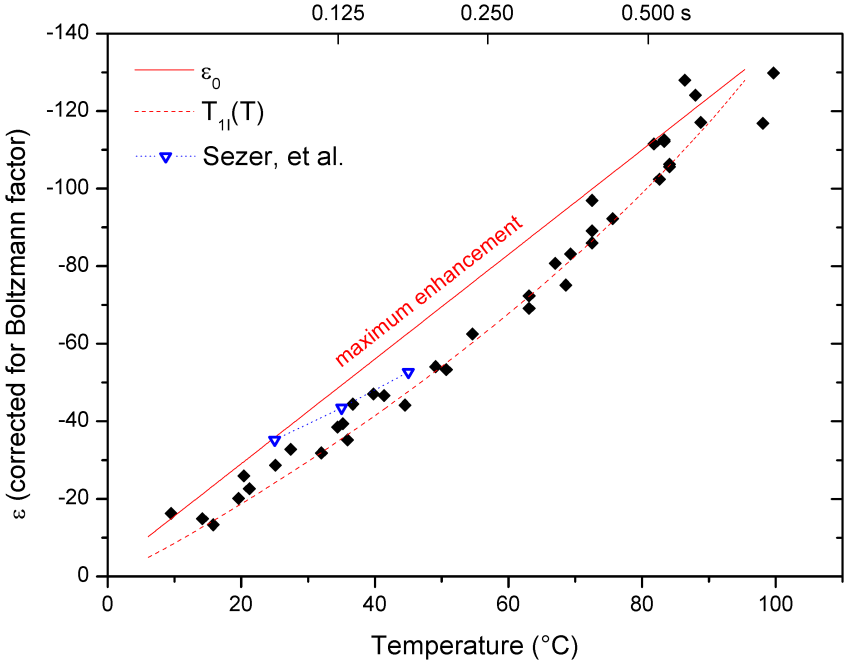

(b) DNP enhancement as a function of temperature. Dashed line — simulation fit to data using experimental $T_{1\mathrm{I}}$; solid line — simulation using very small $T_{1\mathrm{I}}$ approaching zero, i.e. the temperature dependence of ε_0. Calculated enhancement values (assuming $s = f = 1$) from ξ values determined by MD calculations and reported by Sezer et al. [40] are also displayed for comparison.

Figure 5.8: Simulations fitted to experimental data of DNP enhancement in water with 100 mM TEMPOL resulting from 1.3 W microwave irradiation.

Technique	ε_0	ξ	T(°C)	c(mM)	Reference
DNP-NMR	-43^a		~ 40	25	Türke et al. [95]
	-65^a	0.110^b	~ 50	10	Villanueva-Garibay et al. [96]
	-36	0.055	25	100	This thesis
	-49	0.076	35	100	This thesis
	-63	0.096	45	100	This thesis
	-76	0.117	55	100	This thesis
NMRD^c	$-41/29^d$	0.07/0.05	25		Bennati et al. [121]
	$-65/53^d$	0.11/0.09	35		Bennati et al. [121]
	$-83/65^d$	0.14/0.11	45		Bennati et al. [121]
	$-95/83^d$	0.16/0.14	55		Bennati et al. [121]
MD		0.0534	25		Sezer et al. [40]
		0.0660	35		Sezer et al. [40]
		0.0800	45		Sezer et al. [40]

[a] Not corrected for Boltzmann factor since temperature is uncertain, but believed to not exceed ~ 25°C.
[b] Calculated from Reference [96] data assuming $s = 1$ and $f = 0.90$.
[c] Values are with/without the inclusion of a contact contribution to the relaxation profile.
[d] Calculated assuming $s = 1$ and $f = 0.91$ [40].

Table 5.1: Summary of DNP enhancements and coupling factor data for several studies conducted at 3.4 T

40 mM and 6°C), the ^{14}N hyperfine splitting is well resolved, thus making complete saturation difficult, thereby reducing the attainable ε. As the temperature increases, fast exchange between radical molecules broadens the lines until they eventually collapse into a single peak, thus increasing the attainable s and therefore ε from this temperature change alone. However, at high radical concentrations, the lines strongly overlap even at 6°C and $s \approx 1$ is possible at all of the temperatures studied and it is not expected to show a significant temperature dependence. In addition, Figure 5.4 shows that the microwave power is sufficient to maintain $s \approx 1$, even when the exchange is very fast and T_{1S} is short, because a decrease in ε_A would otherwise be observed in the highest concentrations at the highest temperatures.

The temperature dependence of ε is therefore dominated by that of ξ at high concentrations, microwave powers and temperatures. As the temperature rises and the water molecules move more rapidly, the correlation time that determines T_{1I} shortens. Similarly, ξ depends on solvent-radical interaction correlation times that are comparable to ω_S^{-1} and these cause an approximately linear dependence over small ranges of temperature in an analogous way to those affecting T_{1I} (Figure 5.2b).

Estimated values of the coupling factor, ξ, were calculated for a range of

temperatures using Equations 5.1 and 5.8. These values are presented in Table 5.1 for comparison with results from other groups at 3.4 T.

Villanueva-Garibay et al. [96] used a novel double-resonance structure to study DNP in water with 10 mM TEMPO. Due to the small active region of their structure, they found that the enhancement was dependent on sample size — much like the work presented in this chapter. For a sample of comparable length to their maximum B_{1S} region (2.4 mm) they found $\varepsilon = -65$, although they suggested that a non-uniform B_{1S} over the sample resulted in a smaller value. This ε value was used to calculate the coupling factor in Table 5.1 assuming that f is the same for TEMPO and TEMPOL. The ε value suggests that their sample temperature reached at least 55°C if these assumptions are correct. However, a comparison of the EPR spectrum for their 10 mM sample with the 40 mM sample presented in Figure 5.6 suggests that s for their sample could rise rapidly with such temperature increases which makes the interpretation more uncertain. Their EPR data also indicates that s is likely to be less than 1, and so ξ and therefore T must be larger. It is this lack of knowledge of s with temperature that was the main reason for being unable to accurately simulate the longer sample data for $c \ll 100$ mM in this work.

Bennati et al. [121] calculated ξ values from correlation times at different temperatures for a 25 mM ^{15}N-^{2}H-TEMPONE solution using NMRD. These coupling factors were then used to estimate DNP enhancements. The coupling factor without any contact contribution at 25°C is close to the corresponding value found in this thesis, however, they find a more rapid variation with temperature than observed here, with ξ doubling with a ∼20°C temperature rise.

Türke et al. [95] measured an enhancement of $\varepsilon = -43$ for a water sample with 25 mM TEMPONE-D, ^{15}N and used NMRD results to calculate an experimental saturation factor $s = 0.65$. The use of the ^{15}N isotope of the radical should improve the achievable saturation, but the estimate of $s = 0.65$ agrees with the results here suggesting that such low radical concentrations are insufficient to allow fast enough electron spin exchange to enable $s \approx 1$ to be approached near room temperature. The analysis was complicated further by a largely uncertain estimated temperature rise of 15°C.

Sezer et al. have obtained values of ξ via MD simulations and density matrix calculations, for TEMPOL in water at magnetic fields from 0.34 T to 12.8 T at a range of temperatures [40, 125]. Their values for 3.4 T at agree well with the experimentally determined values here at 25°C, but do not increase as rapidly with temperature as the data in this chapter. For example, increasing the temperature from 25° to 45°C gives an experimental increase in ξ of ∼75% and a calculated

increase of ∼50%. Sezer et al. used a non-polarisable molecular dynamic water model and had to slow down the dynamics by adjusting the friction coefficient of the thermostat to match experimental and theoretical diffusion coefficients so they agree at 25°C. This added friction may have reduced the temperature dependence of the dynamics in the model, providing a possible explanation of the disparity between the coupling factor values at temperatures above 25°C.

It was not feasible to accurately simulate ε as a function of irradiation time for the large samples due to non-uniform irradiation and heating, as well as the fact that s likely has a strong dependence on T at lower concentrations. However, it is interesting to note that the DNP-enhanced spectrum in Figure 5.1 shows an enhancement of $\varepsilon \approx -182$ at 133°C (when the Boltzmann factor is included) and extrapolation of Equation 5.8 to the same temperature predicts an identical value. Now as discussed, there is clearly considerable uncertainty in the precise enhancement value of this long sample, but this agreement does nevertheless provide added confidence in the robustness of the general approach taken to the analysis and also suggests that ε continues to increase approximately linearly with T at higher temperatures.

5.4 Conclusions

This chapter has demonstrated a method for determining the temperature dependence of the maximum enhancement for a nitroxide radical in water at high magnetic field.

At low concentrations (∼10 mM), CW-EPR spectra displayed resolved hyperfine splitting and reaching complete saturation is therefore much more problematic. Also, s can be temperature dependent and difficult to ascertain. Using high concentrations (∼100 mM) results in some broadening of the resonance, but this is relatively small (∼16 Hz at 40°C) and much smaller at higher temperature. The high radical concentrations used also mean $f \approx 1$, and provided sufficient microwave power is used, $s \approx 1$ also. This leads to a situation where ε is just the product of the ratio of the electron and nuclear gyromagnetic ratios (γ_S/γ_I) with the coupling factor ξ. Therefore, ξ can be deduced from experiment.

In order for this method to be utilised, $T_{1\mathrm{I}}$ must be known and the temperature must be measurable during detection of the DNP spectrum by chemical shift. Furthermore, short samples should be used for proper analysis so the temperature and enhancement gradients in the sample can be minimised. The high microwave power required to ensure $s \approx 1$ when fast exchange between the radical electrons is

present causes rapid sample heating at these high EPR frequencies. However, the maximum DNP enhancement can still be obtained if $T_{1\mathrm{I}} \ll \tau_T$ (the characteristic heating time).

Since the data presented here uses temperature increases caused by microwave power, the thermal equilibrium reference NMR spectrum is measured at a different temperature to the enhanced spectra (i.e. 6°C), and so the difference in the Boltzmann distributions must be taken into account in order to correctly calculate ε and ξ. The experimentally determined values of ξ were compared with MD calculations and agree well at room temperature, but they increase more rapidly with increasing temperature than predicted by theory.

DNP enhancements >100 were achieved at high temperatures, giving a high sensitivity in these experiments. It has also been shown that, for temperature sensitive samples, the microwave power and irradiation time could be adjusted to maintain a more suitable temperature, whilst still obtaining reasonable enhancements (e.g. at 250 mW, $\varepsilon \sim -40$ at 40°C). Also, the short polarisation times mean that rapid acquisition can be used providing further signal enhancement, so it seems likely there would be sufficient sensitivity to allow useful liquid-state DNP-NMR experiments on small samples.

Chapter 6

Overhauser DNP of small organic compounds in aqueous solutions

There has been a revival of interest in liquid-state DNP in recent years, stimulated in large part by the development of the dissolution method proposed by Ardenkjaer-Larsen et al. [89], and also by the larger than expected enhancements obtained at high fields using methods where both polarisation and detection are completed in the liquid-state. With the advent of commercially available microwave sources at intermediate to high NMR magnetic fields, the last decade has seen many studies investigating the Overhauser-type DNP mechanism in liquids at fields previously unattainable (for example, see References [113], [97], [43] and [36]).

However, the vast majority of liquid DNP work has focused on the hyperpolarisation of solvent nuclei and not on solutes because of the challenges raised by low NMR coil filling factors and the necessity for small sample volumes at high microwave frequencies. There have been encouraging results in shuttle DNP, where enhancements have been observed and coupling factors determined for dissolved biomolecules such as glucose, DSS and L-tryptophan; though the sensitivity increases reported so far are somewhat small (ε up to $\sim$4) [137, 108]. This method of DNP has an advantage over dissolution in that there is no need to freeze the sample; instead it can be dissolved in biologically-friendly solvents (e.g. water) and experiments conducted at near room temperature where the substance under study remains stable. However, this is technically very challenging and there can be large losses of polarisation during the shuttling process.

Surface and internal water dynamics often play an important role in biological

systems. This has allowed liquid DNP studies of numerous biological systems (e.g. lipid vesicles [138], soluble and membrane proteins [38, 139, 140], and lipid solvent dynamics [141]) by polarisation of solvent water molecules at 0.35 T. Often, the dynamics of water polarised by (and therefore near to) labelled sites on molecules are studied. This is, however, still based on polarising solvents. Furthermore, this work was all carried out at low field.

Krummenacker, et al. [98] recently reported the first ^{1}H DNP experiments where nuclei in molecules dissolved in solution have been enhanced at high field. Metabolites were studied at 9.2 T and coupling factor ratios were measured. Exploring the differences in the coupling of radicals to the nuclei on solvent molecules and to those on target solute molecules is important to understand polarisation transfer in Overhauser DNP, and to gain insights into the possible applications of the technique in fields such as molecular biology.

The results of liquid-state ^{1}H DNP experiments on small organic molecules dissolved in water are presented in this chapter, further demonstrating the potential applicability of liquid DNP at moderately high field. The compounds glycine, L-proline and acrylic acid in aqueous solution will each be considered in turn, followed by some overall conclusions.

6.1 Glycine

The smallest of the amino acids, glycine has a molar mass of 75.07 g mol^{-1}. This compound was chosen for its small and simple structure, as well as its high water solubility which is necessary to facilitate easier observation of the ^{1}H NMR signal from the CH_2 group of glycine. In a 3 M glycine solution, the concentration of the CH_2 protons is only 6 mol/l; the concentration of water protons on the other hand is 111 mol/l. So the ^{1}H NMR signal from the CH_2 group will be less than 6% of that from the solvent, illustrating the challenging nature of such experiments even with highly soluble samples. In addition to the size of the CH_2 proton signal being observable, there is also sufficient separation from the water proton signal to be resolved on the 143 MHz/94 GHz system described in Chapter 4. The structure of glycine is given in Figure 6.1.

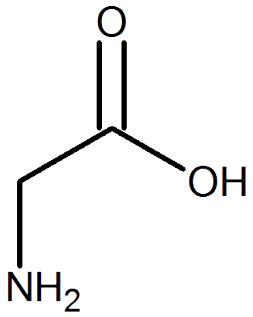

Figure 6.1: Skeletal formula of glycine (NH_2CH_2COOH).

6.1.1 Experimental details

Sample preparation

A solution of 100 mM TEMPOL dissolved in D_2O was made up first. Glycine was then dissolved in the solution to a concentration of 3 M. This concentration approaches the maximum possible, as the water solubility of glycine is given in the literature as 25.0 g/100 ml (equivalent to approximately 3.3 M concentration) [142]. The sample was not degassed because of the technically demanding nature of the standard freeze-pump-thaw process when dealing with such short and thin capillary tubes. In particular, sealing the capillaries without evaporating sample and leaving air bubbles was found to be impractical.

An 11 mm long sample of the solution was sealed in quartz capillaries using epoxy resin according to the method described in Section 4.2.

Experiment

In contrast to the experimental method used for one-pulse DNP-NMR experiments in Chapter 5, variable microwave pulse lengths were not used here; instead, continuous-wave irradiation was applied. The microwaves were used to heat and maintain the temperature of the sample at an approximately constant value. As can be seen in Figure 5.3 of Chapter 5, the sample temperature of water samples rises quickly irrespective of radical concentration (with a characteristic time of $\tau_T = 0.25$ s) and after about 1 s of irradiation, begins to plateau. The typical experiment times of the work presented throughout this chapter are at least several minutes (up to several hours), so the sample temperature is assumed to be constant for >99% of the duration of the experiment.

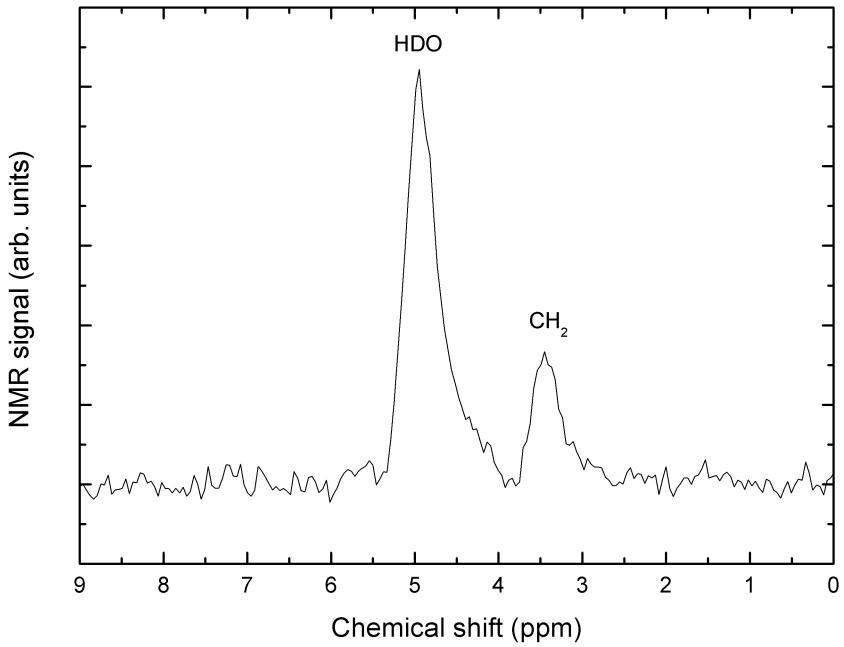

Figure 6.2: ^{1}H NMR spectrum of 3 M glycine-100 mM TEMPOL-D_2O sample: no microwave irradiation, 40,000 acquisitions, 7.0 ± 0.5°C.

6.1.2 Results and discussion

The thermal equilibrium reference ^{1}H NMR spectrum is shown in Figure 6.2. Due to the low signal-to-noise ratio of the proton resonance from the CH_2 group in glycine, the spectrum was acquired over several hours whilst the temperature was maintained at 7°C using nitrogen gas flow. Using D_2O as the solvent causes the exchange of all OH and NH protons in the sample molecule with deuterium [143]. The primary amine (NH_2) group protons also exchange with deuterium. Therefore, all those protons give a common singlet at the chemical shift of the water protons, leaving only two observable peaks for the HDO 'water' molecules and the CH_2 group. The intensity of the HDO peak is much greater than the CH_2 peak due to the higher concentration of D_2O molecules and readily exchangeable OH and NH_2 protons.

A DNP-enhanced spectrum is shown in Figure 6.3. Negative enhancement is observed due to the dipolar coupling dominated Overhauser effect in aqueous solutions [6]. It is immediately apparent that the HDO protons have been polarised more than the CH_2 protons. The resolution is sufficient for the sample temperature to be determined from the temperature dependent chemical shift of water. However, at the high temperatures attained with high applied microwave powers, the HDO peak begins to merge with the CH_2 and the integrated signal intensity becomes more

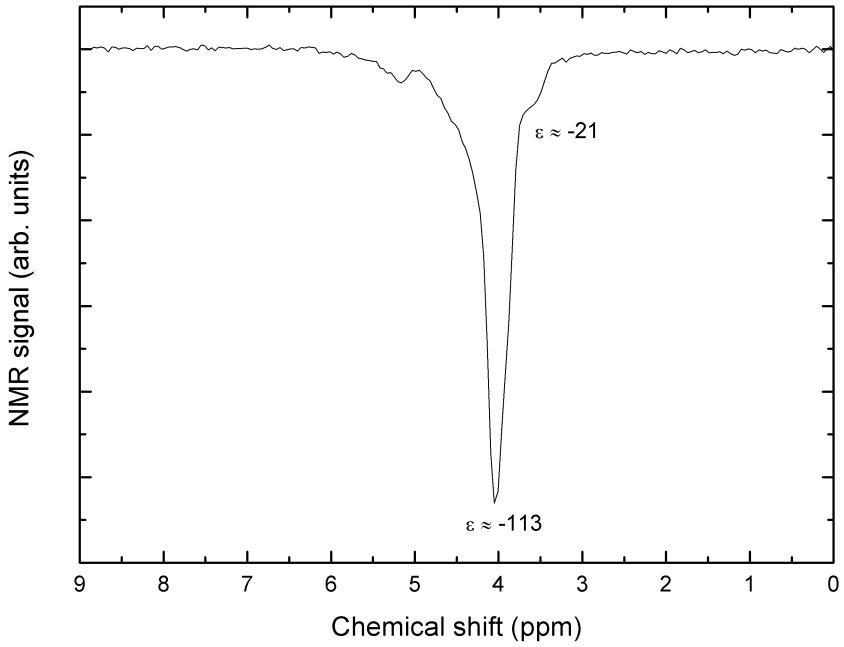

Figure 6.3: DNP-enhanced ^{1}H NMR spectrum of 3 M glycine-100 mM TEMPOL-D_2O. ∼1.1 W applied microwave power, 400 acquisitions, 101 ± 3°C.

uncertain. Figure 6.3 also shows that an anomalous peak becomes visible at 5.2 ppm as the HDO peak shifts upfield with increasing temperature. This chemical shift appears to be consistent with a primary amine group [144], and although it is not normally observed, it may be caused by residual protons in the NH_2 group of glycine that have not fully exchanged with deuterium. As in Figure 5.1 (DNP spectrum of water with 120 mM TEMPOL), there is a low intensity broad component to the HDO peak which is likely a reflection of uneven sample temperatures. Unless otherwise stated, Gaussian peaks were fitted to the spectra and the enhancement results were calculated using Equation 6.1:

$$\varepsilon = \frac{I_{\text{enh}} - I_0}{I_0} \tag{6.1}$$

where I_{enh} and I_0 are the integrated intensities of the enhanced and thermal equilibrium NMR spectra, respectively.

Figure 6.4 shows the DNP-enhanced ^{1}H NMR spectra acquired over a range of temperatures, showing the gradual coalescence of the two peaks as the temperature rises with increasing microwave power. The increase in enhancement of the HDO and CH_2 protons can be clearly seen and, as expected, the shift of the CH_2 protons remains constant to within experimental error. The anomalous peak at

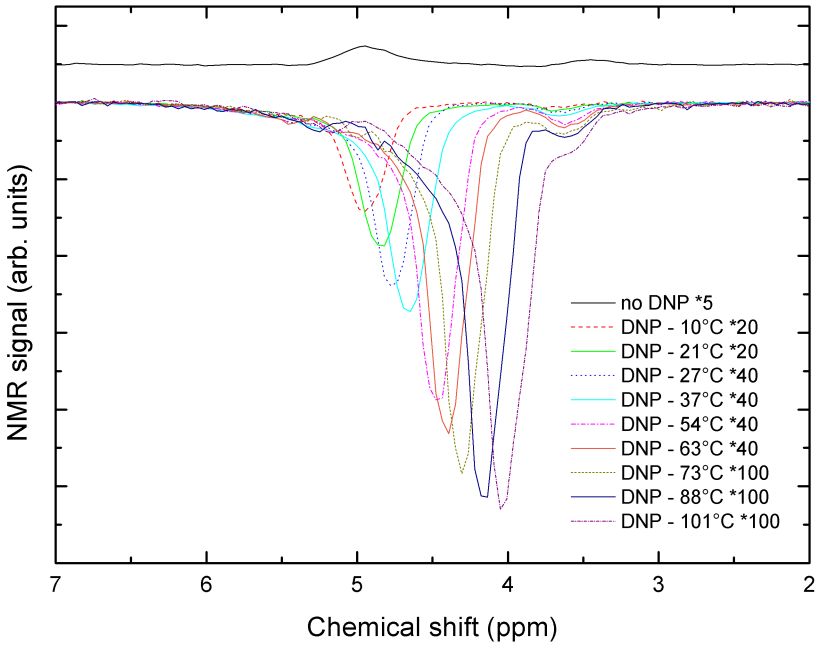

Figure 6.4: Overlay of DNP-enhanced spectra, illustrating the increasing enhancement and temperature of both HDO and CH_2 protons. The DNP spectra have been normalised to the same number of acquisitions (multiplication factor shown in figure) and the thermal equilibrium signal increased by a factor of 5 for comparison.

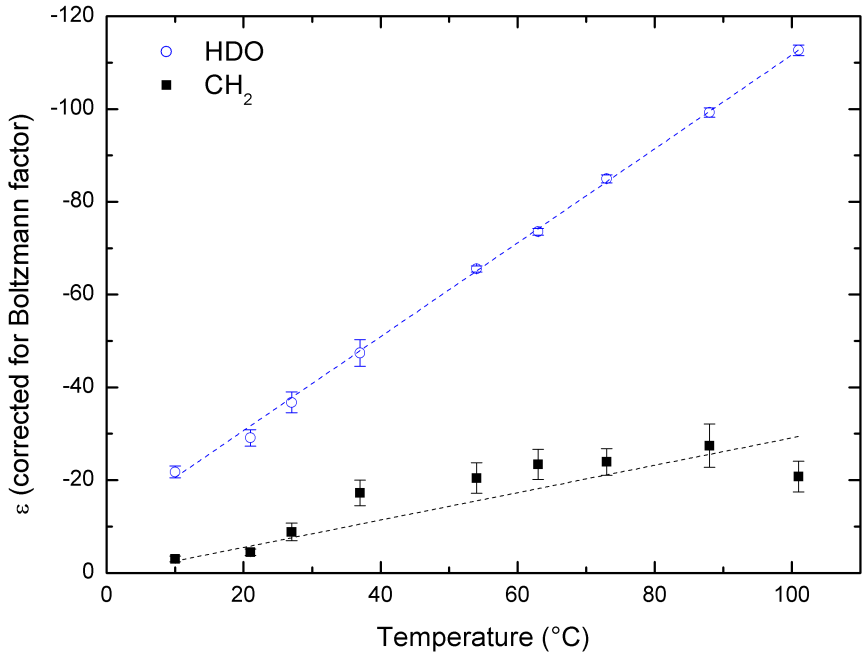

Figure 6.5: DNP enhancement as a function of temperature, as calculated from the chemical shift. Dashed lines — linear fits with slopes of -1.01 and -0.30 for HDO and CH_2 protons, respectively. Ratio of slopes $m_{\mathrm{HDO}}/m_{\mathrm{CH_2}} = 3.4 \pm 0.5$.

5.2 ppm is not visible at lower microwave powers, which suggests that perhaps the HDO enhancement has been slightly overestimated at lower temperatures. Given the difference in signal intensities, however, this effect is estimated to be small (<10%).

Sample stability — CW-EPR signal intensity measurements

A series of room temperature CW-EPR experiments were carried out at X-band in collaboration with William Woodruff. The signal intensity was monitored periodically over 46 days and found to be stable to within experimental uncertainty. Therefore, there appears to be little or no degradation of the TEMPOL radical in the sample over experimentally relevant timescales and the concentration is assumed to be ∼100 mM throughout the duration of the DNP experiments conducted.

Temperature dependence of enhancement of HDO and CH_2 protons

The temperature dependence of ε was measured and found to vary approximately linearly for both the HDO and CH_2 protons over the temperature range studied (see Figure 6.5). The enhancements were calculated using Equation 6.1 and I_0 values that take into account the change in Boltzmann factor with increasing temperature.

As with the water-TEMPOL samples presented in Chapter 5, temperatures >100°C were achieved in the sealed sample tube, with maximum observed values of $\varepsilon_{\mathrm{HDO}} \approx -113$ at 101°C and $\varepsilon_{\mathrm{CH_2}} \approx -27$ at 88°C.

It is demonstrated that significant enhancements of both solvent and solute protons, $\varepsilon_{\mathrm{HDO}} \approx -50$ and $\varepsilon_{\mathrm{CH_2}} \approx -12$, respectively, can be achieved at a temperature of ∼40°C (closer to the real temperatures where many biological process occur). Krummenacker, et al. [98] recently showed that this solute enhancement is a result of direct coupling of the radical electron spin to the protons on the target molecule and not mediated via the solvent protons. The enhancement values reported here are inevitably underestimates of the 'true' enhancements as the long sample used results in an average signal of enhanced and non-enhanced protons in the sample. This could account for the lower maximum observed integrated enhancement of water protons $\varepsilon \approx -113$ at ∼100°C compared with the maximum observed for a short 2 mm water-100 mM TEMPOL sample where $\varepsilon \approx -130$ at ∼100°C (Chapter 5, Figure 5.5b).

At the highest measured temperature (101°C), $\varepsilon_{\mathrm{CH_2}}$ is seen to decrease appreciably. It is unlikely that this observation is due to any instabilities of the glycine molecule at high temperatures as it does not usually begin to decompose until well above 200°C [145]. It is possible that the apparent drop in enhancement is simply due to experimental error. Unfortunately, further investigation to higher temperatures would probably prove difficult with the current setup due to the likelihood of seal failure and the subsequent evaporation of the sample.

The ratio of the slopes in Figure 6.5, and hence the average ratio of enhancements $\varepsilon_{\mathrm{HDO}}/\varepsilon_{\mathrm{CH_2}}$, is 3.4. This suggests ∼3–4 times weaker coupling of the radical electron spin to the dissolved molecule protons than to the solvent protons, if the leakage factor of both protons were approximately the same (≈ 1). If the highest temperature CH_2 data point is discarded as an anomalous result, the ratio would be $\varepsilon_{\mathrm{HDO}}/\varepsilon_{\mathrm{CH_2}} = 2.9$.

Measurement of T_1 by saturation-recovery

The temperature dependence of $T_{1\mathrm{I}}$ is shown in Figure 6.7, with the results of one of the saturation-recovery experiments shown in Figure 6.6, indicating the spread of the data and the quality of the fit. The spectra were acquired using DNP and the sample temperature variation resulting from the CW microwave irradiation was measured using the change in the chemical shift of water. The difficulty in obtaining a large number of spectra with acceptable signal-to-noise, as well as the potential for evaporating the sample if heated for long periods of time, meant that only a few data

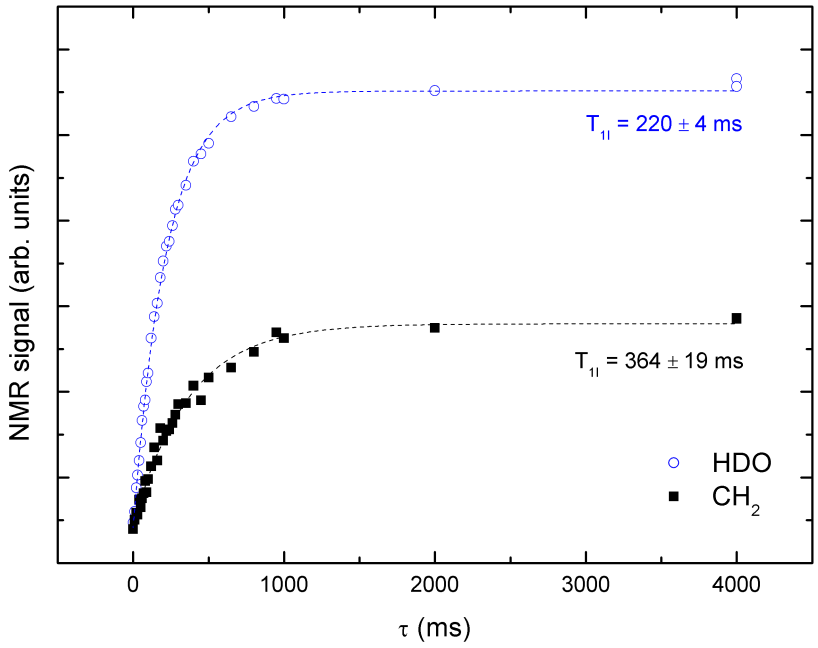

Figure 6.6: Saturation-recovery experiment at 143 MHz. Sample temperature is 100 ± 3°C. Dashed lines — fit of the form $(1 - \exp(-t/T_{1I}))$ with resulting nuclear relaxation times displayed in the figure.

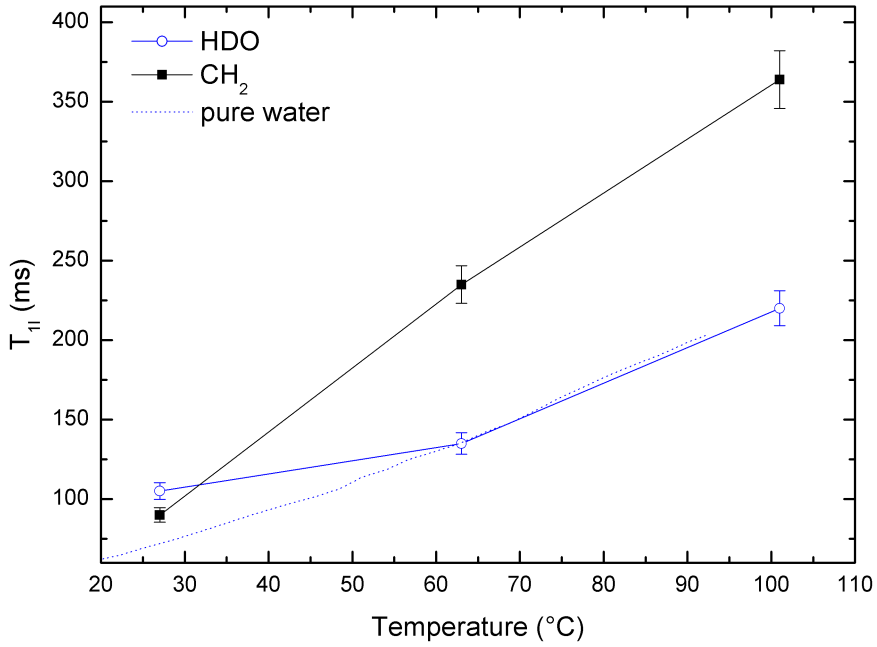

Figure 6.7: Temperature dependence of proton T_1 of HDO and CH_2 in water with 3 M glycine and 100 mM TEMPOL at 143 MHz. Data are shown with temperature indicated by chemical shift. The T_1 of pure water is shown as a dotted line and has been scaled to agree with the glycine-TEMPOL-D_2O sample value at 63°C.

points on the T_{1I} vs. temperature graph could be taken. The lack of data prevents any detailed quantitative analysis of the behaviour, but the fractional change in T_{1I} does appear similar to that of pure water, especially at higher temperatures — plotted as a dotted line and scaled to agree at 63°C in Figure 6.7.

The T_{1I} of water is a measure of its mobility, which is a function of a number of factors including the solution viscosity, temperature and the extent of hydrogen bonding. The additional presence of a solute such as glycine to water results in regions of greater order due to stronger hydrogen bonding and the formation of solvation shells around the solute molecule. This results in the reduced mobility of the water molecule and ultimately lowers the average T_{1I} measured. Thus, this effect contributes to the lowering of the nuclear spin-lattice relaxation time compared to pure water. However, its contribution is quite small — causing a less than 0.3 s (10%) difference in $T_{1I,\,H_2O}$ for glycine-water and pure water at 300 MHz [146] — and is considered negligible in comparison to the effect of the paramagnetic TEMPOL.

Coupling factor ξ — an estimation

When comparing the results for the two different proton types studied here (HDO and CH_2), it is important to consider what affects the enhancement: γ_S, γ_I, s, f and ξ. The gyromagnetic ratios are identical, and since the saturation factor s describes a property of the radical it must be the same for all enhanced nuclei in the sample under study. Of the two remaining factors f and ξ, which vary according to the environments of the protons, f can be straightforwardly measured by comparing the intrinsic nuclear relaxation time of the sample (i.e. without radical) to the time with the radical present.

A non-doped sample of 3 M glycine in D_2O was made up so that T_{1I0} could be measured. However, without the radical and the Overhauser enhancement, T_1 measurements on the 143 MHz/94 GHz system proved problematic due to weak NMR signal and poor resolution as well as prohibitively long relaxation times (∼several seconds). Instead, ∼5 mm of sample was syringed into a 2.0/2.4 mm ID/OD quartz capillary which was sealed (flame-sealed on one end, glued with epoxy resin on the other) and inserted into a Bruker 4 mm rotor. Inversion-recovery experiments were then carried out on a 100 MHz Chemagnetics Infinity NMR spectrometer and a 300 MHz Varian InfinityPlus Spectrometer. The resulting spin-lattice relaxation times are presented as a function of ^{1}H NMR frequency in Figure 6.8. Assuming a linear frequency dependence of T_{1I} over the relatively small frequency range, interpolation was used to calculate relaxation times $T_{1I0,\,HDO} = 6.5$ s and $T_{1I0,\,CH_2} = 2.2$ s at 143 MHz at room temperature (approximately 20°C).

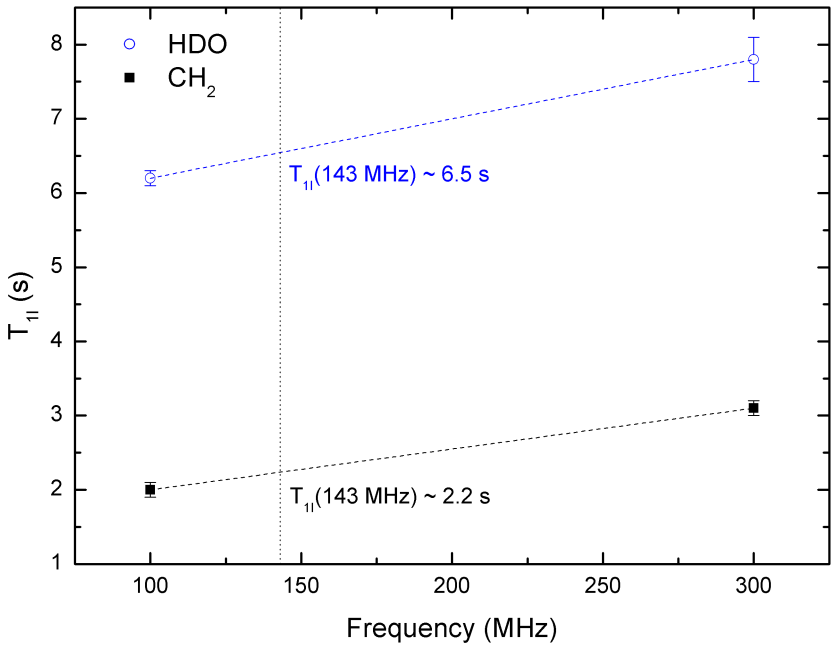

Figure 6.8: Room temperature $T_{1\mathrm{I}}$ values of 3 M glycine-D_2O at 143 MHz, interpolated from measurements made at 100 MHz and 300 MHz.

Unfortunately, no ε or $T_{1\mathrm{I}}$ data were taken at exactly 20°C, with the closest values being at 27°C. However, inspection of the equation for the leakage factor f (Equation 6.2), shows that an estimate of its lower limit at 27°C can be made since the $T_{1\mathrm{I}}$ of pure water at 27°C will be greater than at 20°C giving an f value closer to 1. Hence, this lower limit was calculated to be $f_{\mathrm{HDO}} \geq 0.98$ and $f_{\mathrm{CH_2}} \geq 0.96$ using the following equation:

$$f = 1 - \frac{T_{1\mathrm{I}}}{T_{1\mathrm{I}0}} \tag{6.2}$$

where $T_{1\mathrm{I}}$ and $T_{1\mathrm{I}0}$ is the nuclear spin-lattice relaxation time with and without the radical present, respectively.

Complete saturation when using nitroxide polarising agents such as TEMPOL can be difficult to achieve due to the size of the nitrogen hyperfine coupling and also the short electron relaxation times $T_{1\mathrm{S}}$ in liquids. Saturation has also proved challenging to quantify, though there has been some success reported in the literature, using for example pulsed ELDOR. However, at 94 GHz this is still limited and measurements at radical concentrations $\geq$25 mM have not been possible due to the fast, unobservable decay of EPR FIDs for nitroxides such as TEMPO [95]. Nevertheless, it is possible to approach full saturation if high radical concentrations and microwave power are used. Therefore, for the following analysis the common

assumption that $s \approx 1$ will be made, which is supported by recent calculations using Redfield theory at 94 GHz [133].

Assuming $s \approx 1$, and using $\varepsilon_{\mathrm{HDO}} = -36.8$ and $\varepsilon_{\mathrm{CH_2}} = -8.8$ from Figure 6.5, an estimate of the coupling factor at 27°C can be calculated as $\xi_{\mathrm{HDO}} = 0.057 \pm 0.007$ and $\xi_{\mathrm{CH_2}} = 0.014 \pm 0.003$. $\xi_{\mathrm{HDO}} \approx 0.057$ agrees well with coupling factor of $\xi_{\mathrm{H_2O}} = 0.055 \pm 0.003$ found in Chapter 5 of this thesis (cf. Table 5.1), and with the value found by MD calculations ($\xi = 0.0534$ at 25°C) [40]. The leakage and coupling factor values are summarised later in the chapter in Table 6.1 (Section 6.3.2).

Since the difference between the DNP enhancement of solvent and solute protons is of great interest, it may be more instructive to evaluate the ratio of the coupling factors. This quantity also has the advantage of being independent of the hard to measure saturation factor. Now, the coupling factor can be expressed as

$$\xi_{\mathrm{p}} = \frac{\gamma_{\mathrm{I}}}{\gamma_{\mathrm{S}}} \frac{\varepsilon}{f_{\mathrm{p}} s} \tag{6.3}$$

where the subscript p denotes a type of proton. Taking the ratio of coupling factors for HDO and CH_2, s is clearly seen to be eliminated from the equation:

$$\frac{\xi_{\mathrm{HDO}}}{\xi_{\mathrm{CH_2}}} = \frac{\varepsilon_{\mathrm{HDO}} f_{\mathrm{CH_2}}}{\varepsilon_{\mathrm{CH_2}} f_{\mathrm{HDO}}} \tag{6.4}$$

This coupling factor ratio can be theoretically predicted in the manner recently employed by Krummenacker, et al. [98] in their study of metabolites, where a force-free hard-sphere (FFHS) model was assumed. A similar procedure is followed below in the concluding parts of this section.

Before continuing the analysis, it is worth noting that Sezer [42] has recently proposed a novel method for quantifying Overhauser effect DNP data and calculating coupling constants using a combination of MD simulations to treat solvent molecules close to the radical and analytical calculations (FFHS model) to determine the solvent-radical dynamics at larger distances. He recognised that a simple FFHS model has its limitations, but for studies involving small radicals and target molecules like those involved here, reasonable results may still be obtained.

In the aforementioned FFHS model, the correlation time is related to the distance of closest approach d of the electron and nuclear spins, and their diffusion coefficients [6, 147]:

$$\tau = \frac{d^2}{D_{\mathrm{S}} + D_{\mathrm{I}}} \tag{6.5}$$

where D_{S} and D_{I} are the diffusion coefficients of the electron and nuclear spin, respectively.

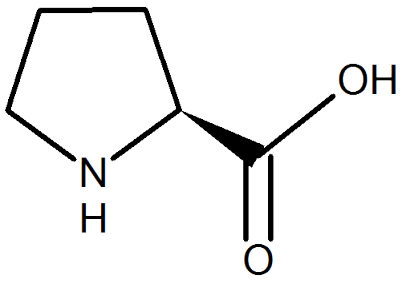

Figure 6.9: Skeletal formula of L-proline ($C_5H_9NO_2$).

The coupling factor is known to decay with the correlation time as $\tau^{-3/2}$ [40]. So assuming the distance of closest approach is the same for both types of protons, the ratio of coupling factors can be predicted from the relevant diffusion constants:

$$\frac{\xi_{\mathrm{HDO}}}{\xi_{\mathrm{CH_2}}} = \left(\frac{\tau_{\mathrm{HDO}}}{\tau_{\mathrm{CH_2}}}\right)^{-3/2} = \left(\frac{D_{\mathrm{S}} + D_{\mathrm{HDO}}}{D_{\mathrm{S}} + D_{\mathrm{CH_2}}}\right)^{3/2} \tag{6.6}$$

using $D_{\mathrm{HDO}} = D_{\mathrm{H_2O}} = 2.3 \times 10^{-9}$ $\mathrm{m^2 s^{-1}}$ [148]; $D_{\mathrm{CH_2}} = 0.75 \times 10^{-9}$ $\mathrm{m^2 s^{-1}}$ [149]; and assuming the diffusion coefficient for TEMPOL is the same as for 4-oxo-TEMPO, $D_{\mathrm{S}} = 0.41 \times 10^{-}9$ $\mathrm{m^2 s^{-1}}$ [38]. A coupling factor ratio is then calculated to be $\xi_{\mathrm{HDO,\ calc}}/\xi_{\mathrm{CH_2,\ calc}} = 3.6 \pm 0.2$.

The measured ratio $\xi_{\mathrm{HDO}}/\xi_{\mathrm{CH_2}} = 4.1 \pm 0.8$. This appears to be in reasonable agreement with the predicted value, but perhaps indicating slightly weaker coupling to the glycine CH_2 group.

6.2 L-proline

L-proline is a protein-forming amino acid, the 'left-handed' enantiomer of proline. It has a molar mass of 115.13 g $\mathrm{mol^{-1}}$, approximately 1.5 times more massive than glycine and acrylic acid. L-proline is small, has a relatively simple ^{1}H NMR spectrum with signals sufficiently separated from the water signal in order to be resolved, and is very soluble in water. However, even at a high concentration of 1 M L-proline dissolved in water, the proton concentrations of water, the C-CH_2-N group, C-CH_2-C groups, and the CH group are 111 mol/l, 2 mol/l, 4 mol/l and 1 mol/l, respectively. The structure of L-proline is shown in Figure 6.9.

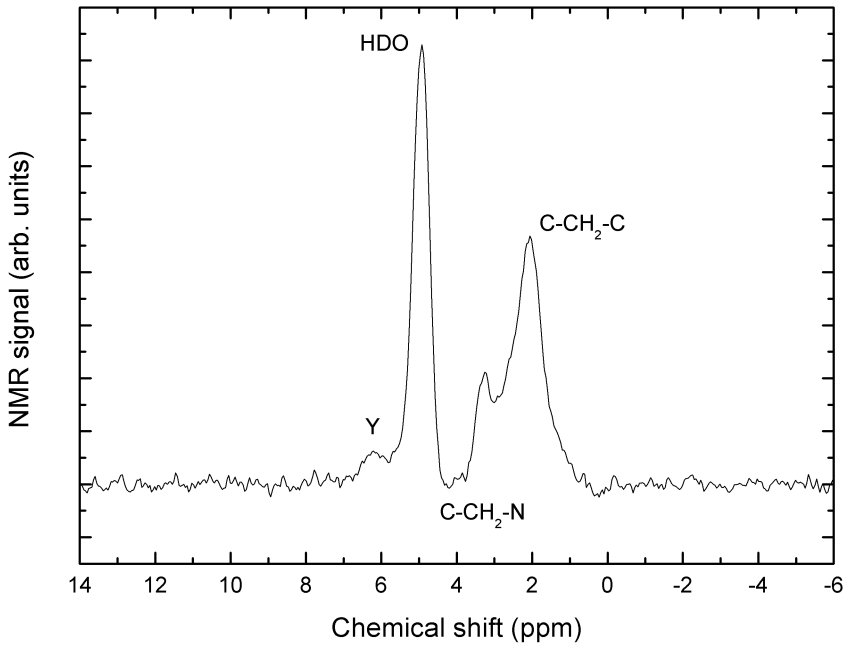

Figure 6.10: ^{1}H NMR spectrum of 1 M L-proline-100 mM TEMPOL-D_2O sample: no microwave irradiation, 48,000 acquisitions, 6.0 ± 0.5°C.

6.2.1 Experimental details

100 mM TEMPOL was dissolved in D_2O, followed by L-proline (*ReagentPlus*®, $\geq$ 99%, Sigma Aldrich) which was dissolved into the solution to a concentration of 1 M, below the maximum water solubility found in the literature (162.3 g/100 ml at 25°C [150]).

The standard method was used to seal the sample (length 10.5 mm) in quartz capillaries using epoxy resin.

Continuous-wave microwave irradiation was applied for the duration of all DNP experiments and the resulting change in temperature was measured by the chemical shift of water.

6.2.2 Results and discussion

The ^{1}H NMR spectrum at thermal equilibrium is shown in Figure 6.10. The spectrum was acquired over several hours whilst using nitrogen gas to maintain the sample temperature at 6°C, as measured by a thermocouple near the cavity. The two peaks upfield of the HDO signal have been identified as the methylene protons from C-CH_2-N and C-CH_2-C, which are known to occur at 3.37 ppm and 2.02–2.34 ppm, respectively (from BMRB Biological Magnetic Resonance Data Bank).

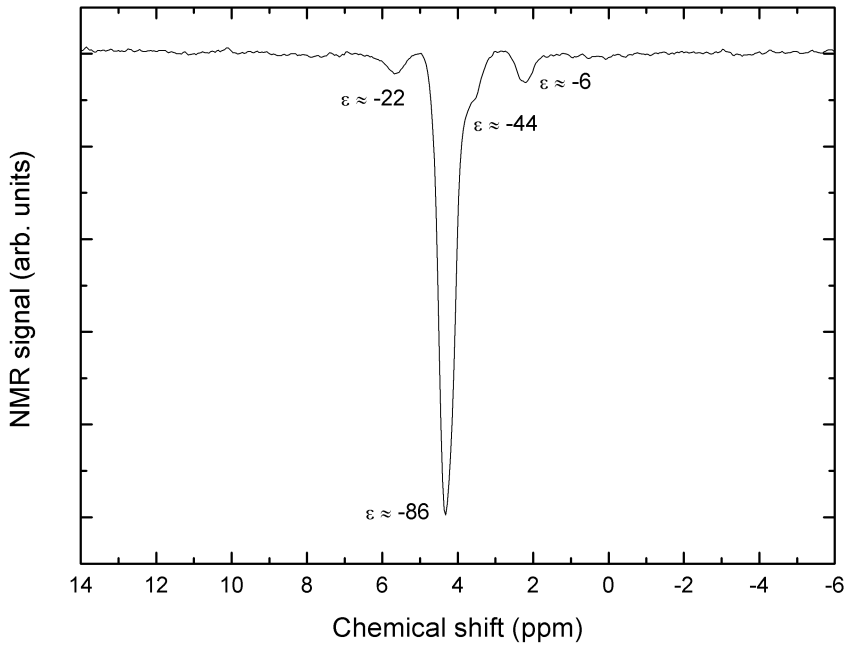

Figure 6.11: DNP-enhanced ^{1}H NMR spectrum of 1 M L-proline-100 mM TEMPOL-D_2O. ∼0.4 W applied microwave power, 200 acquisitions, 70 ± 3°C.

A signal from the CH group is expected at 4.12 ppm, but is too small to be clearly discernible. The labile protons of the hydroxyl and secondary amine groups of L-proline are not usually observed due to hydrogen-deuterium exchange. However, the peak labelled 'Y' is consistent with the usual chemical shift range of NH protons (5–8 ppm) and may be a due to residual protons that have not exchanged with the deuterium.

Figure 6.11 shows the DNP-enhanced NMR spectrum at 70°C. The negative enhancement of the HDO protons is much greater than the protons on the solute molecules, as observed with glycine (Section 6.1.2). The enhancement values were calculated using Equation 6.1 relative to the thermal equilibrium spectrum corrected for the change in Boltzmann factor at elevated temperature.

DNP spectra were recorded for a range of applied microwave powers and are plotted along with the thermal equilibrium spectrum in Figure 6.12. An incremental increase in ε with microwave power is observed for all the protons as well as the clear upfield shift in the water signal. This shift results in greater uncertainty in the integration of C-CH_2-N protons at high temperatures. Peak Y is also observed to shift upfield and its relatively strong NMR signal is greater than that expected for what was initially thought to be residual NH protons, which usually fully exchange. At the time of writing, the appearance of this resonance is not fully understood.

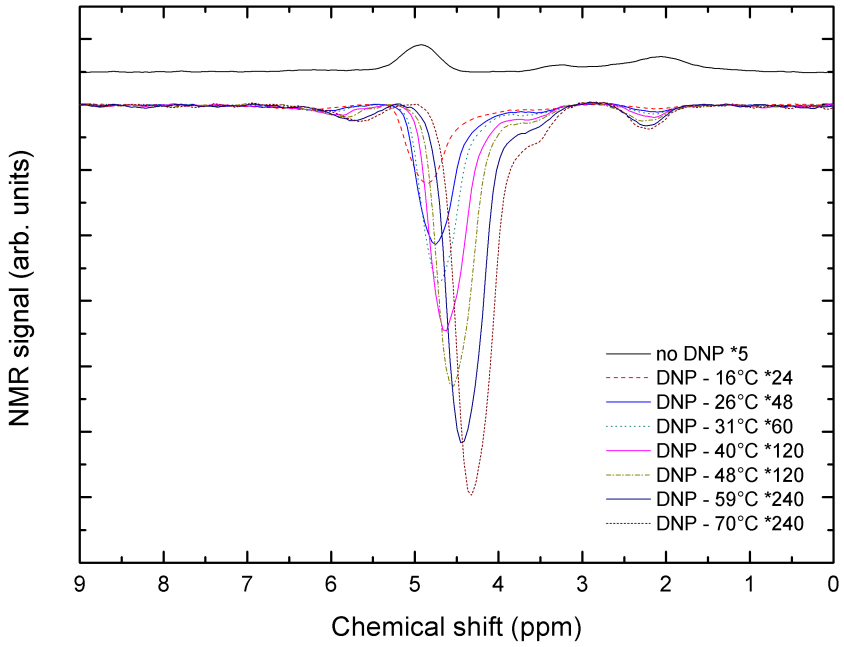

Figure 6.12: Overlay of DNP-enhanced spectra, demonstrating the increase of enhancement and temperature of HDO, C-CH_2-N and C-CH_2-C protons. The DNP spectra have been normalised to the same number of acquisitions and the thermal equilibrium spectrum (multiplied by a factor of 5) is displayed on top for comparison.

Temperature dependence of enhancement of HDO and CH_2 protons

The variation in enhancement with temperature is plotted in Figure 6.13. Equation 6.1 was used along with adjusted I_0 (for changing Boltzmann factors) values to calculate the enhancements. The maximum observed DNP enhancements were $\varepsilon_{\mathrm{HDO}} \approx -86$, $\varepsilon_{\text{C-CH}_2\text{-N}} \approx -44$, $\varepsilon_{\text{C-CH}_2\text{-C}} \approx -6$ and $\varepsilon_{\mathrm{Y}} \approx -22$ at 70°C.

The enhancement variation appears to be well described by a linear fit, with the exception of the C-CH_2-N protons which shows a sharper increase at high temperatures. This may be accounted for by merging with the HDO signal at high temperatures resulting in a poorer fit and overestimation.

Measurements to assess sample stability were not carried out, but with $\varepsilon_{\mathrm{HDO}}$ values similar to those obtained for glycine-TEMPOL-D_2O and the absence of a likely reducing agent, it is assumed that the radical was stable and the concentration remained at approximately 100 mM.

Appreciable enhancements, even at ∼40°C, were obtained for the protons in C-CH_2-N where $\varepsilon \approx -17$ and the average ratio of enhancements is $\varepsilon_{\mathrm{HDO}}/\varepsilon_{\text{C-CH}_2\text{-N}} = 2.7$. The C-$CH_2$-C protons, on the other hand, reached enhancements less than 10% of $\varepsilon_{\mathrm{HDO}}$ at the same temperature.

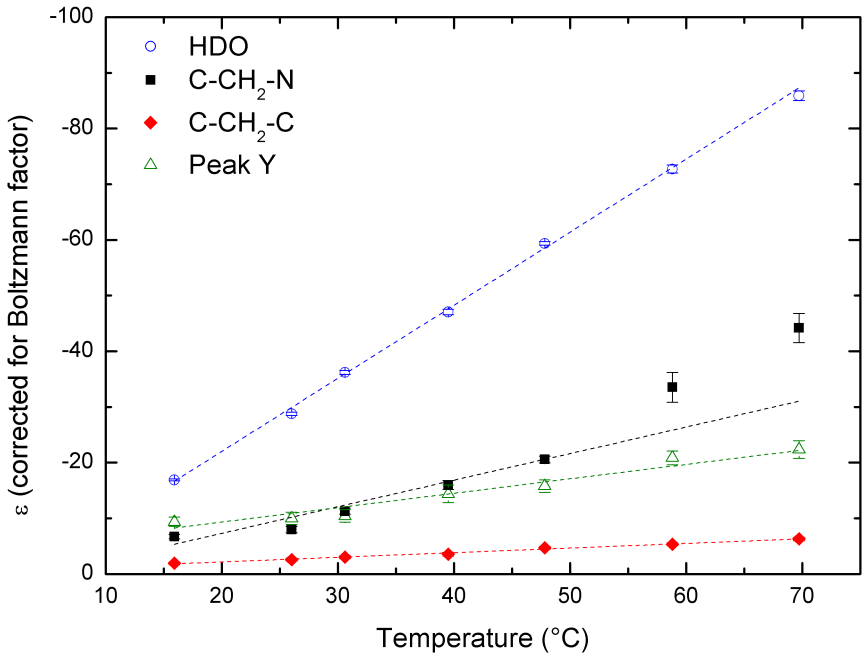

Figure 6.13: DNP enhancement as a function of temperature, as calculated by chemical shift change. Dashed lines — linear fits with slopes of -1.31, -0.48, -0.08 and -0.26 for HDO, C-CH_2-N, C-CH_2-C and Peak Y protons, respectively. Ratio of slopes $m_{\mathrm{HDO}}/m_{\text{C-CH}_2\text{-N}} = 2.8 \pm 0.4$, $m_{\mathrm{HDO}}/m_{\text{C-CH}_2\text{-C}} = 15.8 \pm 0.7$, $m_{\mathrm{HDO}}/m_{\mathrm{Y}} = 5.1 \pm 0.6$.

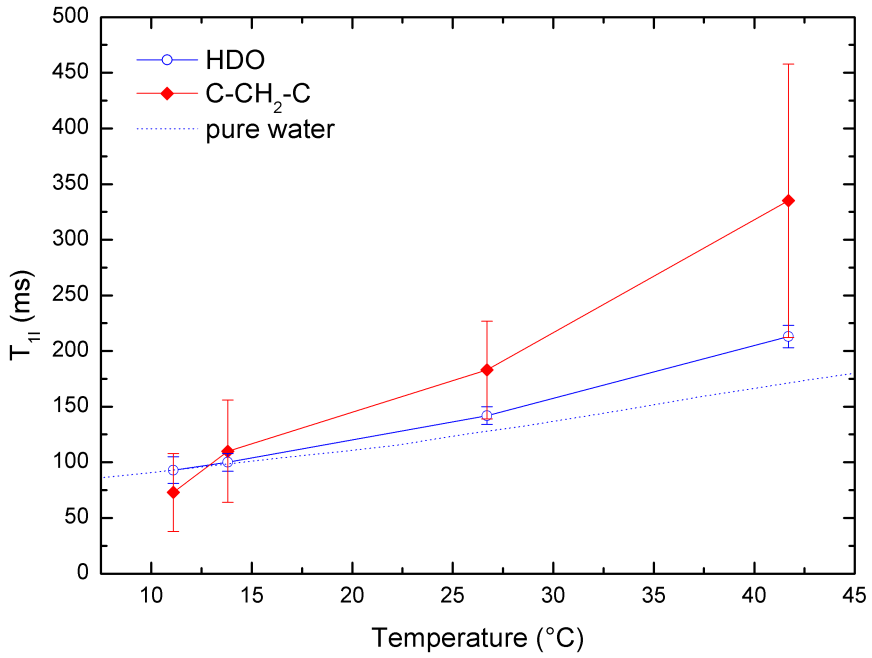

Figure 6.14: Effect of temperature on proton T_{1I} of HDO and C-CH_2-C in water doped with 100 Mm TEMPOL and 1 M L-proline. Data are shown with the temperature calculated from chemical shift, and have an uncertainty of approximately ± 3°C. The T_{1I} of pure water has been included, and scaled to agree with the sample value at 11°C, for comparison.

Measurement of T_1 by saturation-recovery

Saturation-recovery experiments were used to measure T_{1I} at 143 MHz. DNP was used in order to obtain satisfactory signal-to-noise, and was also used to heat the sample. However, even so, only the HDO and C-CH_2-C proton resonances could be resolved. The HDO signal was strong as expected, giving data which could be easily fitted; whilst the data from the methylene group was quite scattered, producing much larger errors.

Several measurements of the relaxation time were made over a range of temperatures (Figure 6.14). The temperature dependence of the relaxation time of pure water (scaled to agree at 11°C) is plotted as a dotted line, and shows reasonable agreement with the HDO protons in the sample.

Coupling factor ξ — an estimation

Applying the same strategy as in Section 6.1.2, the coupling factors for the HDO and C-CH_2-C protons are estimated and their ratio compared with that predicted by a FFHS model.

T_{1I0} measurements were not made for a non-doped sample of L-proline in D_2O, however, from Figure 6.14 the T_{1I} values at 27°C are known and found to be of the same order of magnitude as the glycine sample T_{1I}. Since L-proline is not expected to dramatically decrease the T_{1I} of water, the condition $T_{1I,HDO} \gg T_{1I,pro}$ (where the subscript 'pro' refers to the C-CH_2-C protons in L-proline) should still exist. Therefore, for the following analysis, the leakage factor is assumed to be $f \approx 0.98$.

It is further assumed that the radical concentration is sufficiently high for $s \approx 1$, and using $\varepsilon_{HDO} = -35.9$ and $\varepsilon_{pro} = -3.0$ at 31°C (Figure 6.13), the coupling factors at 31°C are estimated to be $\xi_{HDO} = 0.056 \pm 0.008$ and $\xi_{pro} = 0.005 \pm 0.001$. As before, the uncertainty regarding the saturation factor can be eliminated by expressing the results as the saturation-independent ratio $\xi_{HDO}/\xi_{pro} = 12.0 \pm 2.6$.

Continuing the analysis as for the glycine sample, the coupling factor ratio can also be calculated using Equation 6.7:

$$\frac{\xi_{HDO}}{\xi_{pro}} = \left(\frac{\tau_{HDO}}{\tau_{pro}}\right)^{-3/2} = \left(\frac{D_S + D_{HDO}}{D_S + D_{pro}}\right)^{3/2} \tag{6.7}$$

using $D_{HDO} = D_{H_2O} = 2.3 \times 10^{-9}$ m^2s^{-1} [148]; $D_{pro} = D_{L\text{-proline}} = 0.879 \times 10^{-9}$ m^2s^{-1} [151]; and assuming the diffusion coefficient for TEMPOL is the same as 4-oxo-TEMPO, $D_S = 0.41 \times 10^{-}9$ m^2s^{-1} [38]. A coupling factor ratio is then calculated to be $\xi_{HDO,\,calc}/\xi_{pro,\,calc} = 3.0 \pm 0.2$.

The theoretically predicted ratio is much smaller than the measured value (by a factor of 4), implying much weaker coupling to the C-CH_2-C protons than expected.

6.3 Acrylic acid

Acrylic acid is the simplest unsaturated carboxylic acid and has a molar mass of 72.06 g mol^{-1}, very similar to that of glycine. Like glycine, its small and simple structure as well its complete miscibility with water make it ideal for study using this system. In addition, it displays a proton resonance at a chemical shift larger than that of water protons. So in an acrylic acid-water sample, as it is heated and the proton resonance of water moves to lower chemical shifts, there is no problem resolving the two signals. The structure of acrylic acid is given in Figure 6.15.

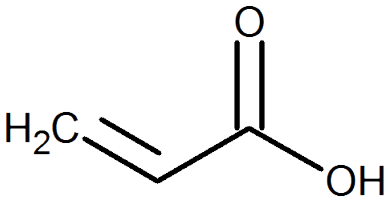

Figure 6.15: Skeletal formula of acrylic acid ($CH_2CHCOOH$).

6.3.1 Experimental details

A solution of 50% acrylic acid (99%, Sigma Aldrich) and 50% D_2O (99.9 atom % D, Sigma Aldrich) was made up first. The inclusion of acid in the solution was found to corrode the epoxy resin used to seal the sample capillary (see Section 4.2, Chapter 4) within a matter of hours, so the proportion of acid and water was varied in an attempt to find a more suitable mixture. A solution of 10% acrylic acid and 90% D_2O (by volume) proved low enough in concentration to not corrode the seals (checked over several weeks) and so 100 mM TEMPOL was then dissolved in the solution to complete the sample. No degassing was performed.

The standard preparation method was used to seal the sample of length 11 mm in capillary tubes.

Continuous-wave microwave irradiation was used for all DNP experiments and temperature changes were measured using the change in the water proton chemical shift.

6.3.2 Results and discussion

The thermal equilibrium reference ^{1}H NMR spectrum is shown in Figure 6.16. Signal was acquired over several hours whilst the temperature was kept constant at 6°C using nitrogen gas flow. The peak labelled 'AA' is attributed to the CH_2 and CH protons from the acrylic acid molecule, which usually appear in the range 5.96–6.52 ppm (Spectral Database for Organic Compounds SDBS) and cannot be resolved using the current experimental setup. The OH protons (usually observed at 12.0 ppm) in the acrylic acid exchange with deuterium, since D_2O was used as a solvent, leaving two peaks (HDO and AA) we expect to observe in the spectrum. However, there is clearly a peak observable at ∼1 ppm (labelled 'Peak X'), which was not observed in ^{1}H NMR spectra of pure acrylic acid collected at 284 MHz. The occurrence of this signal is consistent with the product TEMPOL reduction, i.e. it is the signal from the four degenerate methyl groups of the diamagnetic molecule

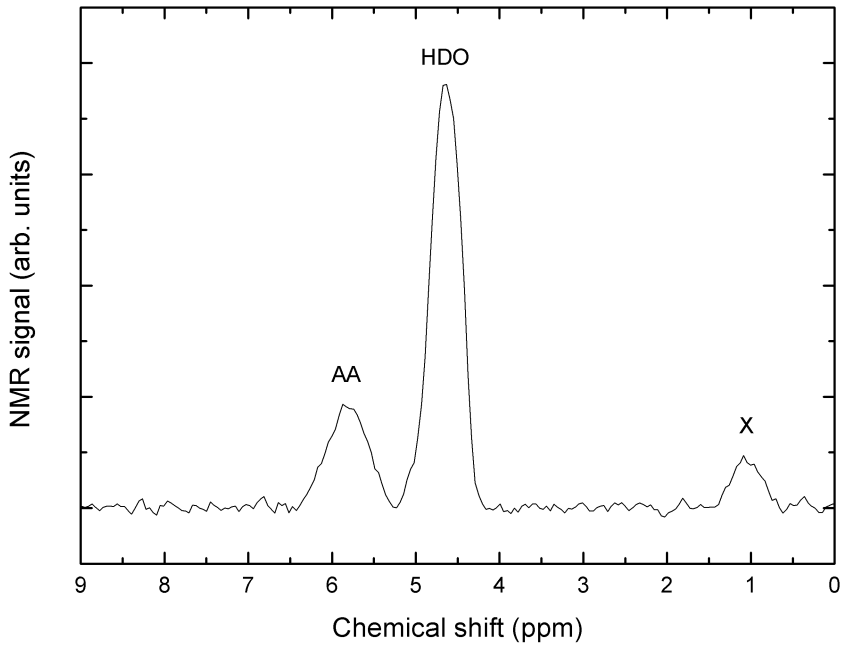

Figure 6.16: ^{1}H NMR spectrum of acrylic acid-D_2O(10:90 % v/v)-100 mM TEMPOL sample: no microwave irradiation, 100,000 acquisitions, 6.0 ± 0.5°C.

'TEMPOL-H'. The appearance of this proton signal was observed by Miéville et al. [152] as the paramagnetic TEMPOL was reduced by ascorbate to TEMPOL-H, revealing the previously undetectable methyl group protons at 1.28 ppm. It is proposed here that the TEMPOL radical has been reduced in a similar fashion by the proton-donating acrylic acid (see Figure 6.17).

Figure 6.18 shows the DNP-enhanced NMR spectrum of the sample at 83°C. As observed with the two previously studied systems, the negative enhancement is much greater for the HDO protons of the small water molecule than for AA or TEMPOL-H. Slight asymmetry of the HDO lineshape can likely be attributed to uneven sample heating resulting from the familiar problem of having a sample length greater than the cavity dimensions at high microwave frequencies. Enhancements were once again calculated using integrated intensities and Equation 6.1.

DNP spectra were obtained over a range of temperatures and are plotted in Figure 6.19 along with the thermal equilibrium spectrum for comparison. The increasing enhancement of the HDO and AA protons with rising temperature is clear; the signal from the CH_3 protons of TEMPOL-H, on the other hand, is very weak. As the applied microwave power is increased, there is a corresponding rise in temperature and therefore change in the chemical shift of water. Since the HDO peak is at a lower shift than AA, as the temperature rises the HDO resonance

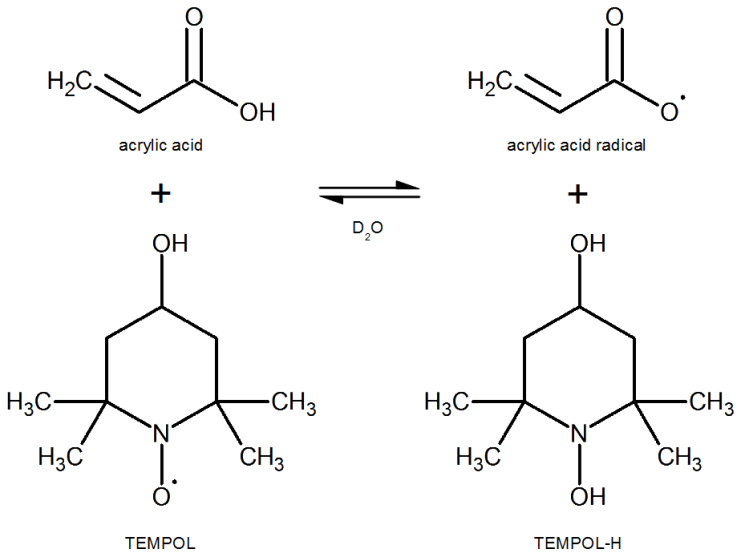

Figure 6.17: The reduction of TEMPOL by acrylic acid, resulting in the formation of the diamagnetic TEMPOL-H molecule.

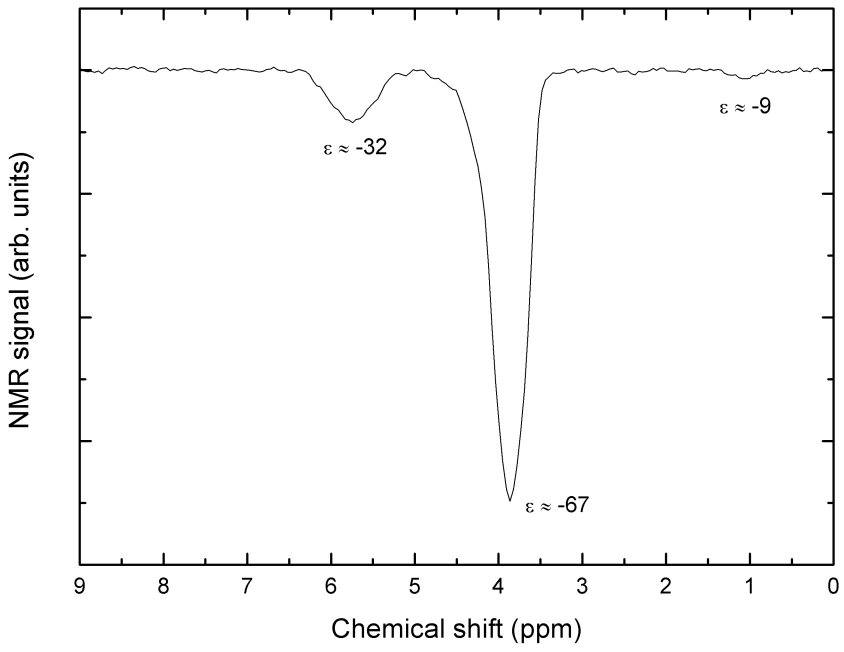

Figure 6.18: DNP-enhanced ^{1}H NMR spectrum of acrylic acid-D_2O-100 mM TEMPOL. ∼1.7 W applied microwave power, 400 acquisitions, 83 ± 3°C.

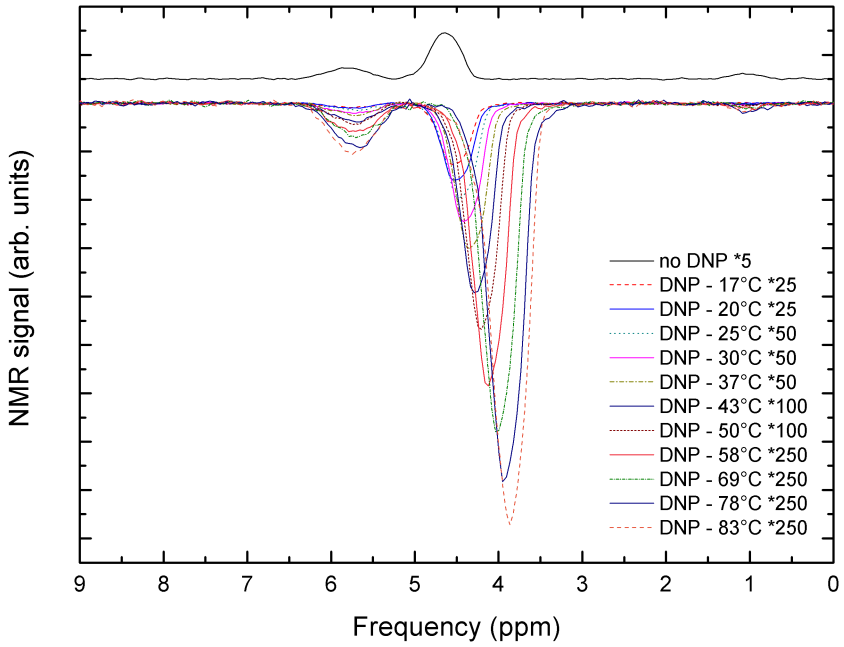

Figure 6.19: Overlay of DNP-enhanced spectra, showing the increasing enhancement of HDO and AA protons, whilst showing the changing shift of HDO and constant position of AA. The DNP spectra have been normalised to the same number of acquisitions and the thermal equilibrium signal (top) increased by a factor of 5 for comparison.

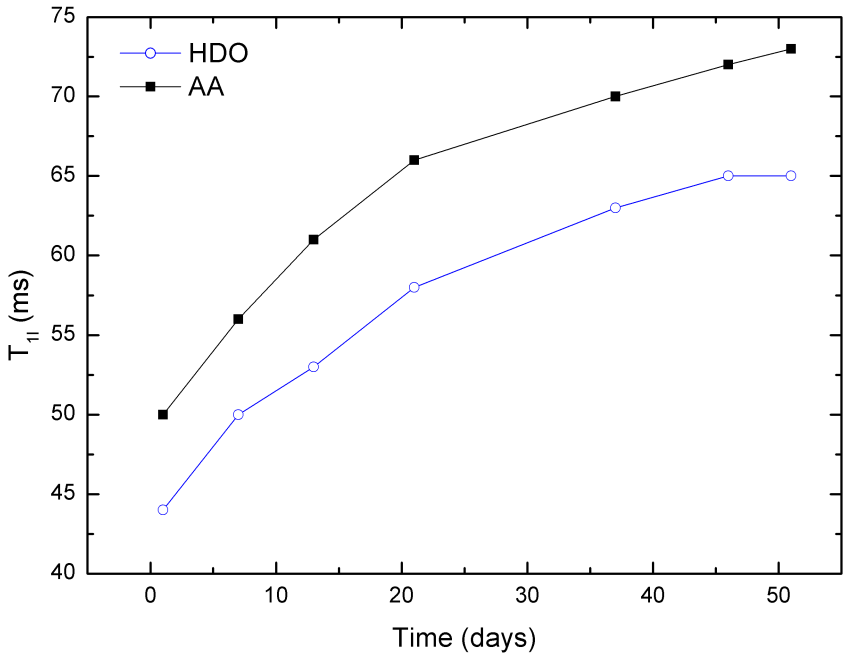

Figure 6.20: Change in nuclear spin-lattice relaxation time as a function of time, due to reduction of TEMPOL. Measured at room temperature at 284 MHz.

shifts upfield, moving further away from the AA signal, and the resolution problem associated with the glycine-TEMPOL-D_2O and L-proline-TEMPOL-D_2O systems at high temperatures is not experienced.

Sample stability — T_1 measurements at 284 MHz and CW-EPR signal intensities

As a measure of sample stability, the nuclear spin-lattice relaxation time was measured periodically over several weeks. Owing to the weak NMR signal in the absence of microwave irradiation, inversion-recovery experiments were conducted at 284 MHz on a 600 MHz sweepable Varian NMR spectrometer using a much larger sample volume since it is only the change in T_{1I} that is of interest. Figure 6.20 shows the results and demonstrates that the relaxation time is continually and considerably increasing over the 7 weeks where measurements were recorded — an approximately 50% increase from 44 ms to 65 ms over 45 days. This increase in nuclear relaxation time suggests a decrease in the concentration of the paramagnetic TEMPOL.

This was further investigated using CW-EPR. Figure 6.21 shows the variation of the integrated signal intensity from a series of room temperature experiments, collected on a Bruker X-band EPR spectrometer. There is a very rapid drop in signal

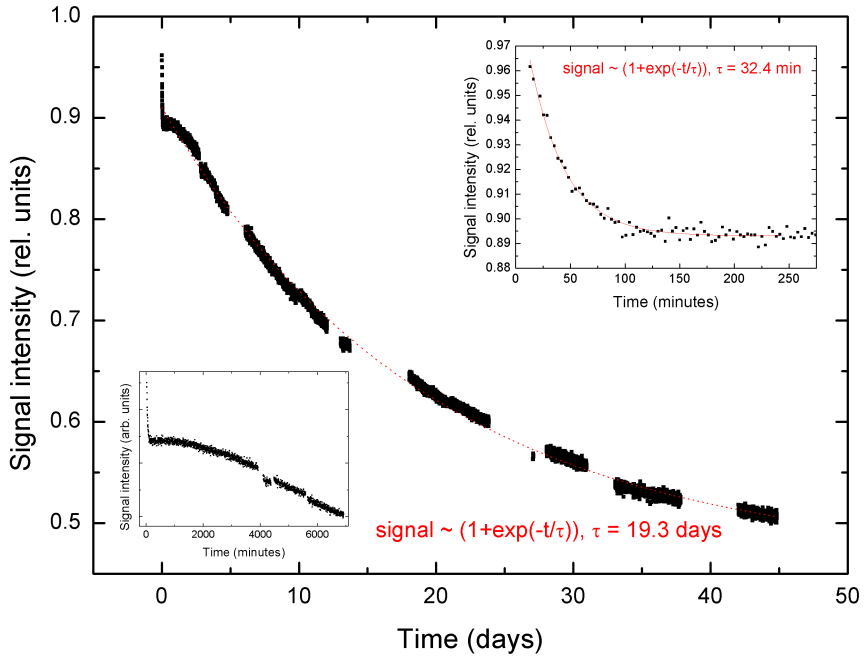

Figure 6.21: Evolution of integrated X-band EPR signal intensity with time, showing a continuous degradation of TEMPOL radical at room temperature. Inset — expansion of the first 275 minutes after the sample was prepared.

to about 90% of the original value ∼90 minutes after the solution was made up; this seems to be well described by a single exponential decay, with a characteristic time of 32.4 minutes. After the first few hours, the decay of the signal is much slower and the subsequent region can be reasonably approximated as a single exponential decay with characteristic time $\tau \approx 19$ days. After 45 days, the EPR signal from the sample drops to approximately 50%, consistent with the measured 50% increase in T_1 over the same time period. This data provides further evidence that the usually stable TEMPOL is being reduced, and that the concentration during DNP experiments will therefore no longer be 100 mM. However, over the timescale of the DNP experiments the radical concentration, whilst lower, can be assumed to be essentially constant due to the slow rate of decay.

Temperature dependence of enhancement of HDO and CH/CH_2 protons

The temperature dependence of ε is presented in Figure 6.22. The enhancements were calculated using Equation 6.1 and I_0 values adjusted for the different Boltzmann factors at different temperatures. The maximum observed enhancements were $\varepsilon_{\mathrm{HDO}} \approx -67$ and $\varepsilon_{\mathrm{AA}} \approx -32$ at 83°C.

The temperature dependence of the AA protons appears to be quite linear

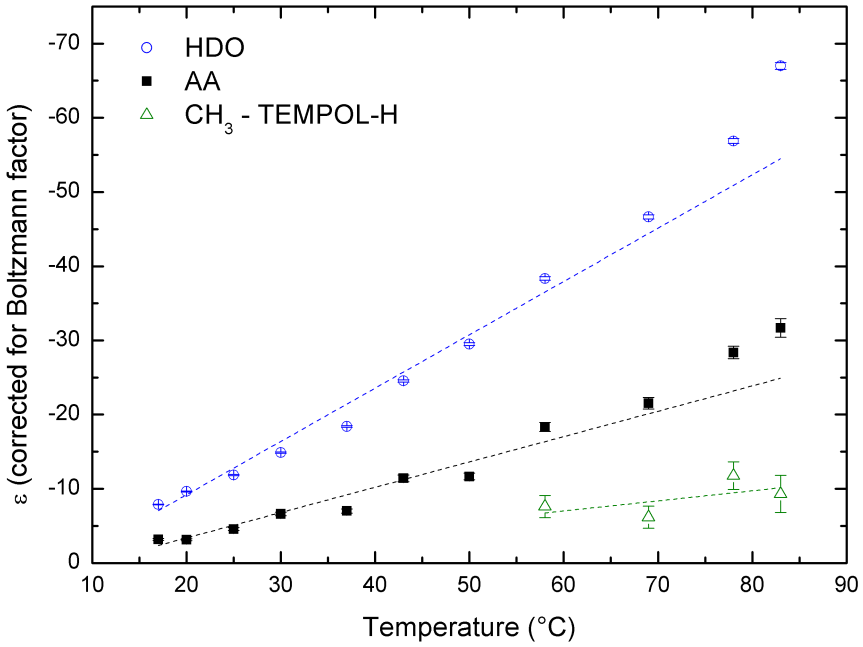

Figure 6.22: Temperature dependence of DNP enhancement, with temperatures calculated from change in chemical shift of water protons. Dashed lines — linear fits with slopes of -0.72, -0.34 and -0.14 for HDO, AA and CH_3 protons, respectively. Ratio of slopes $m_{\mathrm{HDO}}/m_{\mathrm{AA}} = 2.1 \pm 0.2$, $m_{\mathrm{HDO}}/m_{\mathrm{CH_3}} = 5.3 \pm 5.3$.

up to ∼70°C, with the two highest temperature data points apparently rising faster with temperature. The rate of increase in enhancement for the HDO protons seems to be increasing and is particularly noticeable at high temperatures. This may be the result of lower radical concentration (due to reduction by AA) giving $s < 1$ at lower temperatures. In DNP experiments where high power microwaves combined with high radical concentrations give $s \approx f \approx 1$, the increasing enhancement with rising temperature is a result of faster translational motion between the radical and target molecules increasing the modulation of the dipolar hyperfine interactions and thereby increasing the enhancement. Perhaps the additional increase in ε with temperature observed here comes from an increase in saturation as the sample heats.

The enhancements observed are somewhat lower than in the glycine system, with $\varepsilon_{\mathrm{HDO}} \approx -22$ and $\varepsilon_{\mathrm{CH_2}} \approx -10$ at ∼40°C. This is likely a result of the lower TEMPOL concentration in the sample. The experiments were conducted over a period of about half a day, 21 days after the sample was prepared. The results of Figure 6.21 suggest that the radical concentration would have decreased to ∼60 mM by the time of the DNP experiments if the sample were at room temperature. However, it is likely that the heating associated with DNP experiments would speed up the reduction process, giving an average concentration of ≤60 mM.

The enhancements of the methyl protons of the TEMPOL-H molecule are also plotted for the higher temperatures where it was observable. But further discussion will be restricted to water and acrylic acid.

The ratio of the slopes for the solvent and solute protons in Figure 6.22 was found to be ∼2, corresponding to stronger coupling of the radical electron spin to the solvent molecules than the solute.

Measurement of T_1 by saturation-recovery

$T_{1\mathrm{I}}$ was measured at a range of temperatures (see Figure 6.23) at 143 MHz using DNP. A relatively large error is estimated for the AA protons which is attributed to the array of delay times τ selected not allowing characterisation of the full exponential build up at high temperatures (long relaxation times). The uncertainty of $T_{1\mathrm{I}}$ was generally found to be lower at lower temperatures. The two types of proton were found to have a similar temperature dependence (to within experimental uncertainty), with $T_{1\mathrm{I,HDO}}$ perhaps ∼1.5–2.5 times longer. This temperature dependence also appears to match that of pure water quite well, which has been scaled to agree at 4°C and plotted as a dotted line. The relaxation time of HDO in this sample is significantly longer than HDO in the glycine sample (Figure 6.7), where for example $T_{1\mathrm{I,HDO}}$ at 63°C is 367 ms and 135 ms in the AA and glycine sample, respectively.

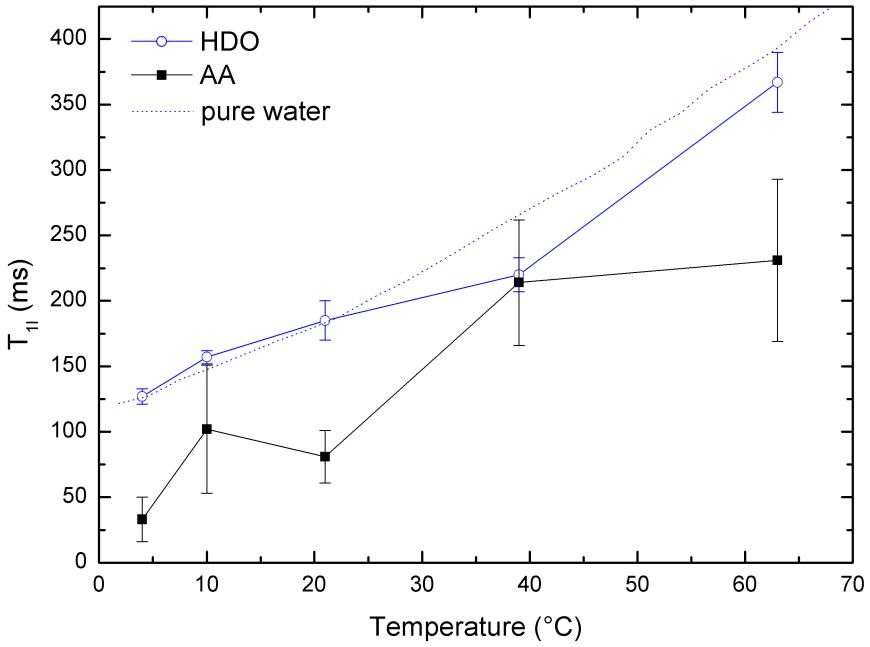

Figure 6.23: Temperature dependence of proton T_{1I} of HDO and AA protons in D_2O with acrylic acid and an initial radical concentration of 100 mM TEMPOL which is thought to have reduced by at least ∼40%. Data are shown with temperatures indicated by HDO chemical shift. The T_{1I} of pure water is shown as a dotted line and has been scaled to agree with the sample value at 4°C.

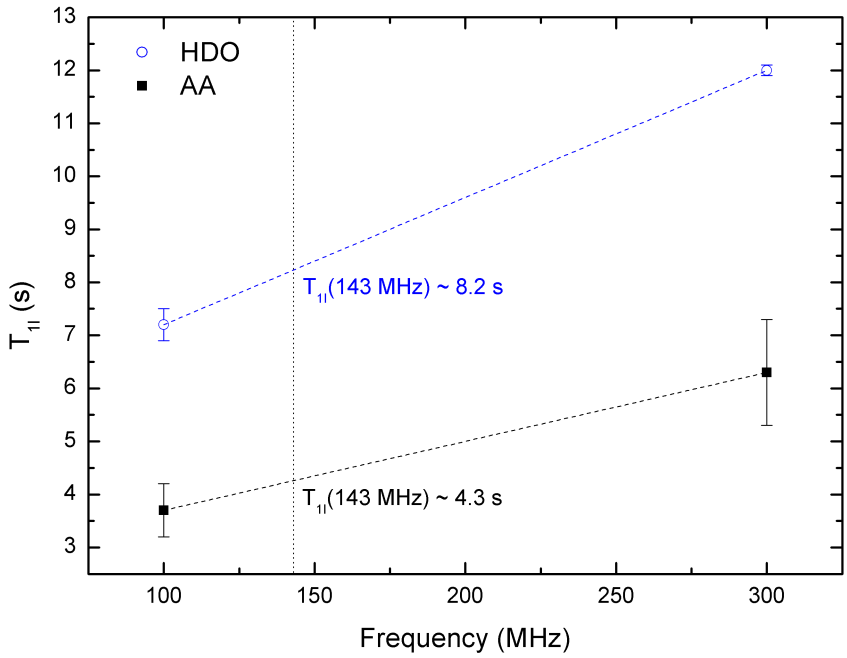

Figure 6.24: $T_{1\mathrm{I}}$ values of acrylic acid-D_2O (10:90 % v/v) at 143 MHz at room temperature, interpolated from measurements made at 100 MHz and 300 MHz.

This difference is at least qualitatively consistent with lower radical concentration and also increased viscosity of the solution due to the inclusion of acrylic acid [153].

Coupling factor ξ — an estimation

In the following section, the coupling factors for the HDO and AA protons are calculated and their ratio compared with that predicted by a FFHS model in the same manner as Section 6.1.2.

A non-doped solution of acrylic acid and D_2O (10:90 % v/v) was used to measure the relaxation time in the absence of the radical. Measurements carried out using a larger volume sample (~16 μl) at 100 MHz and 300 MHz were used to interpolate $T_{1\mathrm{I}}$ at 143 MHz, due to the low signal-to-noise ratio of non-enhanced spectra preventing T_1 experiments being carried out on the 143 MHz/94 GHz DNP system within an acceptable time frame.

The results of measurements made at 100 MHz and 300 MHz are shown in Figure 6.24. An assumption of linearity in the frequency range led to relaxation times of $T_{1\mathrm{I,HDO}} = 8.2$ s and $T_{1\mathrm{I,AA}} = 4.3$ s at room temperature (approximately 20°C) at 143 MHz.

Using Equation 6.2 for f and $T_{1\mathrm{I}}$ values from Figure 6.23 at 21°C, the leakage

factors at 20°C were calculated to be $f_{\mathrm{HDO}} \approx f_{\mathrm{AA}} \approx 0.98$.

Assuming that the radical concentration is still high enough for $s \approx 1$, and using $\varepsilon_{\mathrm{HDO}} = -9.6$ and $\varepsilon_{\mathrm{AA}} = -3.1$ at 20°C (Figure 6.22), the coupling factor at 20°C was estimated to be $\xi_{\mathrm{HDO}} = 0.015 \pm 0.005$ and $\xi_{\mathrm{AA}} = 0.005 \pm 0.003$, where the large uncertainties are dominated by a large estimated error on $s = 1$ as well as a large fractional error on $\varepsilon_{\mathrm{AA}}$. It is likely that despite reasonably high microwave powers (∼230 mW), due to the lower concentration (∼60 mM) of TEMPOL, that full saturation is not quite reached. In this case, the values of ξ estimated here still provide a lower limit and the saturation-independent ratio can still be evaluated using Equation 6.8:

$$\frac{\xi_{\mathrm{HDO}}}{\xi_{\mathrm{AA}}} = \frac{\varepsilon_{\mathrm{HDO}} f_{\mathrm{AA}}}{\varepsilon_{\mathrm{AA}} f_{\mathrm{HDO}}} \tag{6.8}$$

giving an experimental value of $\xi_{\mathrm{HDO}}/\xi_{\mathrm{AA}} = 3.1 \pm 1.2$.

As shown in Section 6.1.2, this coupling factor ratio can be related to the diffusion constants of the relevant molecules via the following equation:

$$\frac{\xi_{\mathrm{HDO}}}{\xi_{\mathrm{AA}}} = \left(\frac{\tau_{\mathrm{HDO}}}{\tau_{\mathrm{AA}}}\right)^{-3/2} = \left(\frac{D_{\mathrm{S}} + D_{\mathrm{HDO}}}{D_{\mathrm{S}} + D_{\mathrm{AA}}}\right)^{3/2} \tag{6.9}$$

using $D_{\mathrm{HDO}} = D_{\mathrm{H_2O}} = 2.3 \times 10^{-9}$ $\mathrm{m^2 s^{-1}}$ [148]; $D_{\mathrm{AA}} = 1.06 \times 10^{-9}$ $\mathrm{m^2 s^{-1}}$ [154]; and assuming the diffusion coefficient for TEMPOL is the same as 4-oxo-TEMPO, $D_{\mathrm{S}} = 0.41 \times 10^{-}9$ $\mathrm{m^2 s^{-1}}$ [38]. A coupling factor ratio is then calculated to be $\xi_{\mathrm{HDO,\ calc}}/\xi_{\mathrm{AA,\ calc}} = 2.5 \pm 0.1$.

The measured ratio $\xi_{\mathrm{HDO}}/\xi_{\mathrm{AA}} = 3.1 \pm 1.2$ is similar to the theoretically predicted value. Like the result for glycine-TEMPOL-D_2O, its experimentally determined value is slightly larger, indicating weaker than predicted coupling to the AA protons.

The measured leakage factors and coupling factors for the glycine, L-proline and acrylic acid samples are summarised in Table 6.1.

6.4 Conclusions

This chapter has presented for the first time (to the author's knowledge) liquid-state ^{1}H DNP enhancements of molecules dissolved in solution at 3.4 T. At elevated sample temperatures (70–90°C), significant enhancements of $\varepsilon \approx -27, -44$ and -32 have been obtained for protons on glycine, L-proline and acrylic acid, respectively. The lossy nature of water at high frequencies renders heating virtually unavoidable, but liquid DNP may still be useful. Measuring the DNP enhancement as a function

3 M glycine-100 mM TEMPOL-D_2O			
	HDO	CH_2	Temperature (°C)
T_{1I} (ms)	105	90	27
T_{1I0} (ms)	6500	2200	20
$f \geq$	0.98	0.96	27
ε ($\sim$ 280 mW*)	-36.8	-8.8	27
$\xi \approx$	0.057	0.014	27
1 M L-proline-100 mM TEMPOL-D_2O			
	HDO	C-CH_2-C	Temperature (°C)
T_{1I} (ms)	142	183	27
T_{1I0} (ms)	—	—	—
$^{\dagger}f \approx$	0.98	0.96	31
ε	-35.9	-3.0	31
$\xi \sim$	0.056	0.005	31
acrylic acid-D_2O(10:90 % v/v)-c mM TEMPOL‡			
	HDO	AA	Temperature (°C)
T_{1I} (ms)	185	102	21
T_{1I0} (ms)	8200	4300	20
$f \approx$	0.98	0.98	20
ε ($\sim$ 230 mW*)	-9.6	-3.1	20
$\xi \geq$	0.015	0.005	20

* applied continuous-wave microwave power

† $f_{\text{L-proline}}$ assumed to be similar to f_{glycine}

‡ concentration c initially 100 mM, thought to be $\leq$60 mM at time of experiment

Table 6.1: Summary of relaxation time and enhancement measurements used to estimate leakage factors and coupling factors in three different samples of organic compounds in aqueous solutions.

of temperature has demonstrated that relatively high sensitivity can still be obtained whilst maintaining more biologically and physiologically acceptable temperatures.

At around 40°C, $\varepsilon \approx -17, -16$ and -11 for protons on glycine, L-proline and acrylic acid, respectively, have been measured. These enhancements of molecules several times larger than water are encouraging for the potential of liquid DNP applications, and were not until recently believed to be feasible at high fields. However, as Krummenacker et al. recently demonstrated [98], this enhancement of solute nuclei occurs through direct coupling to the radical and not via polarisation transfer from solvent protons. This may place limitations on the technique as larger sample molecules are desired and target protons become less accessible; leading to a greater distance of closest approach and weaker coupling to the unpaired electron spin.

High DNP enhancements of solvent water protons ($|\varepsilon| > 100$) have also been achieved at temperatures approaching the boiling point of water.

Evidence for the reduction of TEMPOL to the diamagnetic TEMPOL-H radical has been observed and found to be a relatively slow process in the case of acrylic acid acting as a reducing agent at room temperature. The possibility of this effect must be considered when choosing samples as it has the potential to dramatically decrease the lifetime of samples which could normally remain stable for months, as well as reducing the maximum attainable enhancement.

Coupling factors were estimated for the three compounds studied — glycine, L-proline and acrylic acid. For the glycine solution, $\xi_{\mathrm{HDO}} \approx 0.057$ was found to be in good agreement with previous work (cf. Table 5.1, Chapter 5), suggesting that the value of $\xi_{\mathrm{CH_2}} \approx 0.014$ is a reasonable estimate. For the L-proline solution, due to a lack of data assumptions had to be made about the leakage factor; however $f \sim 1$ at the high radical concentration used seems justified. Coupling factors of $\xi_{\mathrm{HDO}} \approx 0.056$ and $\xi_{\mathrm{C\text{-}CH_2\text{-}C}} \approx 0.005$ were estimated. Considerably smaller (3–4 times) coupling factors were obtained for the acrylic acid sample: $\xi_{\mathrm{HDO}} \approx 0.015$ and $\xi_{\mathrm{AA}} \approx 0.005$. The comparatively small ξ_{HDO} value suggests that the radical may have been reduced so much that the assumption of $s \approx 1$ becomes invalid.

Since it is the difference in the Overhauser enhancement for solvent and solute that is of greatest interest here, the saturation factor, which is often uncertain, can be eliminated from the analysis by taking the ratio of coupling factors. Utilising a FFHS model, these ratios can also be predicted based on known diffusion coefficients. The following experimental and theoretical ratios were found for glycine, L-proline and acrylic acid: $[\xi_{\mathrm{HDO}}/\xi_{\mathrm{CH_2}} = 4.1,\ \xi_{\mathrm{HDO,calc}}/\xi_{\mathrm{CH_2,calc}} = 3.6]$; $[\xi_{\mathrm{HDO}}/\xi_{\mathrm{C\text{-}CH_2\text{-}C}} = 11.7,\ \xi_{\mathrm{HDO,calc}}/\xi_{\mathrm{C\text{-}CH_2\text{-}C,calc}} = 3.0]$; and $[\xi_{\mathrm{HDO}}/\xi_{\mathrm{AA}} = 3.1,\ \xi_{\mathrm{HDO,calc}}/\xi_{\mathrm{AA,calc}} = 2.5]$. The experimentally measured and the calculated ratios for glycine and acrylic acid are in

reasonable agreement with each other. However, for all three systems, comparison shows that the coupling of the electron spin of the polarising agent to the target molecule proton is weaker than predicted. This is in contrast to Krummenacker et al. [98], who observed that the coupling to the methyl protons of the solute molecule (for Na-pyruvate, Na-lactate and alanine) was stronger than predicted. The magnitude of these discrepancies provides further evidence that the local dynamics of the radical and target molecule are important for proper analysis of Overhauser DNP at high fields, and a simple FFHS approach may no longer be appropriate, even with relatively small molecules. A more sophisticated analysis, such as that adopted by Sezer [42], may now be required for high-field liquid DNP.

Chapter 7

Investigation of saturation by simultaneous irradiation of two EPR lines

7.1 Introduction

The saturation factor s in a DNP experiment is a measure of the extent of saturation of the electron spin transitions of radicals in the sample. It is dependent on the applied microwave power and electron relaxation and can take values between 0 and 1. As one of the three parameters that reduce Overhauser DNP enhancement from the maximum possible value (γ_S/γ_I), understanding it is essential to interpreting DNP experiments, and maximising it is important to improve sensitivity. The saturation factor is often defined as

$$s = \frac{S_0 - \langle S_z \rangle}{S_0} = \frac{\gamma_S^2 B_1^2 T_{1S} T_{2S}}{1 + \gamma_S^2 B_1^2 T_{1S} T_{2S}} \tag{2.49}$$

which can also be expressed in terms of applied microwave power P (since $P \propto B_1^2$):

$$s = \frac{\alpha P}{1 + \alpha P} \tag{7.1}$$

where α is a numerical factor accounting for the electron relaxation times T_{1S} and T_{2S}, and the properties of the cavity [6, 123, 111].

However, the situation is more complex for radicals which have more than one transition as a result of hyperfine interaction with a nucleus of spin $I > 0$. This is the case, for example, with nitroxide radicals commonly used in EPR and DNP

where the unpaired electron interacts with a nitrogen nucleus of spin $I = 1$ (^{14}N) or $I = 1/2$ (^{15}N). Classically, it was predicted that a maximum saturation of only $s_{\max} = 1/3$ could be achieved when pumping one transition (in the case of the more common nitrogen isotope ^{14}N) [20] and, in general, the saturation is then given by:

$$s = \frac{1}{n}\left(\frac{\alpha P}{1 + \alpha P}\right) \tag{7.2}$$

where n is the number of hyperfine lines [123].

Usually, only one hyperfine line is saturated at a time, but partial saturation of the other transitions can be obtained through the mixing of lines via two processes. Bates et al. [124] proposed a model which incorporated Heisenberg electron spin exchange: this occurs if radical collisions — where opposite electron spins are exchanged between molecules with nitrogen nuclei in different spin states — occur frequently relative to the electron spin-lattice relaxation time [37]. Armstrong et al. [111] later extended this model to include the effect of intramolecular nitrogen spin relaxation in nitroxides which, when faster than the electron relaxation, can cause further mixing of the EPR transitions. They proposed an equation for predicting the maximum saturation factor (Equation 7.3), which showed good agreement with their data at 0.35 T:

$$s_{\max} = \frac{1}{3}\left(\frac{1 + 3Ck/p}{1 + Ck/p}\right) \tag{7.3}$$

where C is the radical concentration in mM, k is the exchange rate per mM and p is the electron relaxation rate. It is can be seen from Equation 7.3 that at low concentrations ($C \to 0$) the maximum saturation does indeed reduce to 1/3, but at high concentrations ($Ck/p \gg 1$) the saturation factor tends to 1. So this implies that these two effects of Heisenberg exchange and nuclear relaxation may give rise to saturation factors approaching $s_{\max} = 1$, even when only one resonance in the hyperfine split EPR spectrum is saturated. These previous models were based on classical relaxation theory and account only for T_{1S} of the electrons. The effect of electron spin-spin relaxation in theory describing the saturation factor was later included by Sezer et al. [155] by evoking semi-classical relaxation theory [20, 156] and considering the density matrix of the electron-nitrogen system.

It is possible to avoid such considerations by choosing radicals which display only one EPR resonance, for example, a trityl radical. However, experiments at 3.4 T comparing trityl with TEMPOL have shown it to be a less favourable polarising agent for solution-state DNP; resulting in lower DNP enhancements which

have been attributed to a greater distance of closest approach and therefore slower modulation of the electron-nuclear interaction between the radical electron and solvent protons [113]. It seems for now at least, the nitroxide radical TEMPO and its derivatives are the polarisers of choice for this type of DNP experiment and the effect of hyperfine splitting must be considered.

The importance of this issue is reflected by recent reported efforts to calculate saturation factors at the increasingly more common high field strengths (3.4 T and 9.2 T) employed in liquid DNP experiments [157, 155]. The current state of uncertainty of s at high fields in particular has led some authors to circumvent the problem when extracting coupling factors by making comparisons of distinguishable protons on either the same molecule [42] or different molecules within the same sample (see Sections 6.1.2, 6.2.2 and 6.3.2 of Chapter 6 and Reference [98]), for which s is identical and can therefore be eliminated from the analysis.

The issue of understanding the effect on DNP of strong hyperfine coupling in the radical has been a matter of much debate, with a lack of direct experimental approaches until recent pulsed ELDOR experiments by Türke et al. [95] [31] [157].

In this chapter, the possibility of increasing the saturation (and therefore overall enhancement) in DNP experiments by simultaneously irradiating two hyperfine lines is explored. To the author's knowledge, this type of dual irradiation experiment has only been reported once at the lower microwave frequency of 9.7 GHz [13]. Two samples were prepared with different nitroxide radicals to compare the effect of having two and three hyperfine lines on the overall saturation; the results of each sample will be considered in turn.

7.2 Experimental details

7.2.1 Samples

Two nitroxide radicals were used in this study: 4-oxo-TEMPO-d_{16}-^{15}N and TEMPOL, which have EPR spectra with two and three hyperfine lines, respectively. The radicals were dissolved in toluene (Figure 7.1) and the DNP enhancement of the ring and methyl protons were observed. The use of toluene as the solvent allowed larger sample volumes than with water due to its low dielectric loss, enabling much shorter experiment times of typically a few seconds. Both samples were flame-sealed in quartz capillaries of 0.7/0.87 mm ID/OD, with sample lengths of 13 mm and 11 mm for the solutions of 5 mM 4-oxo-TEMPO-d_{16}-^{15}N-toluene and 2.5 mM TEMPOL-toluene, respectively.

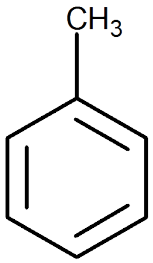

Figure 7.1: Skeletal formula of toluene ($C_6H_5CH_3$).

7.2.2 Dual irradiation experiments

As described in detail in Chapter 4 (Section 4.7), two independent microwave sources were used simultaneously through connection to the collinear arms of a magic-T. The sum of the signals was then fed into the EIK input (see Figure 4.12). Unfortunately, direct power measurements could not be made of the amplified microwaves. For convenience, herein, the Agilent PSG signal generator will be referred to as 'Source A' and the Bruker W-band bridge as 'Source B'. Unless otherwise stated, quoted microwave powers are as measured at the magic-T output (EIK input) and will be referred to as P_{A}, P_{B} and P_{T} for Source A, Source B and total power (dual irradiation), respectively.

All experiments were conducted with continuous-wave microwave irradiation at room temperature, and all reported enhancements ε are calculated using

$$\varepsilon = \frac{I_{\mathrm{enh}} - I_0}{I_0} \tag{7.4}$$

where I_{enh} and I_0 are the integrated signal intensities of the enhanced and thermal equilibrium spectra, respectively.

7.3 4-oxo-TEMPO-d_{16}-^{15}N — two hyperfine lines

The magnetic field was set so that Source B (Bruker W-band bridge) was centred on the high frequency hyperfine line of the radical EPR spectrum. In order to determine the precise frequency of irradiation for Source A, DNP experiments were carried out at varying Source A output frequencies (with fixed power). As the frequency was incrementally increased the integrated ^{1}H NMR signal from the ring and methyl protons of toluene was recorded (Figure 7.2).

Source B was used to apply constant power ($P_{\mathrm{B}} \approx 78$ μW) pumping the transition at ν_4, giving a DNP enhancement. A secondary microwave source (A) was

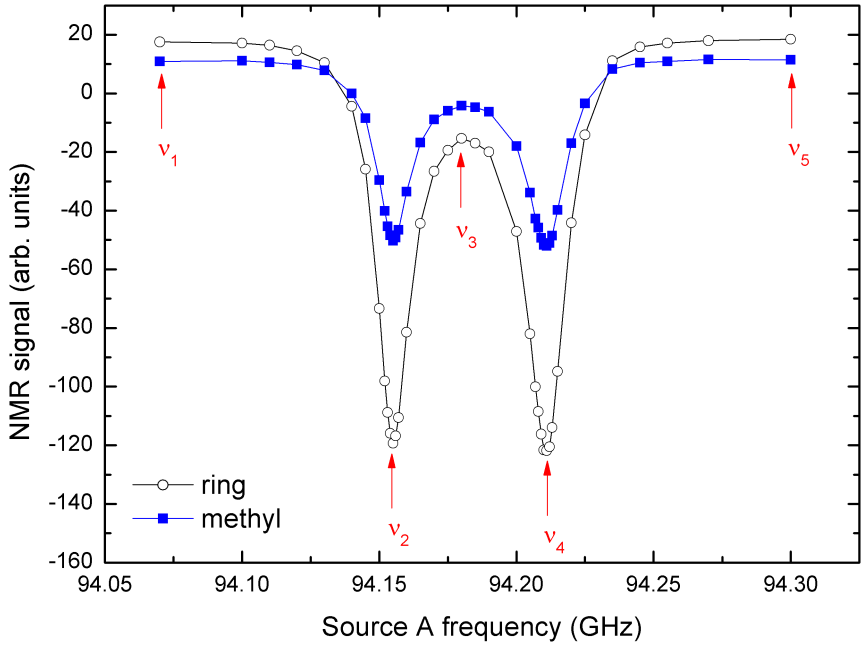

Figure 7.2: Source A frequency sweep of 5mM 4-oxo-TEMPO-d_{16}-^{15}N in toluene, used to find electron resonance frequencies at fixed magnetic field. $P_{\mathrm{A}} \approx 429$ μW, Source B off. Arrows — frequencies used in later experiments corresponding to irradiating: off-resonance (1, 5); allowed EPR transitions (2, 4); and forbidden transitions (3). $\nu_i = 94.070$, 94.155, 94.183, 94.211, 94.300 GHz; for $i = 1$, 2,... 5.

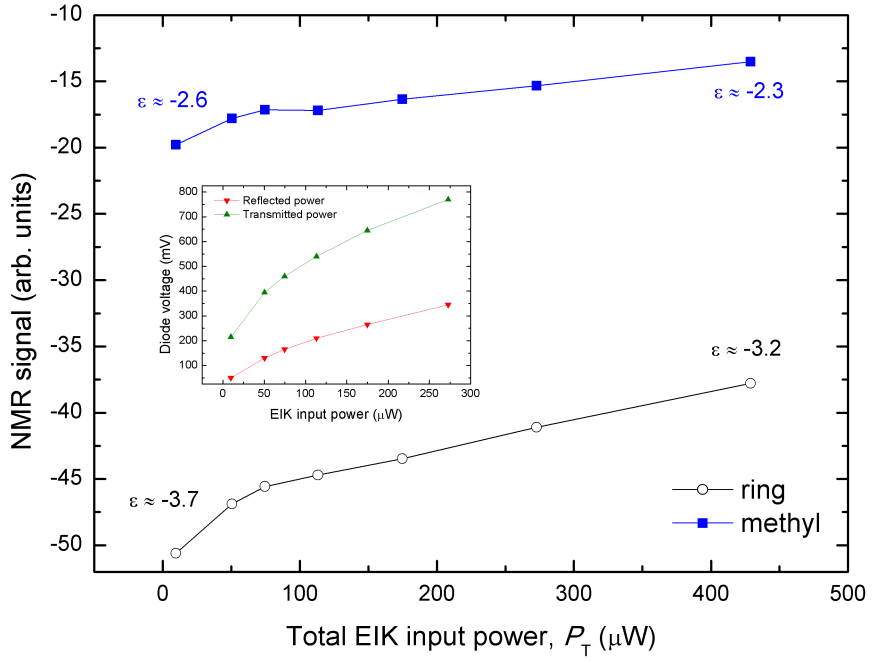

Figure 7.3: Dual irradiation experiment with Source B irradiating on-resonance at ν_4 with constant power ($P_B \approx 78$ μW), whilst simultaneously ramping Source A power ($P_A \approx$ 10–429 μW) off-resonance at ν_1. Inset — measured diode voltages indicating transmitted and reflected power.

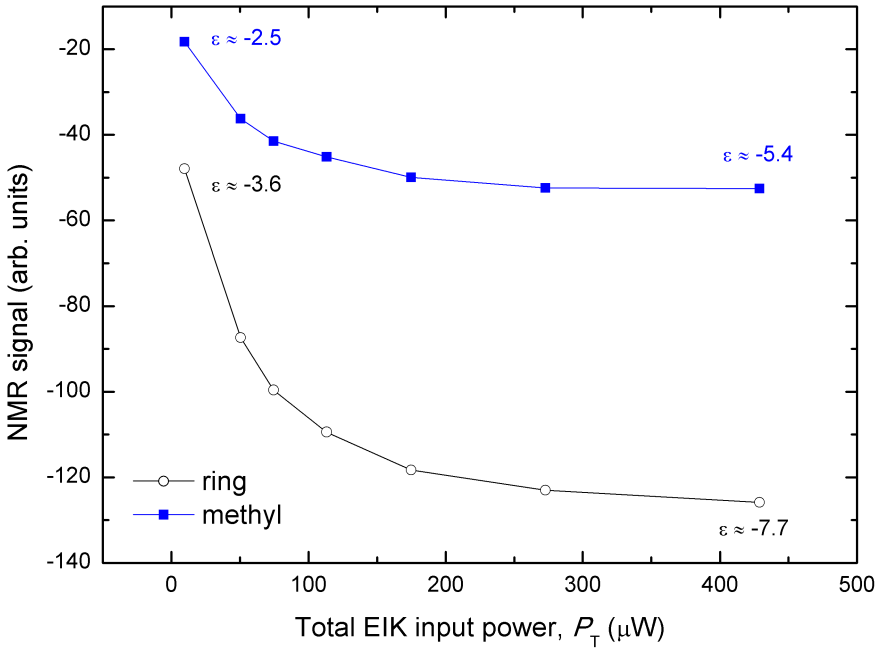

Figure 7.4: Irradiation of both hyperfine lines. Source B at ν_4 with constant power ($P_B \approx 78$ μW), ramping Source A power ($P_A \approx$ 10–429 μW) at ν_2.

then switched on to simultaneously irradiate the sample at the 5 different frequencies shown in Figure 7.2. At each frequency ν_i, DNP spectra were recorded as P_A was incrementally raised. Figures 7.3 and 7.4 show the NMR signal intensity as a function of P_A for Source A irradiating off-resonance (ν_1) and on-resonance with the lower frequency transition (ν_2), respectively. Figure 7.3 shows a decrease in enhancement of $\sim$10% in going from the minimum P_A (60 dB attenuation) to the maximum P_A (0 dB attenuation). The inset in Figure 7.3 shows the transmitted and reflected power as indicated by diode detectors positioned after the EIK. Figure 7.4 shows an increase in $|\varepsilon|$ by a factor of $\sim$2 when simultaneously irradiating both the allowed EPR transitions.

This set of 5 dual irradiation experiments was repeated with a higher 'base' power of $P_B \approx 249$ μW, giving two sets of results — a set at 'low' power and a set at 'high' power. The results are summarised in Table 7.1, with the enhancements given for minimum and maximum P_A (omitting intermediate values for simplicity). The effect of increasing the secondary microwave power P_A on the magnitude of the enhancement is indicated in the last column of the table.

From Table 7.1 it can be seen that in the low-power regime (Source B T.L. = 16.507%) irradiating with two sources on-resonance (either on the same or different transitions) causes a large increase in the enhancement by a factor of $\sim$2 for both the ring and methyl protons of toluene.

At higher microwave power (Source B T.L. = 25.787%), simultaneous irradiation of the two hyperfine lines gives rise to slightly larger enhancement ($\sim$6%), but pumping with both sources at a single frequency (ν_4) actually reduces the observed enhancement by $\sim$12%.

Irradiating with Source A either off-resonance, or at the forbidden transitions, has either no effect or in most cases has a negative impact, causing a reduction in $|\varepsilon|$.

7.4 TEMPOL — three hyperfine lines

The precise input frequency for Source A (Agilent signal generator) was determined with a similar frequency 'sweep' at constant output power to that used for the 4-oxo-TEMPO-d_{16}-^{15}N-toluene sample described in the previous section. Figure 7.5 shows the results of sweeping the frequency of Source A, with a constant low power ($P_B \approx 78$ μW) from Source B applied to the central transition ν_4. With both sources at low power, the greatest enhancement is achieved with all the power at ν_4. At these power levels, a notable asymmetry was observed with the enhancement

Source B			Source A				
Freq.	T.L. (%)	P_B (μW)	Freq.	P_A (μW)	ε_{ring}	ε_{methyl}	$\lvert\varepsilon\rvert$ change
ν_4	16.507	78	ν_1	10	-3.7	-2.6	
				429	-3.0	-2.1	$\downarrow$
			ν_2	10	**-3.6**	**-2.5**	
				429	**-7.7**	**-5.4**	$\Uparrow$ L
			ν_3	10	-3.6	-2.5	
				429	-3.1	-2.2	$\downarrow$
			ν_4	10	**-3.5**	**-2.6**	
				429	**-7.2**	**-5.0**	$\Uparrow$ L
			ν_5	10	-3.8	-2.7	
				429	-3.8	-2.6	$\leftrightarrow$
ν_4	25.787	249	ν_1	10	-7.4	-5.2	
				429	-6.5	-4.6	$\downarrow$
			ν_2	10	**-7.5**	**-5.3**	
				429	**-8.0**	**-5.6**	$\Uparrow$ S
			ν_3	10	-7.5	-5.2	
				429	-5.0	-3.5	$\downarrow$
			ν_4	10	**-7.5**	**-5.2**	
				429	**-6.6**	**-4.6**	$\Downarrow$ S
			ν_5	10	-7.5	-5.2	
				429	-7.3	-5.1	$\downarrow$

Freq. = microwave irradiation frequency (see Figure 7.2)
T.L. = Transmitter level, used to set power level of Bruker bridge

Table 7.1: Summary of dual irradiation DNP experiment results for 5 mM 4-oxo-TEMPO-d_{16}-^{15}N in toluene, showing the effect of increasing saturation of second EPR transition on ε. Experiments where all microwave power is applied on-resonance have been emphasised in the table with bold font and double arrows; 'L' and 'S' indicate 'large' and 'small' changes in enhancement, respectively (arbitrarily defined as >15% and <15%).

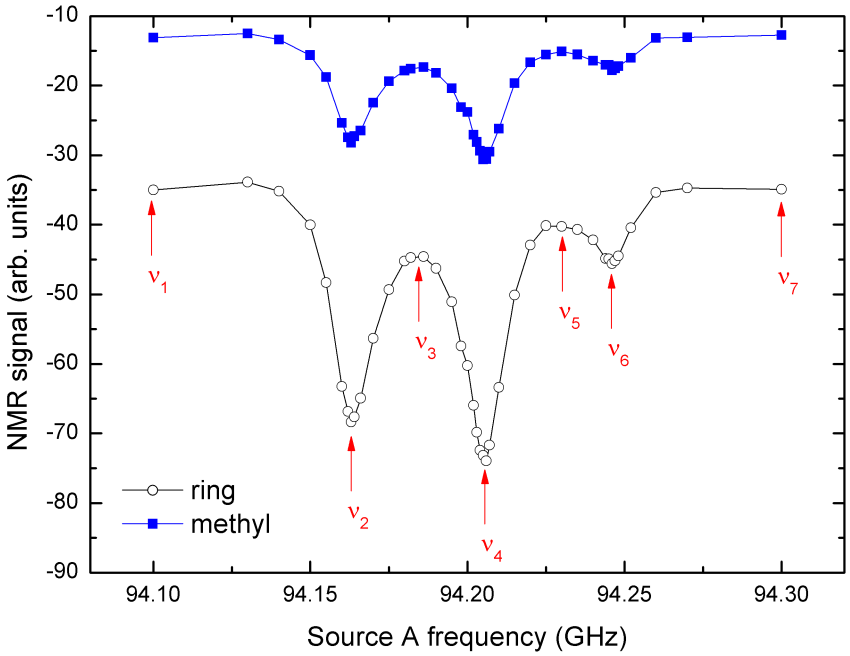

Figure 7.5: Source A frequency sweep of 2.5 mM TEMPOL in toluene, used to find electron resonance frequencies at fixed magnetic field. $P_{\mathrm{A}} \approx P_{\mathrm{B}} \approx 78$ μW. Arrows — frequencies used in later experiments corresponding to irradiating: off-resonance (1, 7); the allowed EPR transitions (2, 4, 6); and forbidden transitions (3, 5). $\nu_i =$ 94.100, 94.163, 94.185, 94.205, 94.230, 94.246, 94.300 GHz; for $i = 1, 2, \ldots 7$.

dramatically less when the second microwave source is applied at ν_6 compared to ν_2.

Figures 7.6 and 7.7 show the effect of irradiating the central transition, whilst simultaneously ramping up the secondary microwave power at ν_1 and ν_2, respectively. Off-resonance irradiation has the effect of decreasing the DNP enhancement by ∼10–15%, whilst pumping two different hyperfine lines improves the enhancement by ∼60–65%. These measurements were made at the 7 frequencies indicated in Figure 7.5, with a base power level from Source B of $P_{\mathrm{B}} = 78$ μW. The experiments were then repeated with a higher total power, setting $P_{\mathrm{B}} = 249$ μW. The results are summarised in Table 7.2.

At lower microwave powers, dual irradiation of the allowed EPR transitions was found to increase $|\varepsilon|$; with irradiation either off-resonance or at the forbidden transitions having no effect or, in one case, reducing $|\varepsilon|$. At higher microwave powers, irradiation of two different hyperfine lines gave small increases in $|\varepsilon|$; but concentrating all the available power at the central transition had no effect on the enhancement. Irradiation away from the hyperfine lines decreased the enhancement

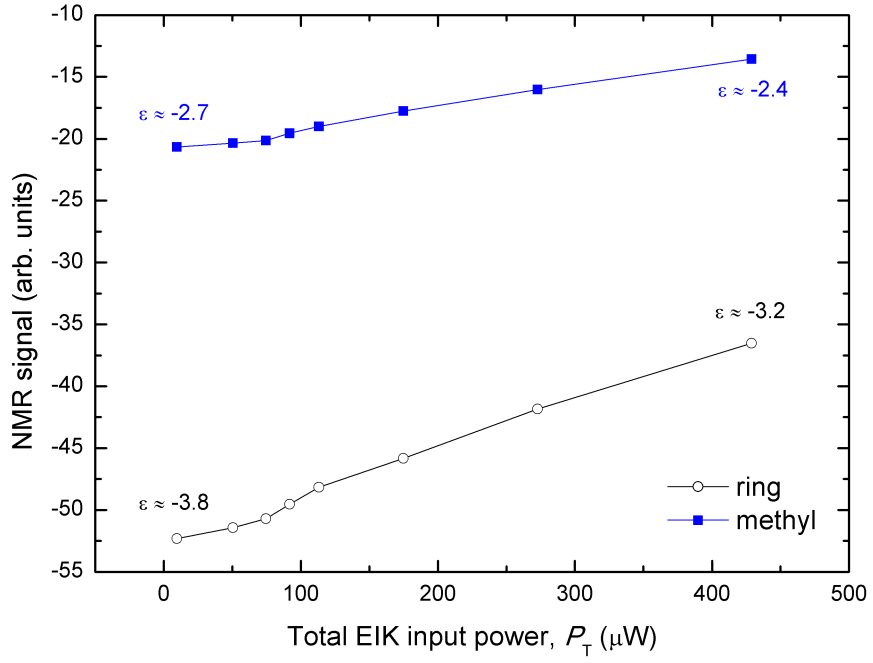

Figure 7.6: Dual irradiation experiment with Source B irradiating central transition (ν_4) with constant power ($P_B \approx 78$ μW), whilst simultaneously ramping Source A power ($P_A \approx 10$–429 μW) off-resonance at ν_1.

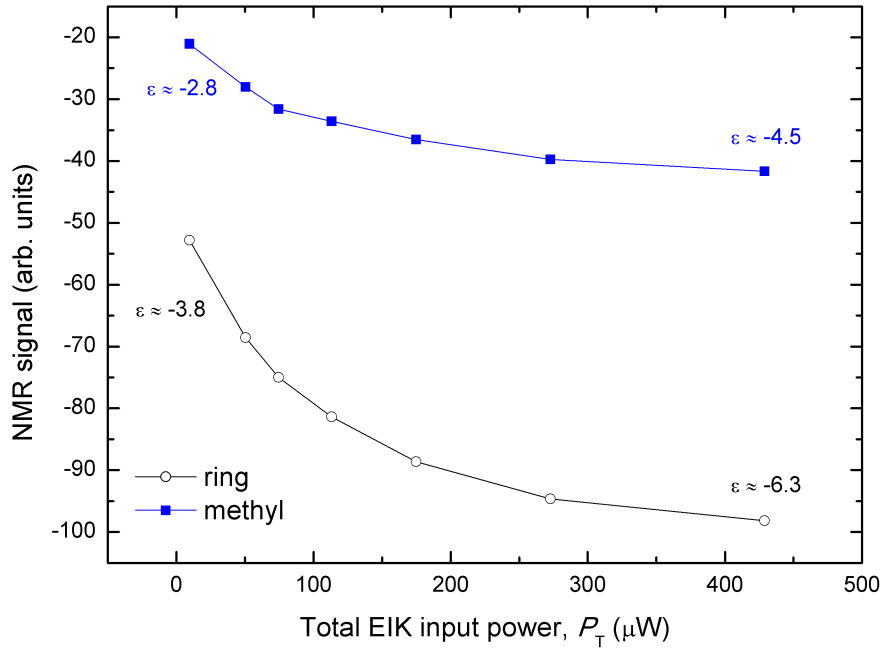

Figure 7.7: Irradiation of two hyperfine lines. Source B at central transition (ν_4) with constant power ($P_B \approx 78$ μW), ramping Source A power ($P_A \approx 10$–429 μW) at low frequency transition (ν_2).

at all of the four positions measured.

7.5 Discussion

The data presented in Sections 7.3 and 7.4 appear to show that off-resonance irradiation with a second microwave source decreases the attainable DNP enhancement. However, experiments with off-resonance irradiation using a single source were conducted and found to have either no effect or caused very small signal enhancement. In order to properly interpret the data it is important to understand the characteristics of the unique dual microwave source setup utilised.

Whilst Source A and Source B are indeed independent microwave generators and their combined power has been measured at the output of the magic-T, the output of the EIK amplifier could not be directly measured. As shown in the inset of Figure 7.3, an indication of the transmitted and reflected power can be observed using power detectors attached to directional couplers after the EIK (see Figure 4.12, Chapter 4). However, the precise output of the Schottky barrier diode-based detectors (WDP-10, Farran Technology Ltd.) with varying input power is not known and so cannot be used to determine the actual EIK output.

The observed reduction of $|\varepsilon|$ with increasing power suggests that the EIK may be saturating. In order to test this, a calibrated variable attenuator (Flann Microwave Instruments, Ltd.) was connected between the 40 dB directional coupler positioned at the EIK output and the power detector (see Figure 7.8). This attenuator was then adjusted to maintain a constant diode voltage reading as P_{A} was increased from 10 dB attenuation to 0 dB, whilst simultaneous irradiating with constant P_{B}. The attenuation required to maintain a constant EIK output for a 10 dB increase in input power was repeated for increasingly large total input powers, by increasing P_{B} (set using the bridge transmitter level). This attenuation, therefore, corresponds to the increase in EIK output for a 10 dB increase in input, and is plotted for varying P_{B} in Figure 7.9. The data show that the EIK is beginning to saturate.

It should be noted that these power measurements were made a few months after the dual irradiation DNP experiments, at which time it was discovered that the output of the Bruker W-band bridge (Source B) had significantly dropped (estimated at ∼85–90%). This was compensated for by setting the transmitter level higher to achieve the same power as previously used (as judged by the diode voltage). The transmitter levels corresponding to those used for the dual irradiation experiments are labelled on the plot, i.e. 16.507% and 25.787%. At a P_{B} corresponding to

Source B			Source A				
Freq.	T.L. (%)	P_B (μW)	Freq.	P_A (μW)	ε_{ring}	ε_{methyl}	$\lvert\varepsilon\rvert$ change
ν_4	16.507	78	ν_1	10	-3.8	-2.7	
				429	-3.0	-2.1	$\downarrow$
			ν_2	10	**-3.8**	**-2.8**	
				429	**-6.3**	**-4.5**	$\Uparrow$ L
			ν_3	10	-3.8	-2.7	
				429	-3.6	-2.7	$\leftrightarrow$
			ν_4	10	**-3.7**	**-2.7**	
				429	**-6.7**	**-4.8**	$\Uparrow$ L
			ν_5	10	-3.8	-2.7	
				429	-3.9	-2.8	$\leftrightarrow$
			ν_6	10	**-3.8**	**-2.7**	
				429	**-6.4**	**-4.6**	$\Uparrow$ L
			ν_7	10	-3.8	-2.7	
				429	-3.6	-2.6	$\leftrightarrow$
ν_4	25.787	249	ν_1	10	-6.3	-4.5	
				429	-5.4	-3.9	$\downarrow$
			ν_2	10	**-6.3**	**-4.5**	
				429	**-6.6**	**-4.8**	$\Uparrow$ S
			ν_3	10	-6.4	-4.7	
				429	-5.2	-3.8	$\downarrow$
			ν_4	10	**-6.4**	**-4.7**	
				429	**-6.3**	**-4.7**	$\Leftrightarrow$
			ν_5	10	-6.5	-4.8	
				429	-5.2	-3.8	$\downarrow$
			ν_6	10	**-6.4**	**-4.7**	
				429	**-6.8**	**-4.9**	$\Uparrow$ S
			ν_7	10	-6.5	-4.7	
				429	-6.2	-4.5	$\downarrow$

Freq. = microwave irradiation frequency (see Figure 7.5)
T.L. = Transmitter level, used to set power level of Bruker bridge

Table 7.2: Summary of dual irradiation DNP experiment results for 2.5 mM TEMPOL in toluene, showing the effect of increasing saturation of a second EPR transition on ε. Experiments with Source B and A irradiating allowed EPR transitions are highlighted with enhancements in bold and enhancement change represented by double arrows; 'L' and 'S' indicate 'large' and 'small' changes in enhancement, respectively (arbitrarily defined as >15% and <15%).

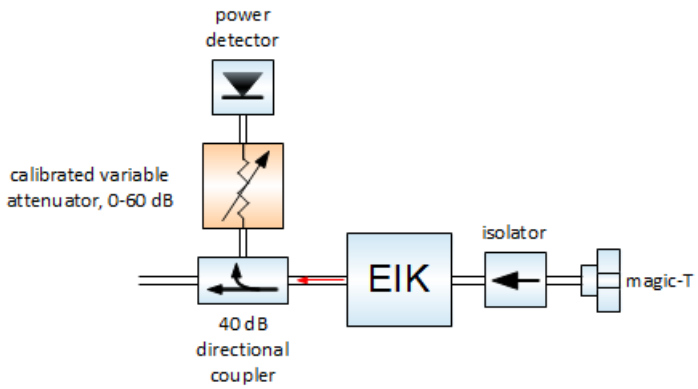

Figure 7.8: Schematic of part of the microwave assembly, showing the addition of a calibrated variable attenuator used to measure relative output powers of the EIK, cf. Figure 4.12.

16.507%, a further 10 dB EIK power input increase provides only an additional 5.2 dB output power; and for 25.787%, only a 3.5 dB power increase is obtained.

This saturation of the amplifier is unexpected as the maximum input power used was ∼680 μW, whilst the manufacturer specifications state that the power required to drive the amplifier to saturation is 10 mW.

A further consideration for analysing the enhancements obtained is the bandwidth of the amplifier and that, due to the strong hyperfine coupling in the radicals, the allowed EPR transitions were separated by ∼40 and ∼55 MHz for TEMPO and 4-oxo-TEMPO-d_{16}-^{15}N, respectively. The forward power from the EIK was monitored and recorded during a frequency sweep of Source A using the diode detector at the 40 dB directional coupler (Figure 7.10). This gives an estimate of the frequency dependent characteristics of the amplifier at input powers relevant to these experiments. The resonant frequencies of the allowed EPR transitions of the radicals used in this study have been plotted on the curve. Unfortunately, it is not possible to be fully quantitative about the differences in applied microwave power at these frequencies since the behaviour of the detector diode is unknown. However, this at least demonstrates that for a given input power P_{T}, the applied microwave power from the amplifier is greater at the lower frequency transitions.

In light of these power measurements, the data from the dual irradiation experiments reported in Tables 7.1 and 7.2 can be rationalised. The reduction of the measured DNP enhancements with increasing secondary source (Source A) power centred at frequencies away from the allowed transitions is most likely due to saturation of the EIK amplifier. It is possible that as P_{A} is increased, the EIK approaches saturation and power originally at the Source B frequency (always set

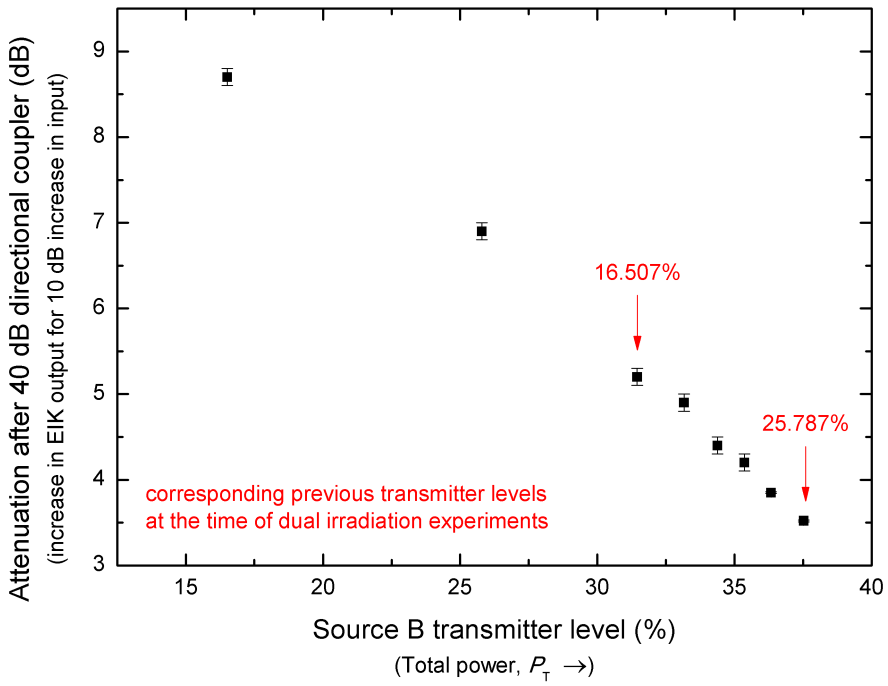

Figure 7.9: Change in EIK output power corresponding to a 10 dB increase in input power, for varying levels of total power. As measured using a calibrated variable attenuator and diode power detector.

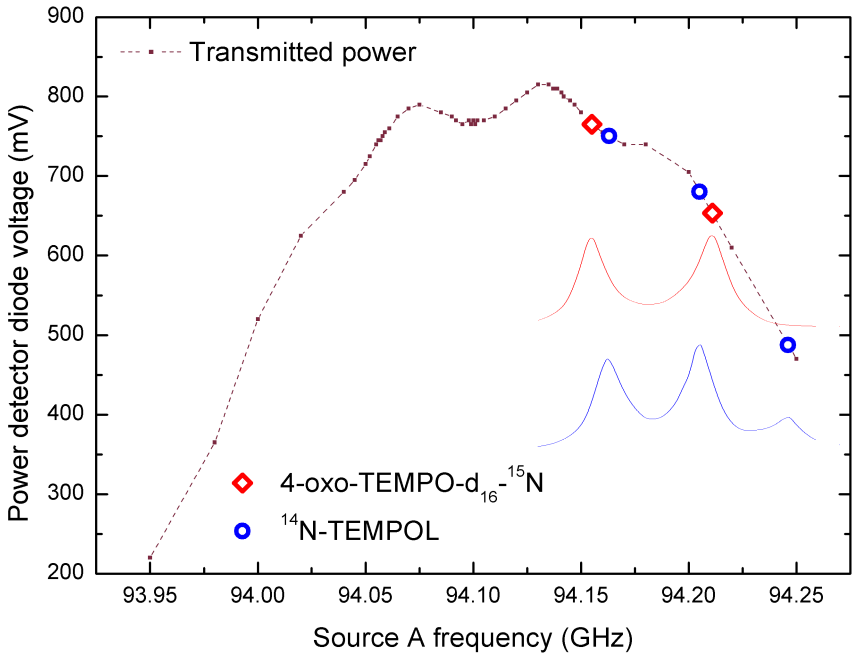

Figure 7.10: Frequency dependence of EIK amplifier output. Measured with single microwave source (Source A) using constant power $P_A \approx 429$ μW. Frequency of allowed EPR transitions for two TEMPO-derived radicals are shown.

to be resonant with an allowed transition) eventually reduces thereby reducing $|\varepsilon|$.

Off-resonance irradiation was found to reduce $|\varepsilon|$ at all measured frequencies in the high power regime (Source B transmitter level = 25.787%) for both radicals; and found to have either no effect at higher microwave frequencies or to again reduce $|\varepsilon|$ at lower frequencies in the low power regime (Source B transmitter level = 16.507%). This is consistent with the hypothesis of amplifier saturation, since from Figure 7.10 we see that greater microwave power is supplied by the EIK at the lower frequencies.

For the ^{15}N-doped sample with two hyperfine EPR lines, an increase in enhancement was observed in both the low and high power regimes when simultaneously irradiating the two lines rather than one. However, due to the way the experiment was set up with Source B at ν_4, it is possible that greater $|\varepsilon|$ is achieved because applying the microwaves at ν_2 gives greater total power since it is at a lower field (cf. Figure 7.10). Although, for the ^{14}N-TEMPOL sample with three hyperfine lines, improvements in enhancement are observed when the secondary source is pumping either the resonance higher or lower in frequency than the central transition where the primary source is irradiating. This suggests that the effect is really coming from increased effective saturation from pumping two lines and not just caused by differences in total applied power.

The larger enhancement achieved with Source A at ν_6 (and Source B at ν_4) provides indirect evidence of the fact that in the high power regime, the central transition has been driven to full saturation when both sources are applied at ν_4; since there is greater power, but less enhancement with Source A centred at the higher frequency ν_4.

7.6 Conclusions

A new experimental setup has been used to successfully irradiate two EPR lines simultaneously at W-band. This was achieved by connecting two independent microwave sources to a single amplifier via a magic-T. Despite some initial difficulty in understanding the results due to unexpected saturation of the amplifier at the higher input powers used, larger DNP enhancements have been attained using this dual irradiation method, which are attributed to an increase in the effective saturation factor.

This result is in contrast to a similar dual irradiation study reported several years ago at X-band, where no improvement to the saturation factor (and therefore ε) was observed [13].

These improvements, however, are somewhat small when using higher microwave powers, with an observed increase of $\sim$10% in the enhancement of ring protons in toluene. At lower total microwave powers, considerable increases in enhancement of $>$65% are measured. The possibility to increase the attainable DNP enhancement by improving saturation with two microwave sources may find applications in situations where available power is limited or with samples which are very temperature sensitive. However, it is likely that the technical challenges and expense will outweigh the benefits in most common liquid DNP applications.

Chapter 8

Summary and conclusions

Various different methods for DNP exist, depending on the type and purpose of the experiment, e.g. whether solids or liquids are being studied. Liquid DNP utilising direct in-situ polarisation — which is the topic of this thesis — has several advantages over other procedures, prime among them being that it allows the examination of biomolecules under biological and physiological conditions, i.e. in solution-state, at approximately room or body temperature. However, in order for this technique to be truly useful, it must be efficient at high field strengths. Currently, the extent of its applicability and its value in comparison to 'standard' high-field NMR is still in question. Fortunately, contemporary results seem to be painting an optimistic picture for the future of liquid DNP, and the work reported here contributes further to that positive outlook.

As the preferred solvent for biomolecules, understanding the DNP enhancement of water is important and has been studied extensively over the last several years [13, 97, 95, 96, 40]. This system, however, can be somewhat challenging to investigate at high fields (here, defined arbitrarily as $\geq$3.4 T) due to the high dielectric loss in water at the corresponding high microwave frequencies required for electron spin saturation — this results in significant sample heating. A resonant cavity was employed to minimise the electric field component (and hence, the heating) at the sample, though this necessitated a very short ($\sim$2 mm) sample length to reduce temperature gradients in the sample. Using this setup, a method has been demonstrated for determining the maximum DNP enhancement as a function of temperature at high field. This required knowledge of the temperature dependence of the nuclear spin-lattice relaxation as well as characterisation of the temperature build-up with time; these measurements were enabled by the observation of the change in the water proton chemical shift. In addition, the high radical concentrations used resulted

in a leakage and saturation factor of ≈1, which facilitated the calculation of coupling factor values. These ξ were found to be in good agreement with theoretical values predicted by MD simulations [40] at room temperature, but slightly higher at increased temperatures. Overall, high enhancements were achieved ($|\varepsilon| \gg 100$) at elevated temperatures, but it was also demonstrated that substantial enhancements could still be attained at more modest temperatures, e.g. $\varepsilon \sim -40$ at 40°C.

A natural extension of the water study was to explore Overhauser DNP on organic compounds dissolved in water and investigate the efficiency of the process. As previously mentioned, the application of liquid DNP to biomolecules is one of the primary objectives of the field; however, the preponderance of work at high fields has been on solvent molecules (the notable exception being Reference [98]). Here, liquid DNP enhancements of solute molecules dissolved in water have been reported at 3.4 T. To the author's knowledge, this is the first report of successful solute polarisation in liquid DNP at this field strength. The temperature dependence of the enhancement for the compounds studied show that significant gains in sensitivity can be made even at ∼40°C, with $\varepsilon \approx -17, -16$ and -11 for glycine, L-proline and acrylic acid protons, respectively. These target molecules are several times larger than water, which is encouraging since coupling to the electron spin is expected to be poorer for larger molecules as the distance of closest approach increases. The DNP efficiency for larger solute molecules is, therefore, expected to diminish; however, the severity of this decrease and the limitations it imposes is not clear. A comparison was made of coupling factor ratios ($\gamma_{\text{water}}/\gamma_{\text{target}}$) extracted from experimental results and those theoretically predicted by a FFHS model. The experimental values were consistently found to be greater than the theoretical values. This provides further evidence, to that already in the literature, that the conventional analytical models so often used in the analysis of liquid DNP experiments may no longer be appropriate at high magnetic fields.

A new experimental setup — with two independent microwave sources — was used to enable the simultaneous continuous-wave irradiation of two hyperfine lines of the nitroxide radical EPR spectrum. Direct pumping of multiple EPR resonances was found to be advantageous compared to the usual single line irradiation, which relies on processes such as spin-exchange and nuclear relaxation to achieve saturation beyond $s = 1/n$, where n is the number of hyperfine lines. This method was shown to increase the magnitude of the DNP enhancement by increasing the electron spin saturation. Fairly small improvements were observed (in contrast to Reference [13]), ∼10% at high powers in this system; but at low microwave powers, enhancements increased by a factor of ∼2. It seems unlikely that this will become a favourable

setup for most liquid DNP experiments due to the costs and technical challenges for relatively low return in terms of sensitivity enhancement in some cases. However, confirmation of the feasibility of dual irradiation is important as it may prove useful in applications where power is limited or the sample under study is highly sensitive to temperature.

The studies presented in this thesis add to the growing body of work in high-field liquid DNP demonstrating the viability of the Overhauser effect at frequencies that were previously thought to be impractical. Whilst the study of dissolved organic molecules demonstrates significant enhancements, further optimisation of the experiment should yield even higher values. Long ($\sim$10 mm) samples were used which, as mentioned in Chapter 5, result in broader lines and lower average enhancement due to sample regions outside of the cavity that are not irradiated but still constitute part of the NMR signal. Shorter samples were not made up for the organic compound investigation due to the technical difficulties in cutting, injecting and sealing (without air bubbles) $\sim$2 mm lengths of 0.1/0.4 mm (ID/OD) capillary tubes. This is, however, possible (as demonstrated in Chapter 5) and may be simpler if a different sample preparation method is adopted. The Kentgens group [133] recently used the proton-free compound Fluorinert® FC-40 to 'sandwich' a sample in a capillary. This same method using liquid sample 'plugs' should allow easier preparation of short sample lengths, and therefore higher DNP enhancements with slightly narrower lines. Further maximisation of the enhancement could be achieved using the dual irradiation method. Once the optimal enhancement factors were reached with the samples already measured, a systematic study of larger and larger biomolecules would give greater insight into the efficiency and the potential of solution-state Overhauser DNP at high field.

Bibliography

[1] "Albert W. Overhauser." http://www.physics.purdue.edu, viewed 26 February 2013.

[2] A. W. Overhauser, "Polarization of nuclei in metals," *Physical Review*, vol. 92, pp. 411–415, 1953.

[3] T. Carver and C. P. Slichter, "Polarization of nuclear spins in metals," *Physical Review*, vol. 92, pp. 212–213, 1953.

[4] T. Carver and C. P. Slichter, "Experimental verification of the Overhauser nuclear polarization effect," *Physical Review*, vol. 102, pp. 975–981, 1956.

[5] K. H. Hausser, "Bestimmung der hochfeldgrenze der dynamischen kernpolarisation aus der dispersion der kernrelaxation," *Zeitschrift fuer Physik*, vol. 183, pp. 265–273, 1965.

[6] K. H. Hausser and D. Stehlik, "Dynamic nuclear polarization in liquids," *Advanced Magnetic Resonance*, vol. 3, pp. 79–139, 1968.

[7] W. D. Rooney, G. Johnson, X. Li, E. R. Cohen, S.-G. Kim, K. Ugurbil, and C. S. Springer Jr, "Magnetic field and tissue dependencies of human brain longitudinal ^1H_2O relaxation in vivo," *Magnetic Resonance in Medicine*, vol. 57, pp. 308–318, 2007.

[8] P. Noonan, "1 GHz and beyond: Challenges in high-field NMR magnets." http://www.spinsights.net/2011/03/1-ghz-and-beyond-challenges-in-high-field-nmr-magnets/, March 2011.

[9] L. R. Becerra, G. J. Gerfen, R. J. Temkin, D. J. Singel, and R. G. Griffin, "Dynamic nuclear polarization with a cyclotron resonance maser at 5 T," *Physical Review Letters*, vol. 71, pp. 3561–3564, 1993.

[10] N. M. Loening, M. Rosay, V. Weis, and R. G. Griffin, "Solution-state dynamic nuclear polarization at high magnetic field," *Journal of the American Chemical Society*, vol. 124, pp. 8808–8809, July 2002.

[11] M. J. Prandolini, V. P. Denysenkov, M. Gafurov, S. Lyubenova, B. Endeward, M. Bennati, and T. F. Prisner, "First DNP results from a liquid water-TEMPOL sample at 400 MHz and 260 GHz," *Applied Magnetic Resonance*, vol. 34, pp. 399–407, Aug. 2008.

[12] V. Denysenkov, M. J. Prandolini, M. Gafurov, D. Sezer, B. Endeward, and T. F. Prisner, "Liquid state DNP using a 260 GHz high power gyrotron," *Physical Chemistry Chemical Physics*, vol. 12, no. 22, pp. 5786–5790, 2010.

[13] P. Hoefer, P. Carl, G. Guthausen, T. Prisner, M. Reese, T. Carlomagno, C. Griesinger, and M. Bennati, "Studies of dynamic nuclear polarization with nitroxides in aqueous solution," *Applied Magnetic Resonance*, vol. 34, pp. 393–398, 2008.

[14] F. Bloch, W. W. Hansen, and M. Packard, "Nuclear induction," *Physical Review*, vol. 69, p. 127, 1946.

[15] E. M. Purcell, H. C. Torrey, and R. V. Pound, "Resonance absorption by nuclear magnetic moments in a solid," *Physical Review*, vol. 69, pp. 37–38, 1946.

[16] M. Levitt, *Spin Dynamics: Basics of Nuclear Magnetic Resonance*. John Wiley & Sons Ltd, 2008.

[17] J. MacKenzie and M. Smith, *Multinuclear Solid-State NMR of Inorganic Materials*. Pergamon, 2002.

[18] P. Hore, *Nuclear Magnetic Resonance*. Oxford University Press, 1995.

[19] B. Cowan, *Nuclear Magnetic Resonance and Relaxation*. Cambridge University Press, 2005.

[20] A. Abragam, *Principles of Nuclear Magnetism*. Oxford University Press, 1961.

[21] J. W. Hennel and J. Klinowski, *Fundamentals of Nuclear Magnetic Resonance*. Longman Scientific & Technical, 1993.

[22] R. Freeman, *A Handbook of Nuclear Magnetic Resonance*. Longman Scientific & Technical, 1988.

[23] N. Bloembergen, *Nuclear Magnetic Relaxation.* W. A. Benjamin, Inc., 1961.

[24] C. D. Jeffries, *Dynamic Nuclear Orientation.* John Wiley & Sons, Inc., 1963.

[25] E. Zavoisky, "Spin-magnetic resonance in paramagnetics," *Journal of Physics USSR*, vol. 9, p. 245, 1945.

[26] J. Weil, J. Bolton, and J. Wertz, *Electron Paramagnetic Resonance: Elementary Theory and Practical Applications.* John Wiley & Sons, Inc., 1994.

[27] M. Brustolon and E. Giamello, eds., *Electron Paramagnetic Resonance: A Practitioner's Toolkit.* John Wiley & Sons, Inc., 2009.

[28] G. E. Pake and T. L. Estle, *The Physical Principles of Electron Paramagnetic Resonance.* W. A. Benjamin, Inc., 1973.

[29] N. M. Atherton, *Principles of Electron Spin Resonance.* Ellis Horwood Limited, 1993.

[30] R. A. Wind, M. J. Duijvestijn, C. van der Lugt, A. Manenschijn, and J. Vriend, "Applications of dynamic nuclear polarization in ^{13}C NMR in solids," *Progress In Nuclear Magnetic Resonance Spectroscopy*, vol. 17, pp. 33–67, 1985.

[31] M.-T. Tuerke and M. Bennati, "Saturation factor of nitroxide radicals in liquid DNP by pulsed ELDOR experiments," *Physical Chemistry Chemical Physics*, vol. 13, no. 9, pp. 3630–3633, 2011.

[32] E. A. Nasibulov, K. L. Ivanov, A. V. Yurkovskaya, and H.-M. Vieth, "Theory of the Overhauser effect in the pulsed mode of EPR pumping: exploiting the advantages of coherent electron spin motion," *Physical Chemistry Chemical Physics*, vol. 14, no. 18, pp. 6459–6468, 2012.

[33] M. Bennati, I. Tkach, and M.-T. Tuerke, "Dynamic nuclear polarization in liquids," *Electron Paramagnetic Resonance*, vol. 22, pp. 155–182, 2011.

[34] I. Solomon, "Relaxation processes in a system of two spins," *Physical Review*, vol. 99, pp. 559–566, 1955.

[35] U. L. Guenther, *Dynamic Nuclear Hyperpolarization in Liquids.* Topics in Current Chemistry, Springer Berlin Heidelberg, 2011.

[36] C. Griesinger, M. Bennati, H. M. Vieth, C. Luchinat, G. Parigi, P. Hoefer, F. Engelke, S. J. Glaser, V. Denysenkov, and T. F. Prisner, "Dynamic nuclear

polarization at high magnetic fields in liquids," *Progress In Nuclear Magnetic Resonance Spectroscopy*, vol. 64, pp. 4–28, July 2012.

[37] M. D. Lingwood and S. Han, "Solution-state dynamic nuclear polarization," *Annual Reports On NMR Spectroscopy*, vol. 73, pp. 83–126, 2011.

[38] B. D. Armstrong and S. Han, "Overhauser dynamic nuclear polarization to study local water dynamics," *Journal of the American Chemical Society*, vol. 131, pp. 4641–4647, Apr. 2009.

[39] L. P. Hwang and J. H. Freed, "Dynamic effects of pair correlation functions on spin relaxation by translational diffusion in liquids," *Journal of Chemical Physics*, vol. 63, p. 4017, 1975.

[40] D. Sezer, M. J. Prandolini, and T. F. Prisner, "Dynamic nuclear polarization coupling factors calculated from molecular dynamics simulations of a nitroxide radical in water," *Physical Chemistry Chemical Physics*, vol. 11, no. 31, pp. 6626–6637, 2009.

[41] M. Pavone, P. Cimino, O. Crescenzi, A. Sillanpaa, and V. Barone, "Interplay of intrinsic, environmental, and dynamical effects in tuning the EPR parameters of nitroxides: Further insights from an integrated computational approach," *Journal of Chemical Physics B*, vol. 111, pp. 8928–8939, 2007.

[42] D. Sezer, "Computation of DNP coupling factors of nitroxide radical in toluene: seamless combination of MD simulations and analytical calculations," *Phys. Chem. Chem. Phys.*, vol. 15, pp. 526–540, 2013.

[43] E. V. Kryukov, M. E. Newton, K. J. Pike, D. R. Bolton, R. M. Kowalczyk, A. P. Howes, M. E. Smith, and R. Dupree, "DNP enhanced NMR using a high-power 94 GHz microwave source: a study of the TEMPOL radical in toluene," *Physical Chemistry Chemical Physics*, vol. 12, no. 22, pp. 5757–5765, 2010.

[44] *Physical Chemistry Chemical Physics [Themed Issue: Dynamic nuclear polarization]*, vol. 12, no. 22, pp. 5725–5928, 2010.

[45] V. A. Atsarkin and W. Koeckenberger, "The different magnetic resonance communities join forces for progress in DNP," *Applied Magnetic Resonance*, vol. 43, July 2012.

[46] H. Ward and R. Lawler, "Nuclear magnetic resonance emission and enhanced absorption in rapid organometallic reactions," *Journal of the American Chemical Society*, vol. 89, pp. 5518–5519, 1967.

[47] J. Bargon, "The discovery of chemically induced dynamic polarization (CIDNP)," *Helvetica Chimica Acta*, vol. 89, pp. 2082–2102, 2006.

[48] E. Daviso, G. Jeschke, and J. Matysik, "Photochemically induced dynamic nuclear polarization (photo-CIDNP) magic-angle spinning NMR," in *Biophysical Techniques in Photosynthesis* (T. Aartsma and J. Matysik, eds.), vol. 26 of *Advances in Photosynthesis and Respiration*, ch. 19, Springer Netherlands, 2008.

[49] M. Goez, "Photo-CIDNP spectroscopy," *Annual Reports on NMR Spectroscopy*, vol. 66, pp. 77–147, 2009.

[50] C. Bowers, D. Jones, N. Kurur, J. Labinger, M. Pravica, and D. Wieitekamp, "Symmetrization postulate and nuclear magnetic resonance of reacting systems," *Advances in Magnetic Resonance*, vol. 14, pp. 269–291, 1990.

[51] J. Bargon, J. Kandels, and K. Woelk, "Ortho- and parahydrogen induced nuclear spin polarization," *Zeitschrift fuer Physikalische Chemie*, vol. 180, pp. 65–93, 1993.

[52] J. Natterer and J. Bargon, "Parahydrogen induced polarization," *Progress In Nuclear Magnetic Resonance Spectroscopy*, vol. 31, pp. 293–315, 1997.

[53] G. Lampel, "Nuclear dynamic polarization by optical electronic saturation and optical pumping in semiconductors," *Physical Review Letters*, vol. 20, pp. 491–493, 1968.

[54] M. Albert, G. Cates, B. Driehuys, W. Happer, B. Saam, C. Springer Jr, and A. Wishnia, "Biological magnetic resonance imaging using laser-polarized 129Xe," *Nature*, vol. 370, pp. 199–201, 1994.

[55] G. Navon, Y.-Q. Song, T. Room, S. Appelt, R. Taylor, and A. Pines, "Enhancement of solution NMR and MRI with laser-polarized xenon," *Science*, vol. 271, pp. 1848–1851, 1996.

[56] A. Bifone, Y.-Q. Song, R. Seydoux, R. Taylor, B. Goodson, T. Pietrass, T. Budinger, G. Navon, and A. Pines, "NMR of laser-polarized xenon in human blood," *Proceedings of the National Academy of Sciences of the United States of America*, vol. 93, pp. 12932–12936, 1996.

[57] N. Bloembergen, "Retrospective comments on magnetic resonance and relaxation," *Concepts in Magnetic Resonance*, vol. 6, pp. 185–192, 1994.

[58] C. P. Slichter, "The discovery and demonstration of dynamic nuclear polarization — a personal and historical account," *Physical Chemistry Chemical Physics*, vol. 12, no. 22, pp. 5741–5751, 2010.

[59] H. Beljers, L. van der Kint, and J. van Wieringen, "Overhauser effect in a free radical," *Physical Review*, vol. 95, p. 1683, 1954.

[60] L. Bennett and H. Torrey, "High negative nuclear polarizations in a liquid," *Physical Review*, vol. 108, pp. 499–500, 1957.

[61] K. H. Hausser and F. Reinbold, "Dynamic polarisation in a three-spin system," *Physics Letters*, vol. 2, pp. 53–54, 1962.

[62] R. Richards and J. White, "Relative couplings between free radicals and hydrogen and fluorine nuclei by the Overhauser effect," *Proceedings of the Chemical Society*, pp. 119–120, March 1962.

[63] R. Dwek and R. Richards, "Dynamic polarisation of phosphorus-31 nuclei at 12,500 Gauss," *Chemical Communications*, vol. 3, pp. 581–582, 1966.

[64] W. Mueller-Warmuth and K. Meise-Gresch, "Molecular motions and interactions as studied by dynamic nuclear-polarization (DNP) in free-radical solutions," *Advances in Magnetic Resonance*, vol. 11, pp. 1–45, 1983.

[65] G. Krueger, W. Mueller-Warmuth, and R. van Steenwinkel, "Molecular motion in liquids and solutions. II. Dynamic nuclear polarization and nuclear magnetic relaxation in free radical solutions of toluene," *Zeitschrift Naturforschung*, vol. 21a, p. 1224, 1966.

[66] C. Jeffries, "Polarization of nuclei by resonance saturation in paramagnetic crystals," *Physical Review*, vol. 106, pp. 164–165, 1957.

[67] C. Jeffries, "Dynamic orientation of nuclei by forbidden transitions in paramagnetic resonance," *Physical Review*, vol. 117, pp. 1056–1069, 1960.

[68] M. Goldman, *Spin temperature and nuclear magnetic resonance in solids.* Clarendon Press, 1970.

[69] A. Abragam and M. Goldman, "Principles of dynamic nuclear polarisation," *Reports on Progress in Physics*, vol. 41, pp. 395–467, 1978.

[70] A. Kessenikh, V. Lushchikov, A. Manenkov, and Y. V. Taran, "Proton polarization in irradiated polyethylenes," *Soviet Physics - Solid State*, vol. 5, pp. 321–329, 1963.

[71] A. Kessenikh, A. Manenkov, and G. Pyatnitskii, "On explanation of experimental data on dynamic polarization of protons in irradiated polyethylenes," *Soviet Physics - Solid State*, vol. 6, pp. 641–643, 1964.

[72] C. Hwang and D. Hill, "New effect in dynamic polarization," *Physical Review Letters*, vol. 18, pp. 110–112, 1967.

[73] C. Hwang and D. Hill, "Phenomenological model for the new effect in dynamic polarization," *Physical Review Letters*, vol. 19, pp. 1011–1014, 1967.

[74] D. Wollan, "Dynamic nuclear polarization with an inhomogeneously broadened ESR line. I. Theory," *Physical Review B*, vol. 13, pp. 3671–3685, 1976.

[75] D. Wollan, "Dynamic nuclear polarization with an inhomogeneously broadened ESR line. II. Experiment," *Physical Review B*, vol. 13, pp. 3686–3696, 1976.

[76] V. A. Atsarkin, "Dynamic polarization of nuclei in solid dielectrics," *Soviet Physics Uspekhi*, vol. 21, pp. 725–745, 1978.

[77] S. Un, T. Prisner, R. T. Weber, M. J. Seaman, K. W. Fishbein, A. E. McDermott, D. J. Singel, and R. G. Griffin, "Pulsed dynamic nuclear polarization at 5 T," *Chemical Physics Letters*, vol. 189, pp. 54–59, Jan. 1992.

[78] L. R. Becerra, G. J. Gerfen, B. F. Bellew, J. A. Bryant, D. A. Hall, S. J. Inati, R. T. Weber, S. Un, T. F. Prisner, A. E. McDermott, K. W. Fishbein, K. E. Kreischer, R. J. Temkin, D. J. Singel, and R. G. Griffin, "A spectrometer for dynamic nuclear polarization and electron paramagnetic resonance at high frequencies," *Journal of Magnetic Resonance Series A*, vol. 117, pp. 28–40, 1995.

[79] V. S. Bajaj, C. T. Farrar, M. K. Hornstein, I. Mastovsky, J. Vierigg, J. Bryant, B. Elena, K. E. Kreischer, R. J. Temkin, and R. G. Griffin, "Dynamic nuclear polarization at 9 T using a novel 250 GHz gyrotron microwave source," *Journal of Magnetic Resonance*, vol. 160, pp. 85–90, 2003.

[80] A. B. Barnes, E. Markhasin, E. Daviso, V. K. Michaelis, E. A. Nanni, S. K. Jawla, E. L. Mena, R. DeRocher, A. Thakkar, P. P. Woskov, J. Herzfeld, R. J. Temkin, and R. G. Griffin, "Dynamic nuclear polarization at 700 MHz/460 GHz," *Journal of Magnetic Resonance*, vol. 224, pp. 1–7, 2012.

[81] D. A. Hall, D. C. Maus, G. J. Gerfen, S. J. Inati, L. R. Becerra, F. W. Dahlquist, and R. G. Griffin, "Polarization-enhanced NMR spectroscopy of biomolecules in frozen solution," *Science*, vol. 276, pp. 930–932, 1997.

[82] M. Rosay, V. Weis, K. E. Kreischer, R. J. Temkin, and R. G. Griffin, "Two-dimensional 13C-13C correlation spectroscopy with magic angle spinning and dynamic nuclear polarization," *Journal of the American Chemical Society*, vol. 124, pp. 3214–3215, 2002.

[83] M. Rosay, J. C. Lansing, K. C. Haddad, W. W. Bachovchin, J. Herzfeld, R. J. Temkin, and R. G. Griffin, "High-frequency dynamic nuclear polarization in MAS spectra of membrane and soluble proteins," *Journal of the American Chemical Society*, vol. 125, pp. 13626–13627, 2003.

[84] P. C. A. van der Wel, K.-N. Hu, J. Lewandowski, and R. G. Griffin, "Dynamic nuclear polarization of amyloidogenic peptide nanocrystals: GNNQQNY, a core segment of the yeast prion protein Sup35p," *Journal of the American Chemical Society*, vol. 128, pp. 10840–10846, 2006.

[85] C. Song, K.-N. Hu, C.-G. Joo, T. M. Swager, and R. G. Griffin, "Totapol: A biradical polarizing agent for dynamic nuclear polarization experiments in aqueous media," *Journal of the American Chemical Society*, vol. 128, pp. 11385–11390, 2006.

[86] K. J. Pike, T. F. Kemp, H. Takahashi, R. Day, A. Howes, E. V. Kryukov, J. F. MacDonald, A. E. C. Collis, D. R. Bolton, R. J. Wylde, M. Orwick, K. Kosuga, A. J. Clark, T. Idehara, A. Watts, G. M. Smith, M. E. Newton, R. Dupree, and M. E. Smith, "A spectrometer designed for 6.7 and 14.1 T DNP-enhanced solid-state MAS NMR using quasi-optical microwave transmission," *Journal of Magnetic Resonance*, vol. 215, pp. 1–9, Feb. 2012.

[87] A. J. Rossini, A. Zagdoun, F. Hegner, M. Schwarzwaelder, D. Gajan, C. Coperet, A. Lesage, and L. Emsley, "Dynamic nuclear polarization NMR spectroscopy of microcrystalline solids," *Journal of the American Chemical Society*, vol. 134, pp. 16899–16908, 2012.

[88] D. Lee, H. Takahashi, A. S. L. Thankamony, J.-P. Dacquin, M. Bardet, O. Lafon, and G. De Paepe, "Enhanced solid-state NMR correlation spectroscopy of quadrupolar nuclei using dynamic nuclear polarization," *Journal of the American Chemical Society*, vol. 134, pp. 18491–18494, 2012.

[89] J. H. Ardenkjaer-Larsen, B. Fridlund, A. Gram, G. Hansson, L. Hansson, M. H. Lerche, R. Servin, M. Thaning, and K. Golman, "Increase in signal-to-noise ratio of >10,000 times in liquid-state NMR," *Proceedings of the National Academy of Sciences of the United States of America*, vol. 100, pp. 10158–10163, Sept. 2003.

[90] M. Rosay, L. Tometich, S. Pawsey, R. Bader, R. Schauwecker, M. Blank, P. M. Borchard, S. R. Cauffman, K. L. Felch, R. T. Weber, R. J. Temkin, R. G. Griffin, and W. E. Maas, "Solid-state dynamic nuclear polarization at 263 GHz: spectrometer design and experimental results," *Physical Chemistry Chemical Physics*, vol. 12, pp. 5850–5860, 2003.

[91] V. S. Bajaj, M. K. Hornstein, K. E. Kreischer, J. R. Sirigiri, P. P. Woskov, M. L. Mak-Jurkauskas, J. Herzfeld, R. J. Temkin, and R. G. Griffin, "250 GHz CW gyrotron oscillator for dynamic nuclear polarization in biological solid state NMR," *Journal of Magnetic Resonance*, vol. 189, pp. 251–279, 2007.

[92] P. A. S. Cruickshank, D. R. Bolton, D. A. Robertson, R. I. Hunter, R. J. Wylde, and G. M. Smith, "A kilowatt pulsed 94 GHz electron paramagnetic resonance spectrometer with high concentration sensitivity, high instantaneous bandwidth, and low dead time," *Review of Scientific Instruments*, vol. 80, p. 103102, Oct. 2009.

[93] C. Poole, *Electron Spin Resonance: A Comprehensive Treatise on Experimental Techniques*. John Wiley & Sons, Inc., 1983.

[94] G. M. Smith, P. A. S. Cruickshank, D. R. Bolton, and D. A. Robertson, "High-field pulse EPR instrumentation," *Electron Paramagnetic Resonance*, vol. 21, pp. 216–233, 2008.

[95] M.-T. Tuerke, I. Tkach, M. Reese, P. Hoefer, and M. Bennati, "Optimization of dynamic nuclear polarization experiments in aqueous solution at 15 MHz/9.7 Ghz: a comparative study with DNP at 140 MHz/94 GHz," *Physical Chemistry Chemical Physics*, vol. 12, no. 22, pp. 5893–5901, 2010.

[96] J. A. Villanueva-Garibay, G. Annino, P. J. M. van Bentum, and A. P. M. Kentgens, "Pushing the limit of liquid-state dynamic nuclear polarization at high field," *Physical Chemistry Chemical Physics*, vol. 12, no. 22, pp. 5846–5849, 2010.

[97] M. J. Prandolini, V. P. Denysenkov, M. Gafurov, B. Endeward, and T. F. Prisner, "High-field dynamic nuclear polarization in aqueous solutions," *Journal of the American Chemical Society*, vol. 131, p. 6090, May 2009.

[98] J. G. Krummenacker, V. P. Denysenkov, and T. F. Prisner, "Liquid state DNP on metabolites at 260 GHz EPR/400 MHz NMR frequency," *Applied Magnetic Resonance*, vol. 43, pp. 139–146, July 2012.

[99] L. Frydman and D. Blazina, "Ultrafast two-dimensional nuclear magnetic resonance spectroscopy of hyperpolarized solutions," *Nature Physics*, vol. 3, pp. 415–419, 2007.

[100] K. Golman, J. H. Ardenkjaer-Larsen, J. S. Petersson, S. Mansson, and I. Leunbach, "Molecular imaging with endogenous substances," *Proceedings of the National Academy of Sciences*, vol. 100, pp. 10435–10439, 2003.

[101] K. Golman, R. in't Zandt, M. Lerche, R. Pehrson, and J. H. Ardenkjaer-Larsen, "Metabolic imaging by hyperpolarized ^{13}C magnetic resonance imaging for in vivo tumor diagnosis," *Cancer Research*, vol. 66, pp. 10855–10860, 2006.

[102] C. von Morze, S. Sukumar, G. D. Reed, P. E. Z. Larson, R. A. Bok, J. Kurhanewicz, and D. B. Vigneron, "Frequency-specific SSFP for hyperpolarized ^{13}C metabolic imaging at 14.1 T," *Magnetic Resonance Imaging*, vol. 31, pp. 163–170, 2013.

[103] J. Leggett, R. Hunter, J. Granwehr, R. Panek, A. J. Perez-Linde, A. J. Horsewill, J. McMaster, G. Smith, and W. Koeckenberger, "A dedicated spectrometer for dissolution DNP NMR spectroscopy," *Physical Chemistry Chemical Physics*, vol. 12, pp. 5883–5892, 2010.

[104] R. Panek, J. Granwehr, J. Leggett, and W. Koeckenberger, "Slice-selective single scan proton COSY with dynamic nuclear polarisation," *Physical Chemistry Chemical Physics*, vol. 12, pp. 5771–5778, 2010.

[105] E. M. Purcell and R. V. Pound, "A nuclear spin system at negative temperature," *Physical Review*, vol. 81, pp. 279–280, 1951.

[106] S. Grosse, F. Gubaydullin, H. Scheelken, H. M. Vieth, and A. V. Yurkovskaya, "Field cycling by fast NMR probe transfer: Design and application in field-dependent CIDNP experiments," *Applied Magnetic Resonance*, vol. 17, pp. 211–225, 1999.

[107] M. Reese, D. Lennartz, T. Marquardsen, P. Hoefer, A. Tavernier, P. Carl, T. Schippmann, M. Bennati, T. Carlomagno, F. Engelke, and C. Griesinger, "Construction of a liquid-state NMR DNP shuttle spectrometer: First experimental results and evaluation of optimal performance characteristics," *Applied Magnetic Resonance*, vol. 34, pp. 301–311, Aug. 2008.

[108] P. Lottmann, T. Marquardsen, A. Krahn, A. Tavernier, P. Hoefer, M. Bennati, F. Engelke, and C. Griesinger, "Evaluation of a shuttle DNP spectrometer by calculating the coupling and global enhancement factors of L-tryptophan," *Applied Magnetic Resonance*, vol. 43, pp. 207–221, July 2012.

[109] T. Maly, D. Cui, R. G. Griffin, and A. F. Miller, "^{1}H dynamic nuclear polarization based on an endogenous radical," *Journal of Physical Chemistry B*, vol. 116, pp. 7055–7065, 2012.

[110] D. Grucker, T. Guiberteau, B. Eclancher, J. Chambron, R. Chiarelli, A. Rassat, G. Subra, and B. Gallez, "Dynamic nuclear-polarization with nitroxides dissolved in biological-fluids," *Journal of Magnetic Resonance Series B*, vol. 106, pp. 101–109, Feb. 1995.

[111] B. D. Armstrong and S. Han, "A new model for Overhauser enhanced nuclear magnetic resonance using nitroxide radicals," *Journal of Chemical Physics*, vol. 127, p. 104508, Sept. 2007.

[112] R. A. Wind and J. H. Ardenkjaer-Larsen, "^{1}H DNP at 1.4 T of water doped with a triarylmethyl-based radical," *Journal of Magnetic Resonance*, vol. 141, pp. 347–354, Dec. 1999.

[113] P. Hoefer, G. Parigi, C. Luchinat, P. Carl, G. Guthausen, M. Reese, T. Carlomagno, C. Griesinger, and M. Bennati, "Field dependent dynamic nuclear polarization with radicals in aqueous solution," *Journal of the American Chemical Society*, vol. 130, p. 3254, Mar. 2008.

[114] M.-T. Tuerke, G. Parigi, C. Luchinat, and M. Bennati, "Overhauser DNP with 15N labelled Fremy's salt at 0.35 Tesla," *Physical Chemistry Chemical Physics*, vol. 14, no. 2, pp. 502–510, 2012.

[115] K.-N. Hu, C. Song, H.-H. Yu, T. M. Swager, and R. G. Griffin, "High-frequency dynamic nuclear polarization using biradicals: A multifrequency EPR lineshape analysis," *The Journal of Chemical Physics*, vol. 128, p. 052302, 2008.

[116] E. L. Dane, B. Corzilius, E. Rizzato, P. Stocker, T. Maly, A. A. Smith, R. G. Griffin, O. Ouari, P. Tordo, and T. M. Swager, "Rigid orthogonal bis-TEMPO biradicals with improved solubility for dynamic nuclear polarization," *The Journal of Organic Chemistry*, vol. 77, pp. 1789–1797, 2012.

[117] M. Gafurov, S. Lyubenova, V. Denysenkov, O. Ouari, H. Karoui, F. Le Moigne, P. Tordo, and T. Prisner, "EPR characterization of a rigid bis-TEMPO-bis-Ketal for dynamic nuclear polarization," *Applied Magnetic Resonance*, vol. 37, pp. 505–514, Jan. 2010.

[118] B. Borah and R. G. Bryant, "NMR relaxation dispersion in an aqueous nitroxide system," *Journal of Chemical Physics*, vol. 75, p. 3297, 1981.

[119] A. Peksoz, M. A. Cimenoglu, and A. Yalciner, "Dynamic nuclear polarization in some aliphatic and aromatic solutions as studied by fluorine-electron double resonance," *Journal of Dispersion Science and Technology*, vol. 29, pp. 40–45, 2008.

[120] J. H. Ardenkjaer-Larsen, I. Laursen, I. Leunbach, G. Ehnholm, L.-G. Wistrand, J. S. Petersson, and K. Golman, "EPR and DNP properties of certain novel single electron contrast agents intended for oximetric imaging," *Journal of Magnetic Resonance*, vol. 133, pp. 1–12, 1998.

[121] M. Bennati, C. Luchinat, G. Parigi, and M.-T. Tuerke, "Water 1H relaxation dispersion analysis on a nitroxide radical provides information on the maximal signal enhancement in Overhauser dynamic nuclear polarization experiments," *Physical Chemistry Chemical Physics*, vol. 12, no. 22, pp. 5902–5910, 2010.

[122] P. H. Fries, D. Imbert, and A. Melchior, "Determination of outer-sphere dipolar time correlation functions from high-field NMR measurements. Example of a Gd^{3+} complex in a viscous solvent," *Journal of Chemical Physics*, vol. 132, p. 044502, 2010.

[123] I. Nicholson, D. J. Lurie, and F. J. L. Robb, "The application of proton-electron double-resonance imaging techniques to proton mobility studies," *Journal of Magnetic Resonance Series B*, vol. 104, pp. 250–255, 1994.

[124] R. Bates and W. Drozdoski, "Use of nitroxide spin labels in studies of solvent-solute interactions," *The Journal of Chemical Physics*, vol. 67, pp. 4038–4044, 1977.

[125] D. Sezer, M. Gafurov, M. J. Prandolini, V. P. Denysenkov, and T. F. Prisner, "Dynamic nuclear polarization of water by a nitroxide radical: rigorous treatment of the electron spin saturation and comparison with experiments at 9.2 Tesla," *Physical Chemistry Chemical Physics*, vol. 11, no. 31, pp. 6638–6653, 2009.

[126] E. Fukushima and S. Roeder, *Experimental Pulse NMR: A Nuts and Bolts Approach*. Perseus Books Publishing, L.L.C., 1981.

[127] J. Gewartowski and H. Watson, *Principles of Electron Tubes*. D. van Nostrand Company, Inc., 1965.

[128] J. Eichmeier and M. Thumm, eds., *Vacuum Electronics: Components and Devices*. Springer-Verlag Berlin Heidelberg, 2008.

[129] C. . P. I. Canada, "High power MMW amplifier 95 Ghz 100 Watts CW model series VKB 2463 datasheet."

[130] E. V. Kryukov, K. J. Pike, T. K. Y. Tam, M. E. Newton, M. E. Smith, and R. Dupree, "Determination of the temperature dependence of the dynamic nuclear polarisation enhancement of water protons at 3.4 Tesla," *Physical Chemistry Chemical Physics*, vol. 13, no. 10, pp. 4372–4380, 2011.

[131] Q. N. Teng, *Structural Biology: practical NMR applications*. Springer, New York, London, 2005.

[132] W. Tyrrell, "Hybrid circuits for microwaves," *Proceedings of the IRE*, vol. 35, pp. 1294–1306, 1947.

[133] P. J. M. van Bentum, G. H. A. van der Heijden, J. A. Villanueva-Garibay, and A. P. M. Kentgens, "Quantitative analysis of high field liquid state dynamic nuclear polarization," *Physical Chemistry Chemical Physics*, vol. 13, no. 39, pp. 17831–17840, 2011.

[134] T. Maly, G. T. Debelouchina, V. S. Bajaj, K.-N. Hu, C.-G. Joo, M. L. Mak-Jurkauskas, J. R. Sirigiri, P. C. A. van der Wel, J. Herzfeld, R. J. Temkin, and R. G. Griffin, "Dynamic nuclear polarization at high magnetic fields," *Journal of Chemical Physics*, vol. 128, p. 052211, Feb. 2008.

[135] Y. Matsuki, H. Takahashi, K. Ueda, T. Idehara, I. Ogawa, M. Toda, H. Akutsu, and T. Fujiwara, "Dynamic nuclear polarization experiments at 14.1 T for solid-state NMR," *Physical Chemistry Chemical Physics*, vol. 12, no. 22, pp. 5799–5803, 2010.

[136] K. Krynicki, "Proton spin-lattice relaxation in pure water between 0°C and 100°C," *Physica*, vol. 32, pp. 167–178, 1966.

[137] A. Krahn, P. Lottmann, T. Marquardsen, A. Tavernier, M.-T. Tuerke, M. Reese, A. Leonov, M. Bennati, P. Hoefer, F. Engelke, and C. Griesinger, "Shuttle DNP spectrometer with a two-center magnet," *Physical Chemistry Chemical Physics*, vol. 12, no. 22, pp. 5830–5840, 2010.

[138] R. Kausik and S. Han, "Ultrasensitive detection of interfacial water diffusion on lipid vesicle surfaces at molecular length scales," *Journal of the American Chemical Society*, vol. 131, pp. 18254–18256, 2009.

[139] B. Armstrong, J. Choi, C. Lopez, D. Wesener, W. Hubbell, S. Cavagnero, and S. Han, "Site-specific hydration dynamics in the nonpolar core of a molten globule by dynamic nuclear polarization of water," *Journal of the American Chemical Society*, vol. 133, pp. 5987–5995, 2011.

[140] A. Doll, E. Bordignon, B. Joseph, R. Tschaggelar, and G. Jeschke, "Liquid state DNP for water accessibility measurements on spin-labeled membrane proteins at physiological temperatures.," *Journal of magnetic resonance (San Diego, Calif. : 1997)*, vol. 222, pp. 34–43, Sept. 2012.

[141] R. Kausik and S. Han, "Dynamics and state of lipid bilayer-internal water unraveled with solution state ^{1}H dynamic nuclear polarization," *Phys. Chem. Chem. Phys.*, vol. 13, pp. 7732–7746, 2011.

[142] T. Brown, ed., *Molecular Biology: Labfax*. Academic Press Inc., 1991.

[143] A. Ault and G. Dudek, *NMR: An Introduction to Proton Nuclear Magnetic Resonance Spectroscopy*. Holden-Day, Inc., 1976.

[144] *Bruker Almanac 2010*. Bruker Corporation, 2010.

[145] M. Dunn and T. Brophy, "Decomposition points of the amino acids," *The Journal of Biological Chemistry*, vol. 99, pp. 221–229, 1932.

[146] M. Lever, J. Blunt, and R. Maclagan, "Some ways of looking at compensatory kosmotropes and different water environments," *Comparative Biochemistry and Physiology Part A*, vol. 130, pp. 471–486, 2001.

[147] J. H. Freed, "Dynamic effects of pair correlation-functions on spin relaxation by translational diffusion in liquids .2. Finite jumps and independent T_1 processes," *Journal of Chemical Physics*, vol. 68, no. 9, pp. 4034–4037, 1978.

[148] K. H. Herrmann, A. Pohlmeier, D. Gembris, and H. Vereecken, "Three-dimensional imaging of pore water diffusion and motion in porous media by nuclear magnetic resonance imaging," *Journal of Hydrology*, vol. 267, pp. PII S0022–1694(02)00154–3, Oct. 2002.

[149] J. Huang, *Crystallization in polymorphic systems*. PhD thesis, University of Wisconsin-Madison, 2008.

[150] H.-D. Belitz, W. Grosch, and P. Schieberle, *Food Chemistry*. Springer-Verlag Berlin Heidelberg, 2009.

[151] Y. Wu, P. Ma, Y. Liu, and S. Li, "Diffusion coefficients of L-proline, L-threonine and L-arginine in aqueous solutions at 25°C," *Fluid Phase Equilibria*, vol. 186, pp. 27–38, 2001.

[152] P. Mieville, P. Ahuja, R. Sarkar, S. Jannin, P. R. Vasos, S. Gerber-Lemaire, M. Mishkovsky, A. Comment, R. Gruetter, O. Ouari, P. Tordo, and G. Bodenhausen, "Scavenging free radicals to preserve enhancement and extend relaxation times in NMR using dynamic nuclear polarization," *Angewandte Chemie-international Edition*, vol. 49, no. 35, pp. 6182–6185, 2010.

[153] A. Chapiro, "Controlled propagation in associated monomer aggregates," *Pure and Applied Chemistry*, vol. 30, pp. 77–86, 1972.

[154] "GSI Chemical Database." http://www.gsi-net.com/en/publications/gsi-chemical-database.html, viewed 10 January 2013.

[155] D. Sezer, M. Gafurov, M. J. Prandolini, V. Denysenkov, and T. Prisner, "Dynamic nuclear polarization of water by a nitroxide radical: rigorous treatment of the electron spin saturation and comparison with experiments at 9.2 Tesla," *Physical Chemistry Chemical Physics*, vol. 11, pp. 6638–6653, 2009.

[156] M. Goldman, "Formal theory of spin-lattice relaxation," *Journal of Magnetic Resonance*, vol. 149, pp. 160–187, 2001.

[157] M.-T. Tuerke and M. Bennati, "Comparison of Overhauser DNP at 0.34 and 3.4 T with Fremy's Salt," *Applied Magnetic Resonance*, vol. 43, pp. 129–138, July 2012.